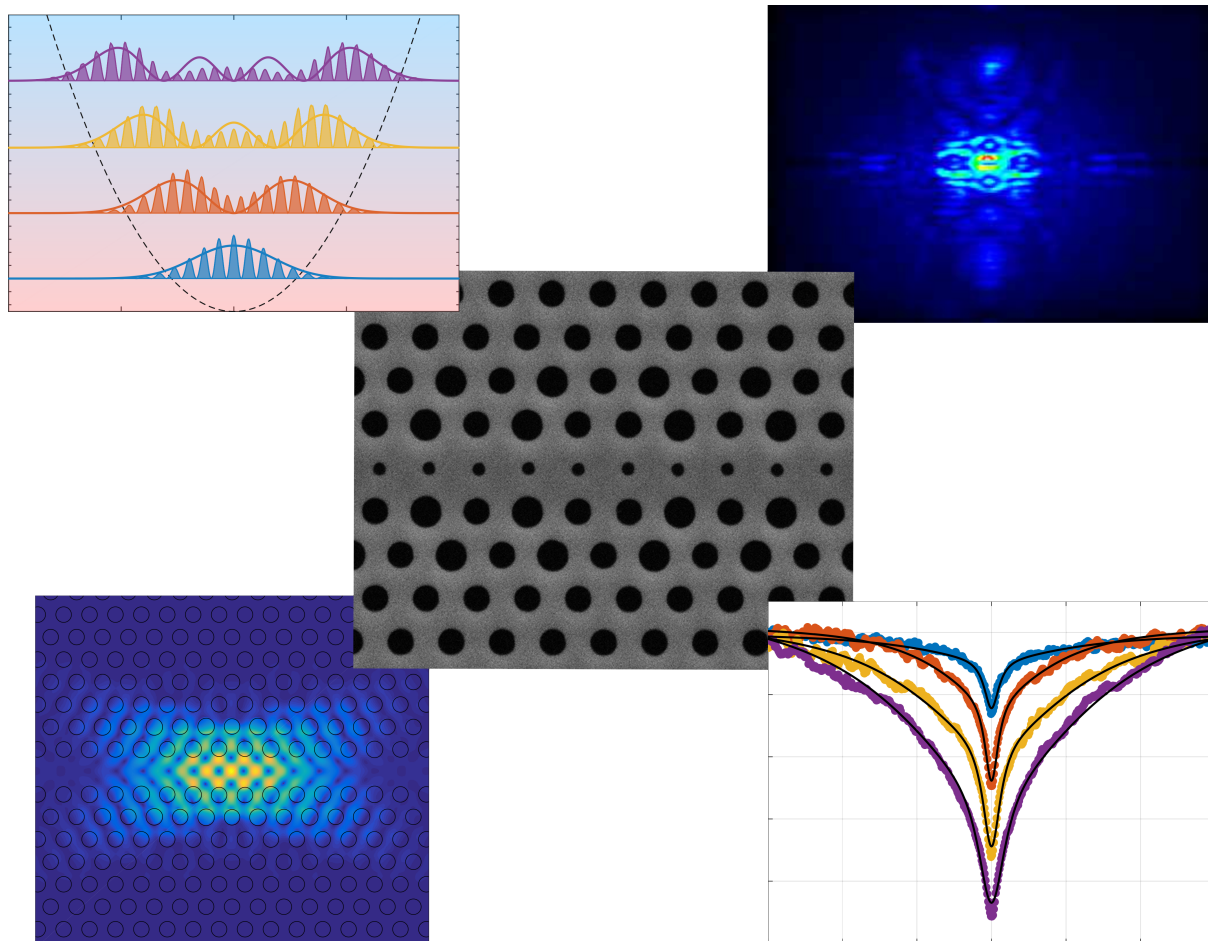


Nonlinear Optics in Photonic Crystal Cavities

Marco Clementi



Tesi per il conseguimento del titolo



Università degli Studi di Pavia
Dipartimento di Fisica

DOTTORATO DI RICERCA IN FISICA – XXXII CICLO

Nonlinear Optics in
Photonic Crystal Cavities

Marco Clementi

Submitted to the Graduate School of Physics in partial
fulfillment of the requirements for the degree of

DOTTORE DI RICERCA IN FISICA

DOCTOR OF PHILOSOPHY IN PHYSICS

at the

University of Pavia

Supervisor: Prof. Matteo Galli

Cover: (*top left*) Lowest-order localized modes in a bichromatic photonic crystal cavity and effective bichromatic potential. (*top right*) Near-field image of the generated second harmonic in a silicon-rich silicon nitride photonic crystal cavity and (*bottom left*) FDTD-calculated near-field profile for the same device. (*bottom right*) Measured probe transmission in a thermo-optically induced transparency experiment, blue pump detuning regime. (*center*) SEM image of one of the fabricated bichromatic cavity devices.

Nonlinear Optics in Photonic Crystal Cavities

Marco Clementi

PhD thesis - University of Pavia

Pavia, Italy, November 2019

*“There are more things in heaven and earth, Horatio,
Than are dreamt of in your philosophy.”*
- Hamlet (1.5 167-8)

Introduction

Harnessing light and its physical properties for applications to the technological domain is perhaps the ultimate objective of *photonics*, the branch of science which studies the generation, manipulation and detection of light in various types of devices. As for the field of electronics from which it stems, the interest towards the integration of optical devices to chip-scaled systems grew significantly in the last decades, with applications not only limited to optical communications and information processing, but also extending to numerous side-branches, such as sensing, biophysics and fundamental research. The key ingredients for integration emerge naturally as a by-product of semiconductor industry, where information technology is still the leading sector of interest. It is thanks to the technological maturity of semiconductor industry that devices proper of the optical domain, such as lasers, cavities, photodetectors, waveguides and many more have gradually found their counterpart in the realm of integrated circuits, improving and complementing a well-established technological compartment and casting a new light on the possible role of optics in the realization of the devices of the future.

A crucial feature of employing light as an information carrier is the extremely wide bandwidth made available by the modulation of optical signals, which makes photons the most popular support for communications over long distances via optical fibers. Though also information processing devices (e.g. *transistors*) would largely benefit from this and other features, the scarce capability to implement efficient photon-photon interactions has historically

set a main challenge in the direction of using light for this purpose. Nonetheless, fast and accurate all-optical signal processing is still made available by nonlinear optical interactions. A nonlinear medium, such as the semiconductor constituting the photonic device, can be indeed exploited to mediate the interaction between different optical signals, providing a way for instance to coherently convert their frequency, to switch them to different communication channels, or to provide a significant delay, realizing a memory. Even further, the interaction between light and matter can be exploited to tailor the quantum properties of light, providing a pathway to the implementation of *optical quantum technologies*, which study has been gathering more and more attention in the physics and engineering environment.

Tailoring the interaction of light and matter in integrated photonic devices, with specific focus on nonlinear optical processes, is the aim of the work presented in this thesis. We focus in particular on the use of a specific type of optical cavity, which can be realized with standard semiconductor technology fabrication processes, known as *photonic crystal cavity*. This kind of device enables an extremely effective confinement of the electromagnetic field both in time and space, making appreciable and suitable for the technological applications an otherwise elusive mechanism light-matter interaction.

Photonic crystal cavities

Photonic Crystals (PhCs) are physical systems where a periodic modulation of the refractive index is exploited to tailor the properties of light propagation in a dielectric medium [1]. A straightforward comparison can be drawn with the case of a crystalline medium, where the periodic arrangement of atoms constituting a solid provide yield energy bands and gaps. Similarly, in a PhC the photon's dispersion relation can be arranged in photonic bands, and the emergence of a photonic bandgap (PBG) may be observed under proper circumstances. The concept of PhC was first introduced by E. Yablonovich [2] and S. John [3] in 1987 and its description can be adapted to the one, two or three dimensional case (fig. 1), although early treatments of light propagation in periodic dielectric media date back to Lord Rayleigh [4]. While several examples of PhCs can be even observed in nature, the technological interest

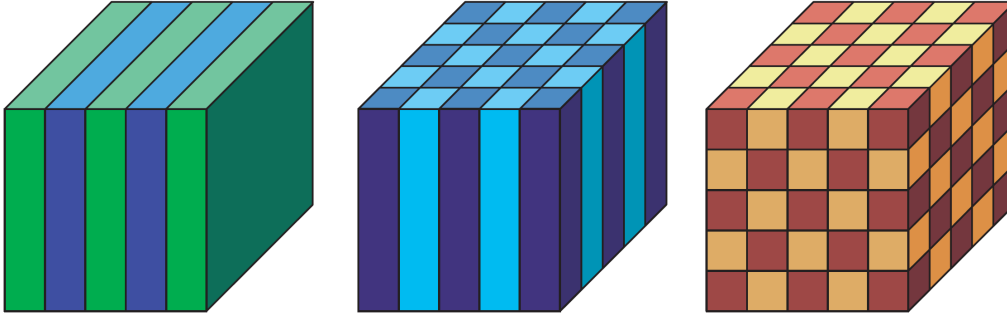


Figure 1: Schematic visualization of a one-, two- and three-dimensional photonic crystal. The periodic modulation of the refractive index is denoted by different colors [1].

of these structures can be understood in terms of control of light dispersion inside the nanostructured medium. An appropriate choice of the structural properties of a PhC device allows to engineer the arrangement of photonics bands and PBG, enabling to implement devices where the frequency or spatial dispersion of light is severely modified compared with the bulk medium. The flat dispersion relation provided by the structured medium can for instance exploited to realize slow-light waveguides, where the group velocity of electromagnetic radiation is reduced by more than one order of magnitude, while a negative value of the group index can be induced to yield superprism or superlensing effects [5].

The emergence of a PBG, on the other hand, translates effectively in a region of the spectrum where light cannot propagate inside the medium. This feature is well known since years and it is the basis for the realization of dielectric mirrors, where multiple thin layers of dielectric media are stacked in order to produce high quality reflectors, with better reflectivity than their metallic counterparts. The PBG is also at the origin of light confinement: heuristically, we can think about a medium where light propagation is inhibited in the three spatial dimensions and for both polarizations, namely exhibiting a *complete* PBG. Then, as in the case of a defect state in a crystalline solid, a single point defect inside the otherwise ideal photonic crystal may lead to the localization of an electromagnetic mode in correspondence of the perturbation. This circumstance provides a prototypical idea for a PhC

cavity, namely a device which exploits a PBG to confine the electromagnetic field in three dimensions. On a technological perspective, a complete PBG is not conventionally used, owing to the difficulties in the fabrication of three-dimensional PhC structures. Conversely, PhC cavities can be implemented in planar waveguides (*PhC slabs*) [6, 7], where confinement in the plane is provided by total internal reflection (TIR), or in periodically patterned linear waveguides (also known as *nanobeams*) [8], where TIR provides confinement in two dimensions and the PBG exists only for wavevectors belonging to guided modes.

Compared to other types of optical cavities, PhC microresonators have the peculiar feature of restricting the confinement to small mode volumes, namely to localize effectively the electromagnetic mode in space, while the decay time of the mode can be kept long compared to the optical cycle. For these reasons, these devices are particularly suited for maximizing the light-matter interaction, especially in the presence of nanostructures such as quantum dots or other kinds of single photon emitter [9]. Owing to the capability of tight light confinement, PhC cavities provide also a suitable platform to enhance nonlinearities of the material constituting the cavity or its surroundings, enabling to implement nonlinear optical devices such as switches, frequency converters etc. operating with low energy and fast response times.

The benefits and the potential of PhC cavities are tightly bound to their fabrication technology. In this sense, semiconductor industry provides the framework for the processing of the thin membranes required for the fabrications of PhC devices (such as the *silicon-on-insulator*, SOI), while *electron beam lithography* (EBL) and *reactive ion etching* (RIE) techniques allow a precise patterning of the bulk material. A precise and reproducible control over these nanofabrication techniques is crucial for the implementation and scalability of this kind of devices.

How to read this thesis

The present work encompasses the design, realization, characterization and processing of devices based on PhC cavities aimed to implement nonlinear

optical processes in chip-scaled structures. The focus is mainly targeted on planar (two-dimensional) structures and oriented both at aspects of fundamental research and technological applications.

The corpus of the thesis is divided in two macrosections: the first one discusses the background theory and the experimental methods, the second presents original theoretical and experimental results. The chapters are subdivided as follows: in chapter 1 we introduce the essential theory about PhC cavities and light-matter interaction, in chapter 2 we present the fabrication technique and the experimental methods used in this work. In chapter 3, we present our results about PhC cavities designed for optical frequency combs. In chapter 4, we discuss the investigations of a novel material, silicon-rich silicon nitride, for the fabrication and nonlinear operation of PhC resonators. In chapter 5 we present the study of a novel phenomenon originated by the dynamic thermo-optical effect observed in this kind of structures.

The experimental research was mainly carried out at the “Laboratorio di spettroscopia ottica” of the University of Pavia, in collaboration with several international research groups. Prof. Thomas Fromherz’s group at the Johannes Kepler Universität, Linz, Austria, provided the fabrication facilities used for the realization of the silicon devices exhibiting equally spaced modes. The collaboration was carried out in the framework of the European project “QuantERA CUSPIDOR”. The Silicon Photonics group, led by Dr Frederic Gardes at the Optoelectronic Research Center in Southampton, United Kingdom, was partner in a collaboration on the study of silicon-rich silicon nitride devices. The Nanophotonics group led by Prof. Liam O’ Faloain at the Cork Institute of Technology, Ireland, fabricated the samples used for the demonstration of thermo-optically induced transparency.

Contents

Introduction	iii
I Background	1
1 Theory	3
1.1 Photonic crystals	3
1.1.1 Defect states in a photonic crystal slab	13
1.2 Light-matter interaction	23
1.2.1 Control of spontaneous emission	23
1.2.2 Nonlinear processes	25
1.2.3 Optical bistability	38
2 Experimental methods	43
2.1 Fabrication	43
2.1.1 SOI wafer	43
2.1.2 PhC fabrication process	44
2.2 Resonant scattering	53
2.2.1 Experimental apparatus	54
II Results	61
3 PhC cavities for optical frequency combs	63

3.1	Motivation	63
3.2	Confinement mechanism	66
3.3	Cavity design	72
3.4	Experimental results	75
3.5	Post fabrication tuning	82
3.6	Four wave mixing	84
3.7	Conclusions	88
4	Nonlinear optics in silicon-rich silicon nitride PhC cavities	89
4.1	Motivation	89
4.2	The SRSN material platform	91
4.3	High-Q photonic crystal cavities	93
4.4	Cavity-enhanced harmonic generation	102
4.5	Conclusions	110
5	Thermo-optically induced transparency	113
5.1	Motivation	113
5.2	Overview	115
5.3	Theory	120
5.4	Experiments	127
5.4.1	Resonator characterization	128
5.4.2	High resolution pump and probe spectroscopy	131
5.4.3	Dynamical response	142
5.5	Conclusions	147
	Conclusions	149
	List of abbreviations	153
	List of publications	157
	Bibliography	158

List of Figures

1	Photonic crystals in one, two and three dimensions	v
1.1	Emergence of the photonic bandgap in one dimension	8
1.2	Dielectric and air band energy distribution in a multilayer . . .	9
1.3	Photonic band structure for the woodpile PhC.	10
1.4	Guided modes of a homogeneous dielectric slab	11
1.5	Examples of photonic crystal slabs	12
1.6	Photonic band structure for PhC slab of rods and holes.	13
1.7	Photonic band gap size as a function of the slab thickness . . .	14
1.8	Surface-, line- and point-defect in a PhC slab	15
1.9	W1-type photonic crystal waveguide	15
1.10	Band structure and field distribution of guided modes in a W1 PhC waveguide	16
1.11	Hexapole PhC cavity	18
1.12	Gentle confinement in a L3 PhC cavity	21
1.13	Energy level diagram for third-order nonlinear processes	25
1.14	Contributions to loss and dispersion in a PhC cavity from selected nonlinear effects	37
1.15	Dependence of free carrier lifetime on the free carrier density . .	38
1.16	Bistable response of a PhC cavity	39
1.17	Bistable response and resonance shift for a dispersion compen- sated cavity	41

2.1	Schematic of the SmartCut process	45
2.2	PhC fabrication process	46
2.3	Electron beam lithography system	49
2.4	Exposed PMMA resist with test pattern of holes	51
2.5	Schematic and working principle of an ICP-RIE machine	52
2.6	SEM cross-section of a cleaved test pattern of holes	53
2.7	SEM images of fully processed bichromatic PhC cavities in silicon	54
2.8	Schematic of the resonant scattering apparatus	55
2.9	Experimental RS spectra	57
2.10	Far-field optimization of a L3 cavity	59
3.1	Optical parametric oscillator based on a SiN microring resonator	65
3.2	Schematic of the “bichromatic” cavity and of the effective confinement potential	67
3.3	Numerical and experimental results for the bichromatic cavity as a function of the lattice mismatch β	70
3.4	Harmonic mode profile and near-field distribution for a bichromatic PhC cavity	71
3.5	SEM image and design parameters for a bichromatic cavity with comb-like spectrum	73
3.6	Bichromatic cavity modes dispersion and FSR mismatch as a function of the defect row hole radius r'	74
3.7	High resolution resonant scattering setup	76
3.8	Experimental traces from high resolution RS	77
3.9	RS spectrum for a bichromatic cavity with Q exceeding one million	79
3.10	Comb-like RS spectrum of a bichromatic PhC cavity	80
3.12	Laser-assisted local oxidation of a PhC cavity	83
3.13	Selective tuning of a comb-like spectrum by laser assisted local oxidation	84
4.2	Refractive index and propagation losses of PECVD silicon nitride as a function on N/Si	92

LIST OF FIGURES

4.3	Effect of TPA in SRSN waveguides	94
4.4	GME calculation of the PhC waveguide bands in the SRSN platform	95
4.5	Design and realization of a SRSN high- Q PhC cavity	96
4.6	Typical RS spectra of high- Q SRSN PhC cavities	99
4.7	Numerical and experimental results for high- Q SRSN cavities .	99
4.8	Thermo-optic coefficient of silicon-rich silicon nitride	100
4.9	Power-dependent RS spectra of SRSN PhC cavities	101
4.10	Layout and SEM image of the SRSN sample used for HG experiments	103
4.11	Simulated near- and far- field pattern for the SRSN far-field optimized A1 cavity	104
4.12	Schematic of the experimental apparatus and experimental RS results from linear devices characterization	105
4.13	Images of the generated second- and third- harmonic in SRSN PhC cavities	107
4.14	Experimental results from nonlinear characterization of the SRSN devices	109
5.1	Dispersion and group index profile associated to an isolated absorption and gain resonance	114
5.2	Conceptual scheme of a thermo-optically coupled resonator . .	118
5.3	TOIT phenomenology for blue and red pump detuning	124
5.4	Coupling channels for an optical resonator	125
5.5	Predicted transmission and group delay spectra for different values of cavity energy	127
5.6	Contour plot of TOIT response	128
5.7	Dispersion adapted PhC cavity	129
5.8	RS spectrum for the DA cavity used in TOIT experiments . .	130
5.9	Bistable response and associated power-dependent shift	131
5.10	High-resolution pump and probe setup for the measurement of TOIT	133
5.11	Broadband TOIT response	136

5.12	Experimental TOIT at fixed input power	137
5.13	Power-dependent scaling of experimental TOIT, blue-detuning regime	138
5.14	Power-dependent scaling of experimental TOIT, red-detuning regime	139
5.15	Experimental TOIT at fixed pump wavelength	140
5.16	Spectral dependence of peak group delay	140
5.17	TOIT dip visibility as a function of coupled power	141
5.18	TOIT linewidth as a function of coupled power	141
5.19	Experimental setup used to probe the time-domain response of TO effect	143
5.20	Time-domain thermo-optical response	144
5.21	Time-domain thermo-optical response: power dependence and comparison with theory	145

Part I

Background

Chapter 1

Theory

We review here the essential theory supporting the concepts presented throughout this work. In section 1.1 we first formalize the problem of light propagation in a periodic medium and in a dielectric slab. We then show how this geometry can lead to the localization of electromagnetic modes. In section 1.2 we review the theory of light-matter interaction, with particular focus on nonlinear optical processes, and we discuss how they are affected by the presence of a cavity.

1.1 Photonic crystals

We focus our attention on a dielectric medium where the refractive index is periodically modulated in one, two or three dimensions (fig. 1). In the absence of free currents and charges, the macroscopic Maxwell's equations, which describe the electromagnetic field dynamics in an inhomogeneous medium, expressed in SI units, read [10]:

$$\nabla \cdot \mathbf{D} = 0 \quad (1.1a)$$

$$\nabla \cdot \mathbf{B} = 0 \quad (1.1b)$$

$$\nabla \times \mathbf{E} = -\frac{\partial \mathbf{B}}{\partial t} \quad (1.1c)$$

$$\nabla \times \mathbf{H} = \frac{\partial \mathbf{D}}{\partial t} \quad (1.1d)$$

where \mathbf{E} and \mathbf{H} are the macroscopic electric and magnetic field vectors, and \mathbf{D} and \mathbf{B} are respectively the displacement and magnetic induction fields. In a linear, isotropic, non-magnetic medium, the field vectors are both functions of space and time coordinates and they are related among each others by the constitutive relations $\mathbf{B}(\mathbf{r}) = \mu_0 \mathbf{H}(\mathbf{r})$ and $\mathbf{D}(\mathbf{r}) = \varepsilon_0 \varepsilon(\mathbf{r}) \mathbf{E}(\mathbf{r})$. Neglecting any explicit time dependence of the dielectric function $\varepsilon(\mathbf{r})$, and relying on the linearity of Maxwell's equations (1.1), we can expand the fields in terms of harmonic modes, which depend sinusoidally with time. This way, the electric and magnetic field oscillating at frequency ω are represented by the complex vectors:

$$\mathbf{E}(\mathbf{r}, t) = \mathbf{E}(\mathbf{r}) e^{-i\omega t}$$

$$\mathbf{H}(\mathbf{r}, t) = \mathbf{H}(\mathbf{r}) e^{-i\omega t}$$

With this formalism, Maxwell's equations can be expressed in a closed form for \mathbf{E} and \mathbf{H} [1]. The two divergence equations (1.1a) and (1.1b) can be rearranged:

$$\nabla \cdot \mathbf{H}(\mathbf{r}) = 0 \quad \nabla \cdot [\varepsilon(\mathbf{r}) \mathbf{E}(\mathbf{r})] = 0 \quad (1.2)$$

These two equations express the transversality condition of the electric and magnetic field for plane waves propagating inside the medium. The two curl equations (1.1c) and (1.1d) can be also recast in a closed form, where the dependence on the electric (or magnetic) field is dropped. This operation provides the relevant *master equation* for the description of light propagation inside the medium:

$$\boxed{\nabla \times \left(\frac{1}{\varepsilon(\mathbf{r})} \nabla \times \mathbf{H}(\mathbf{r}) \right) = \left(\frac{\omega}{c} \right)^2 \mathbf{H}(\mathbf{r})} \quad (1.3)$$

where $c = \frac{1}{\sqrt{\varepsilon_0 \mu_0}}$ is the speed of light in vacuum.

The master equation (1.3) can be interpreted as an eigenvalues equation, where the Hermitian¹ differential operator $\hat{\Theta} = \nabla \times \frac{1}{\varepsilon(\mathbf{r})} \nabla \times$ acts on the eigenfunction \mathbf{H} and with associated real eigenvalue $(\omega/c)^2$. Similarly to the case of time-independent Schrödinger equation, which yields the spatial profile of matter waves in non-relativistic quantum mechanics, eq. (1.3) models the spatial dependence of electromagnetic waves propagating in an inhomogeneous dielectric medium. The eigenvectors of the problem represent the spatial profiles of the propagating modes, with associated frequencies ω , and they form a complete orthonormal set. The role of the Hamiltonian operator is here replaced by the operator $\hat{\Theta}$, while the dielectric function takes the role of a time-independent potential.

Provided that the dielectric function $\varepsilon(\mathbf{r})$ is known, the procedure to solve the problem of light propagation is then the following: the solution of eq. (1.3), which can be calculated either analytically or numerically, provides the magnetic field modes and the respective oscillating frequencies ω . Then, the electric field vector can be recovered from eq. (1.1d):

$$\mathbf{E}(\mathbf{r}) = \frac{i}{\omega \varepsilon_0 \varepsilon(\mathbf{r})} \nabla \times \mathbf{H}(\mathbf{r}) \quad (1.4)$$

which automatically satisfies the transversality requirement $\nabla \cdot \varepsilon \mathbf{E} = 0$.

Light propagation in a periodic medium

The next step is to include the periodicity of the medium in our treatment. By drawing a direct parallelism with the case of the electron in a crystalline solid, we will introduce a description of the medium in terms of a primitive unit cell (*basis*) replicated periodically in one or more dimensions via a well-defined pattern (*lattice*). Mathematically, this translates in a periodicity of

¹This operator is Hermitian only if the dielectric function $\varepsilon(\mathbf{r})$ is real, namely if the medium is transparent at the frequency ω . We will make this assumption throughout this introductory chapter.

the dielectric function:

$$\varepsilon(\mathbf{r}) = \varepsilon(\mathbf{r} + \mathbf{R}) \quad (1.5)$$

where \mathbf{R} is a linear combination of primitive lattice vectors, i.e. $\mathbf{R} = n\mathbf{a}_1 + m\mathbf{a}_2 + l\mathbf{a}_3$, with $(n, m, l) \in \mathbb{N}^3$ in the three-dimensional case. We can thus identify a discrete translation operator $\hat{T}_{\mathbf{R}}$ which commutes with $\hat{\Theta}$ and, in analogy with Bloch's theorem from solid state theory, conclude that $\hat{T}_{\mathbf{R}}$ and $\hat{\Theta}$ share a common set of eigenvectors, while \mathbf{k} represent a “good quantum number” for the problem. More rigorously, this result, known as *Bloch-Floquet theorem*, can be stated as follows [1, 11]:

Theorem. *The solutions to eq. (1.3) for a periodic medium can be expressed in the form $\mathbf{H}_{\mathbf{k}}(\mathbf{r}) = e^{i\mathbf{k}\cdot\mathbf{r}}\mathbf{u}_{\mathbf{k}}(\mathbf{r})$, where $\mathbf{u}_{\mathbf{k}}(\mathbf{r}) = \mathbf{u}_{\mathbf{k}}(\mathbf{r} + \mathbf{R})$, called Floquet mode, is a function having the same periodicity of $\varepsilon(\mathbf{r})$.*

It is straightforward to show that the eigenvalue problem (1.3) can be recast in an appropriate form for the Floquet modes $\mathbf{u}_{\mathbf{k}}(\mathbf{r})$ so defined. Invoking again a parallelism with solid state physics, it is also possible to show that the eigenfrequencies $\omega_n(\mathbf{k})$ can be opportunely arranged in the Brillouin zone (BZ), constituting the so-called *photonic bands*.

It is worth emphasizing that not only the discrete translational invariance yields an appropriate classification of eigensolutions of eq. (1.3), but also any other (continuous or discrete) symmetry of the problem. In particular, the even or odd symmetry of the field profile under reflection with respect to a plane yields a classification of a mode according with its *parity*. This distinction is particularly useful in the characterization of guided modes in a PhC waveguide, or, as we will detail later, in the case of confined modes in a PhC cavity. Another relevant symmetry property to consider is *time-reversal invariance* (or *reciprocity*), which yields the equivalence of eigenstates under inversion of the wavevector $\omega_n(\mathbf{k}) = \omega_n(-\mathbf{k})$.

A further similarity with crystalline solids which stems from the periodicity of the dielectric consists in the presence of spectral regions which do not correspond to solutions of eq. (1.3). These spectral windows are called

1.1. Photonic crystals

photonic band gaps (PBGs) and within them the propagation of light is forbidden. A qualitative picture of the emergence of a PBG is visualized in figure 1.1. The photonic band structure for light propagation in a one-dimensional PhC (*multilayer*) with lattice constant a is plotted as a function of the wavevector, which is assumed to be perpendicular to the multilayer. In the first panel, a fictitious lattice constituted by the bulk material only (GaAs in this case, $\varepsilon = 13$, neglecting chromatic dispersion) is considered, and the band structure consists only in the *light line*:

$$\omega(k) = \frac{ck}{\sqrt{\varepsilon}} \quad (1.6)$$

folded within the first BZ. If the bulk medium is perturbed by the a modulation of the dielectric function, we can observe a clear separation between (now better outlined) first and second photonic bands, near the band edge of the BZ, namely the emergence of a PBG. The physical origin of the PBG can be identified in a coupling between the forward and backward propagating wave inside the material, which eigenfrequencies become degenerate at the band edge in the absence of a perturbation. Since the magnitude of the coupling is proportional to the dielectric function contrast between the two materials, higher values of this yield a wider PBG:

$$\frac{\Delta\omega}{\omega_m} \propto \frac{\Delta\varepsilon}{\varepsilon_m} \quad (1.7)$$

where the first term is the *gap-midgap ratio* and the second one is the *dielectric function contrast*, with $\varepsilon_m = \frac{\varepsilon_1 + \varepsilon_2}{2}$ and $\omega_m = \frac{\omega_1 + \omega_2}{2}$. This fact is shown in the central and right panels of fig. 1.1, where the gap width is dramatically increased if the GaAs is alternated with air (right) instead of a AlGaAs alloy ($\varepsilon = 12$, center).

The photonic bands $n = 1$ and $n = 2$ considered in this example play an analogous role to the valence band and conduction band of a solid. Fig. 1.2 shows the calculated energy distribution near the respective higher and lower band edges, and highlights an important property of the confinement mechanism: the electromagnetic energy is mostly concentrated in the high- ε dielec-

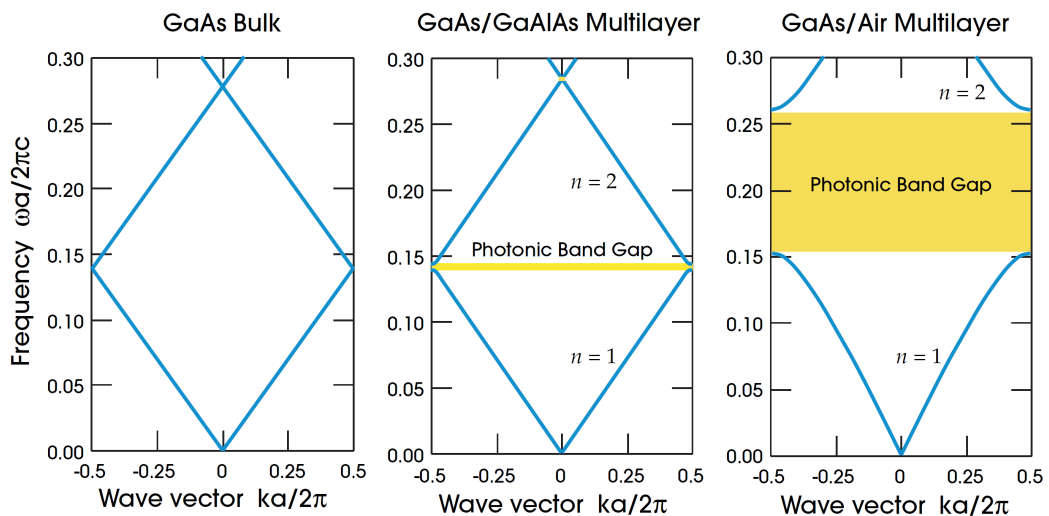


Figure 1.1: Emergence of the PBG in a one dimensional PhC (multilayer) structure. In the first panel, the bulk GaAs material is considered, and the dispersion relation is a straight line. If the fictitious periodicity a is introduced, this is folded in the BZ. In the central and right panels, the GaAs material is actually alternated with a lower index material, either GaAlAs alloy ($\varepsilon = 12$) and air ($\varepsilon = 1$), with the effect of introducing a splitting at the edge of the BZ. This corresponds to the PBG, which extent depends on the refractive index contrast. The emergence of the PBG makes physically meaningful a distinction between different photonic bands, here identified by the band index n [1].

tric for band 1, while it is mostly distributed within the low- ε dielectric in the case of band 2. This fact points to the role of the dielectric function $\varepsilon(\mathbf{r})$ as a confinement potential, and for this reason bands 1 and 2 are respectively denominated *dielectric band* and *air band*.

We restricted ourselves so far to the paradigmatic case of a one-dimensional PhC, namely a dielectric multilayer, and to orthogonal light propagation. The well-known properties of this structures were traditionally explained in the framework of Bragg reflection, where the overall reflectivity is computed as the coherent sum of reflection contributions at the multiple interfaces, and they are exploited in the fabrication of dielectric mirrors, which exhibit high-reflectivity, hardly achieved by metallic mirrors, in the PBG region [12]. Within our formalism, the non-orthogonal propagation of light can be included by considering the z -component of the wavevector and by performing a separation of variables in eq. (1.3). In this case, a non-degenerate behavior

1.1. Photonic crystals

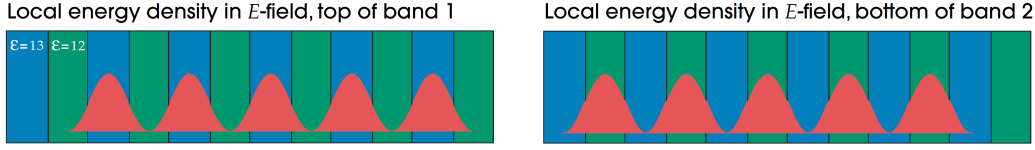


Figure 1.2: Electric field energy distribution $\frac{1}{2}\varepsilon|\mathbf{E}|^2$ for the dielectric (left) and air (right) band of a multilayer. Left and right panel correspond respectively to the top of band $n = 1$ and bottom of band $n = 2$ of fig. 1.1 [1].

for the s and p polarization should be taken into account.

In two or three dimensions, a PBG may exist in general only for specific subsets of \mathbf{k} vectors, corresponding to particular propagation directions and/or polarizations of the field. Ideally, the light propagation at a specific frequency ω is thus strictly forbidden only in the presence of a *complete PBG*. Although several examples of three-dimensional PhC exhibiting a complete PBG were demonstrated over the years (fig. 1.3), the fabrication of these structures is difficult in practice at optical wavelength. For this reason, practical implementations of PhC cavities usually rely on other mechanisms of confinement, such as total internal reflection (TIR) in semiconductor slabs or waveguides.

Photonic crystal slabs

PhC slabs constitute by far the most widespread platform for the realization of PhC cavities. This is due to the relatively easy fabrication process, which exploits techniques proper of the semiconductor industry. Let us consider the case of a homogeneous thin slab of semiconductor, or planar waveguide, with core refractive index $n_{core} = \sqrt{\varepsilon_{core}}$ and (upper and lower) cladding refractive index $n_{clad} = \sqrt{\varepsilon_{clad}}$. This structure can support guided modes provided that $n_{core} > n_{clad}$. In a ray optics picture, the presence of guided modes is possible thanks to TIR, provided that wavevector inclination is below the critical angle $\theta_c = \arcsin(n_{clad}/n_{core})$. More generally, the solution of Maxwell's equations can be carried out analytically [13], and yield lossless guided modes under the condition that the following inequality is satisfied:

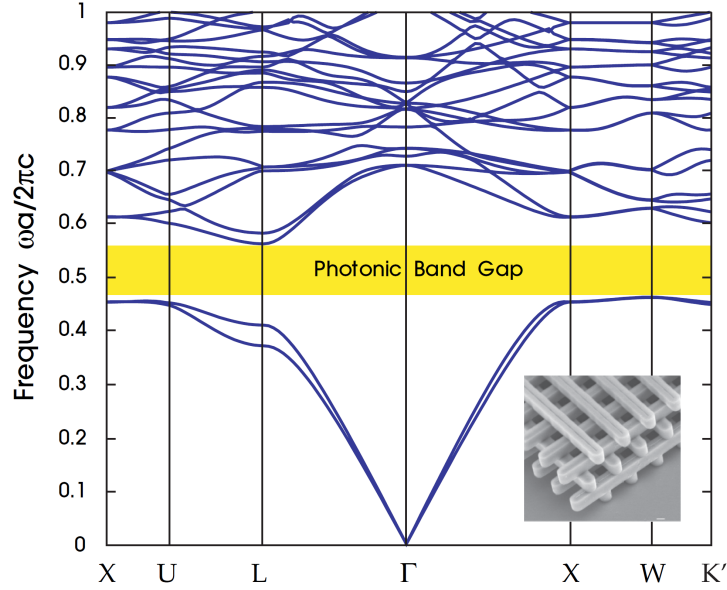


Figure 1.3: Photonic band structure for a three-dimensional PhC with woodpile structure (inset), with $\varepsilon = 13$ dielectric in air [1].

$$\omega < \frac{c}{n_{clad}} k_{\parallel} \quad (1.8)$$

where k_{\parallel} is the in-plane component of the wavevector, such that $k = \sqrt{k_{\perp}^2 + k_{\parallel}^2}$. The equality condition in eq. (1.8) identifies a locus of points, known as *light cone*, which describes the propagation in the homogeneous cladding medium at the critical angle. Consequently, all the points lying above the light cone correspond to solutions which are not bounded to the slab region, known as *leaky modes*.

Guided modes can be further classified according to symmetry with respect to the slab plane in transverse electric (TE), which have even symmetry and for which the electric field lies in the slab plane, and transverse magnetic (TM), which have odd symmetry and for which the magnetic field lies in the waveguide plane. The symmetry of the cladding yields the absence of a cutoff frequency for the fundamental TE and TM modes, namely the presence of at least two modes at any frequency. The modes of a dielectric slab are plotted in fig. 1.4. An effective index $n_{eff} = \omega c/k$ can be defined

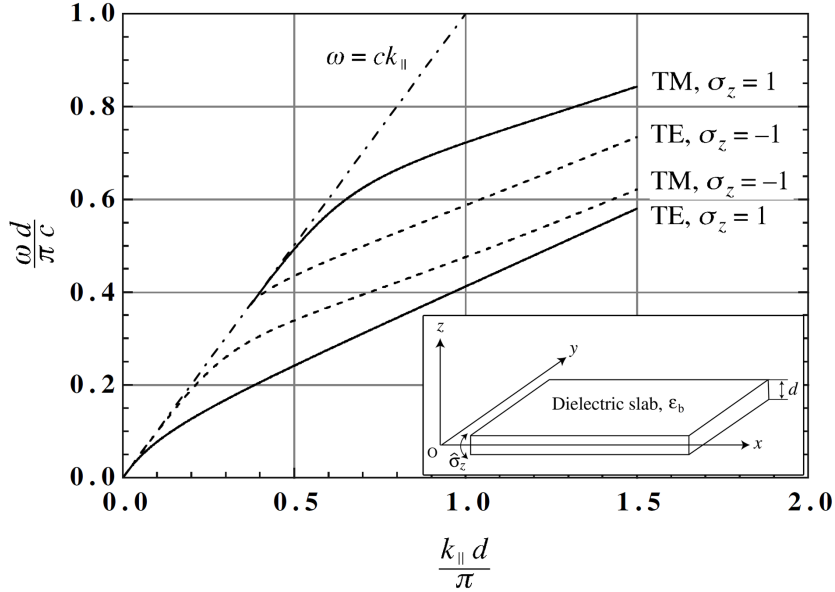


Figure 1.4: Lowest-order guided modes dispersion for a homogeneous dielectric slab (inset), with refractive index $n_{core} = 2.86$. TE and TM modes are separated according with symmetry under reflection with respect to the xy -plane [11].

for each guided mode, which value starts from n_{clad} at the cutoff frequency and tends asymptotically to n_{core} at high frequencies. This value provides a quantitative picture of the mode confinement effectiveness.

So far we considered a membrane of dielectric homogeneous in the xy -plane. If we now introduce a periodicity of the refractive index in two dimensions we obtain the PhC slab. Two examples are shown in fig. 1.5, namely a square lattice of dielectric rods in air and a triangular lattice of holes patterned in a dielectric membrane. For historical and technological reasons, the latter example is one of the most popular for the fabrication several PhC applications, such as waveguides and nanocavities. Although this type of structure is not a 2-dimensional PhC (the medium is not periodic nor homogeneous in the z -direction, where confinement is provided by TIR), a representation in the BZ (fig. 1.6) is still possible and we can use it to draw several analogies. First of all, we notice the present of the light-cone, which now affects all the photonic bands over a certain value of ω : we conclude that lossless propagation in the PhC slab is possible only for a finite number

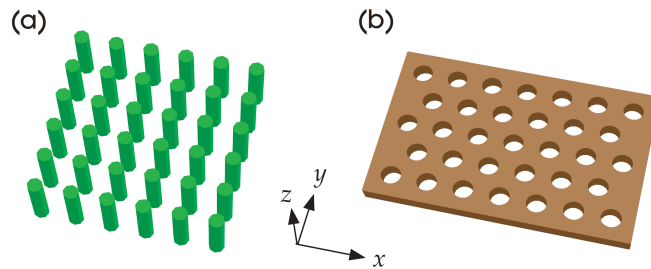


Figure 1.5: Examples of PhC slabs, which combine periodicity in two-dimensions (xy -plane) and TIR confinement in the vertical (z) direction. (a) Square lattice of dielectric rods in air. (b) Triangular lattice of holes in a PhC slab [1].

of guided modes. Second, we observe that the effect of the periodicity acts now as a perturbation which couples different photonic bands *and* different guided modes. Third, we remark that the symmetry of under xy reflection still sets a separation between two orthogonal sets of modes according with even/odd parity, which are denominated respectively *TE-like* and *TM-like*. We observe that a PBG may exist only for TE-like or TM-like modes, and only in the case of an ideal 2D PhC for both [14]. In particular, a lattice of rod favors the formation of a TM-like PBG, while a lattice of holes favors the TE-like PBG. It is worth noticing that the PBG of a PhC slab should always be considered incomplete, as it does not forbid the coupling to radiating modes.

The physical dimensions of the PhC slabs are typically chosen to be of the order of the wavelength inside the medium λ_0/n_{core} , and they can be tuned by design. The lattice constant a is perhaps the most relevant parameter. However, owing to scale invariance of Maxwell's equations, all the other parameters can be expressed as a function of this, while its actual value can be chosen in view of the resonant frequency foreseen by the design. For silicon-based membranes designed to operate at telecom wavelength ($\lambda_0 = 1550$ nm, $n_{Si} = 3.46$), the lattice step is typically of the order of 400 nm. Heuristically, the lattice step sets the size of the BZ, and thus the position of the lower band edge: consequently, lower values of a correspond to higher gap energies.

As shown in fig. 1.7, the thickness t of the slab plays a role in the determination of the gap width. For small values of t , the effective index is

1.1. Photonic crystals

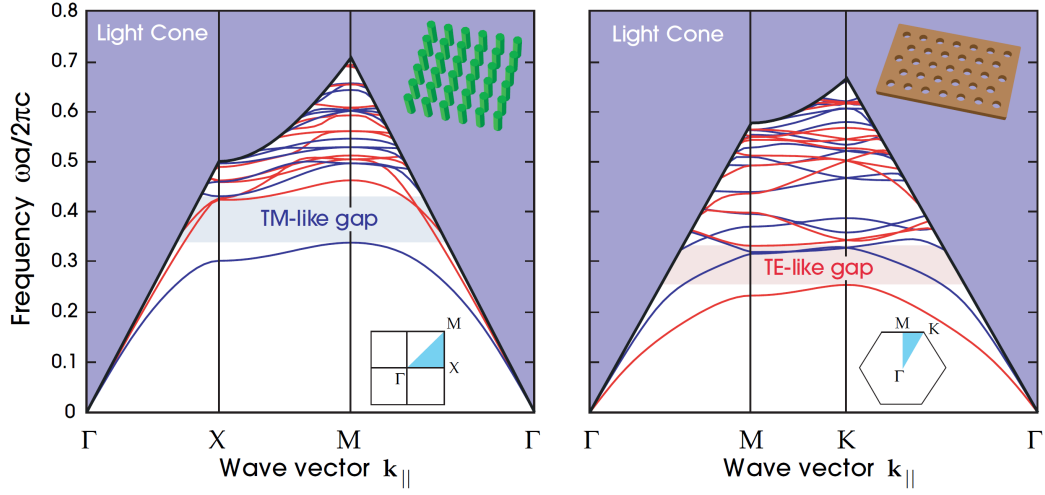


Figure 1.6: Photonic band structure for the PhC slabs represented in fig. 1.5. The shaded area represents the light cone, which is characterized by leaky modes propagating in air. Red and blue bands indicate TE- and TM-like modes respectively. The PBG area for these is represented by a light shaded area [1].

close to the one of the cladding, as the mode energy is mostly located in this region. As a consequence, the effect of a perturbation is relatively mild. By increasing the core thickness, the PBG width increases until the higher order modes enter the gap region. This sets a maximum value for the gap width, which is found around $t \approx 0.5a$ in typical PhC slabs based on triangular patterns of holes [15]. This geometry was shown to exhibit one of the highest values of gap-midgap ratio, which is of the order of $\sim 20 \div 30\%$.

Similar considerations can be drawn for the choice of hole radius r . Higher values yield wider PBGs, and a blueshift of the midgap energy, due to the lowering in the effective index. However, practical limitations related to fabrication (such as proximity effects in electron beam lithography) become relevant for large values of r and, for this reason, an optimal value around $r/a \approx 0.3$ is typically chosen.

1.1.1 Defect states in a photonic crystal slab

The formalism introduced so far describes effectively any guided mode of a PhC slab, which, concerning in-plane propagation, can be uniquely identified

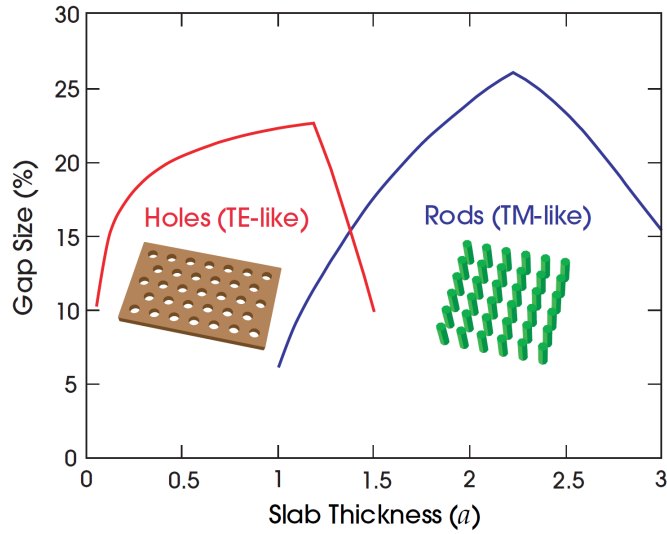


Figure 1.7: Photonic band gap size (gap-midgap ratio) for TE-like and TM-like modes as a function of the slab thickness, expressed in units of the lattice constant. For fixed hole/rod radius and increasing slab thickness, the gap size increases up to a maximum value, where the higher-order mode starts to enter the PBG region, causing a rapid decrease in the gap width [1].

by a band index and a wavevector. Owing to this classification, such modes are intrinsically delocalized within the slab, and they decay exponentially in the cladding region. By introducing a defect in the periodicity of the PhC slab (as well as of an ideal PhC), it is possible to induce the localization of the electromagnetic field in space. As summarized in fig. 1.8, this may consist in a one-dimensional alteration of the original lattice, resulting in a *line defect* (or a *surface mode* if the boundary region of the PhC is considered), which is characterized by a discrete translational invariance in only one direction, and may lead to the emergence of guided modes within the PBG spectral region. Another possibility is a “zero-dimensional” modification of the original lattice, namely a *point-defect*, which could only preserve reflection/inversion symmetries of the original lattices, and which may lead to localization in the real space.

PhC waveguide

A notable example of the former case is the *W1 waveguide*, which consists in

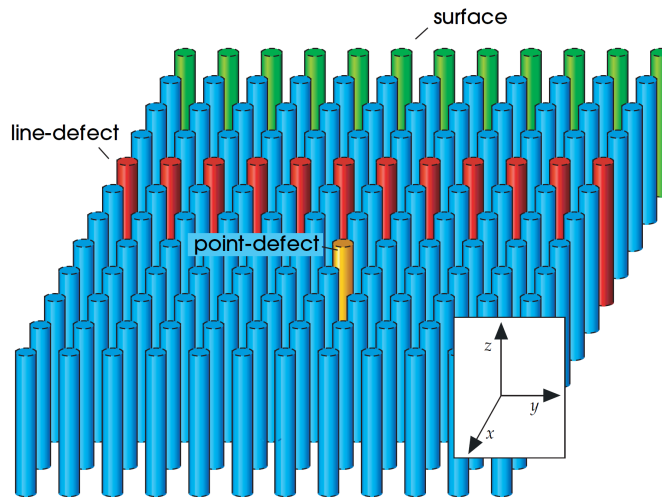


Figure 1.8: Schematics of different kinds of defect in a 2D PhC, specifically a surface-, a line- and a point-defect in a dielectric slab of rods. The latter type is particularly suited for the realization of PhC cavities [1].

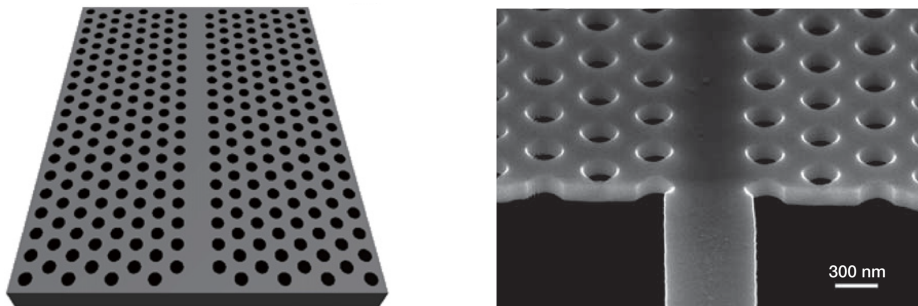


Figure 1.9: Schematic (left) and SEM image (right) of a W1 waveguide in a PhC slab. The structure is obtained as a line defect in a suspended membrane in air patterned with a triangular lattice of holes, where a row of holes is removed and replaced with the core dielectric [16, 17].

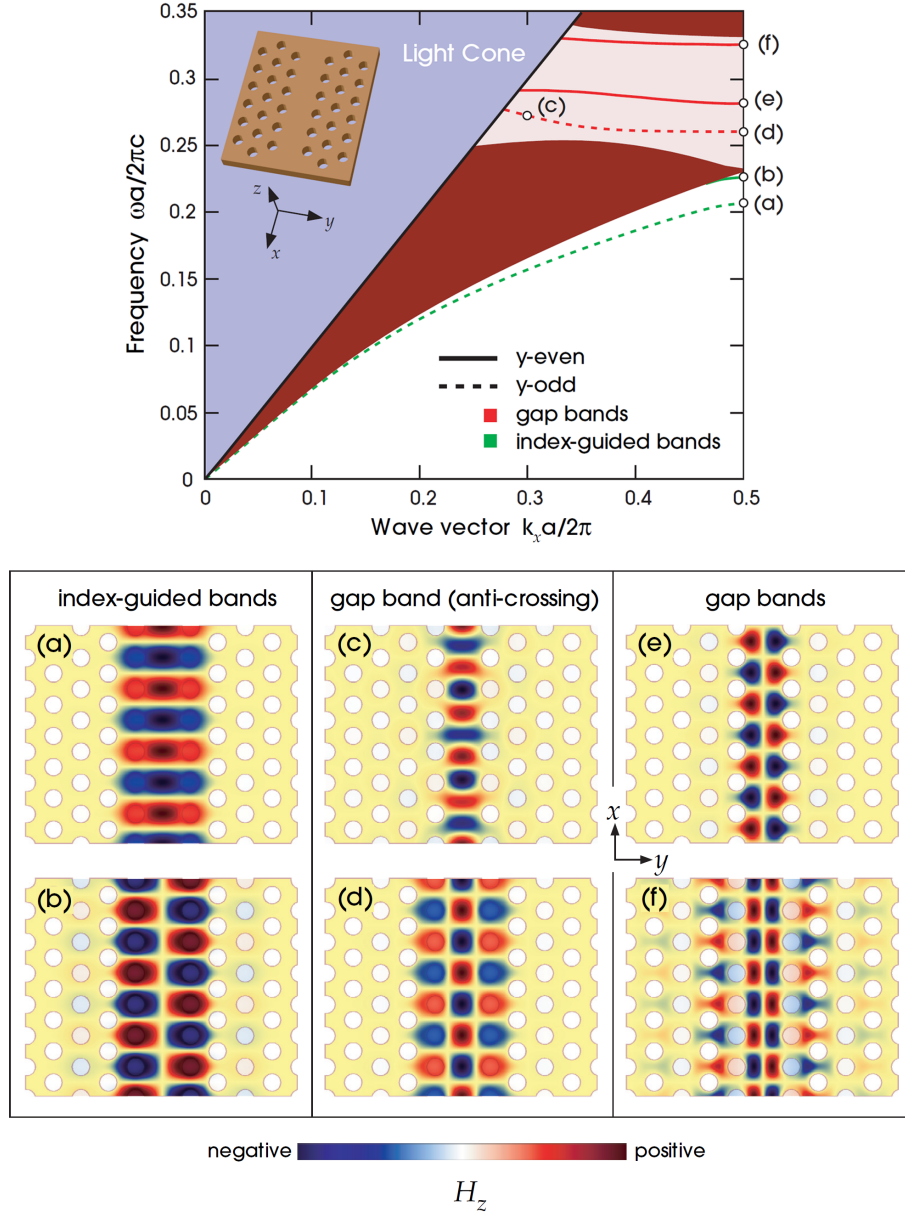


Figure 1.10: Band diagram (top) of TE-like modes for a W1 waveguide in a PhC slab, in the one-dimensional BZ. Red shaded areas represent the extended TE-like modes of the PhC slab. The guided modes are classified either according with their symmetry with respect to the xz -plane and with the confinement mechanism: index guided modes exist outside the PBG, while gap-guided bands are confined by Bragg-type reflection [1].

1.1. Photonic crystals

a PhC slab patterned with a triangular lattice of holes where a row of them is removed and replaced by the core dielectric (fig. 1.9). Heuristically, this modification increases the effective index experienced by the optical field, thus providing an effective confinement potential which favors the localization of light within the line defect, pushing down the original PhC bands. The resulting modes, plotted in the one-dimensional BZ as a function of the k_x wavevector, are represented in fig. 1.10. The lowest order TE-like and TM-like modes (a separation according with z -reflection symmetry is still possible) laying below the dielectric band edge are called *index-guided* modes, reminiscing the index-based confinement mechanism occurring close to the band edge, which does not necessarily require the presence of a PBG. Conversely, higher order modes rely on the existence of a periodic medium, and they are thus referred to as *gap-guided* modes.

A remarkable property of these states is their non-trivial dispersion relation, that can be exploited for applications to optical devices. A practical example is the use of PhC waveguides for the the achievement of structural slow light, which relies on the near-zero group velocity $v_g = \frac{\partial\omega}{\partial k}$ achievable by appropriately engineering the band dispersion. The real space field distribution of selected index-guided and gap-guided modes is represented in figure 1.10b.

It's worth to remark that despite only the bands laying outside the light cone are plotted, the propagation of leaky modes is still possible, keeping in mind that a fraction of the field energy will be lost by out-of-plane scattering during propagation. The loss rate can be estimated, for instance, via frequency domain methods by computing the coupling of leaky modes to radiating modes in first order time-dependent perturbation theory [18].

Finally, waveguide geometries alternative to the W1 are easily designed by tuning the parameters available, such as the width of the waveguide replacing the missing row of holes or by substituting the row with different patterns, such as holes of smaller radius, in order to achieve the desired dispersion for the guiding structure.

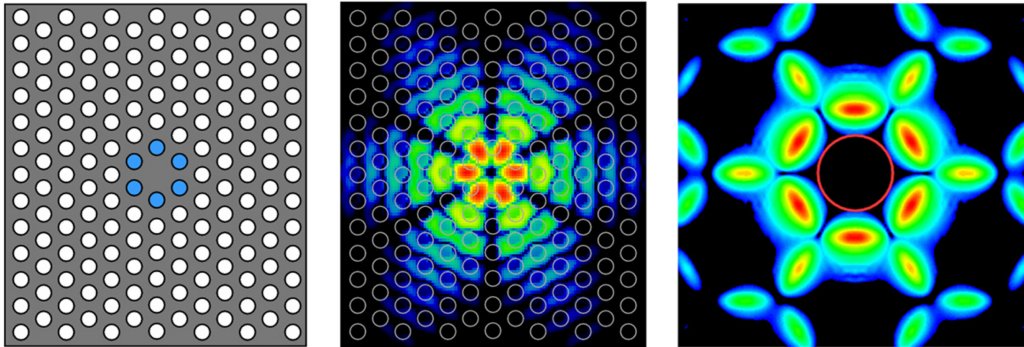


Figure 1.11: Example of PhC microresonator (hexapole, or “H1” PhC cavity). The localization of an electromagnetic mode is achieved by removing a single hole from an otherwise ideal triangular lattice, and by shifting the holes marked in blue outwards with respect to the center (left), for the purpose of gentle confinement (see main text). The resulting localized mode (center) field distribution in the real space inherits the symmetry of the system. The k -space profile (right) of the mode also exhibit sixfold discrete rotational symmetry. The red circle indicates the light-cone. The field intensity strength is logarithmically expressed by different shading. The absence of components within the light-cone region points to a limited amount of out-of-plane losses (i.e. high- Q) for the localized mode [19, 16].

Point defects

We now consider a point-like perturbation of one or few lattice sites, which breaks any translational symmetry of the system. This can be obtained for instance by removing one or more holes (fig. 1.11) from an otherwise periodic PhC crystal slab. This kind of defect can be used to induce localization of light in three-dimensions. Heuristically, we can think of an energy favorable lattice site to which it is possible to couple light, but, owing to the presence of a PBG, this cannot propagate within the slab, and it is thus confined. This physical system realizes a *photonic crystal cavity*, which can support one or multiple resonant modes.

Because of the lack of translational symmetry, any resonant mode will not have a well defined wavevector, and it will appear as a flat (dispersionless) state if represented in the BZ, corresponding to a well defined frequency ω_0 and located in the PBG spectral region. Conversely, in the real space the largest fraction of the optical energy of the mode will be restricted to a typically small volume, with a size of the order of the wavelength cubed

1.1. Photonic crystals

$V \sim (\lambda/n)^3$. Note how the former property is required to pursue localization in the real space, as the field distribution in the the direct and reciprocal space are linked by a Fourier transform: a well-defined position in the real space must correspond to a delocalized state in the \mathbf{k} -space. A fundamental consequence of this fact is that any mode localized via a point defect is leaky, namely it is characterized by intrinsic losses due to out-of-plane scattering. Of course, the argument is restricted to the case of PhC slabs, where the confinement mechanism is based on both TIR and PBG. The realization of PhC cavities exhibiting theoretically zero intrinsic losses would be possible in three-dimensional PhC systems characterized by a full 3D PBG. However, this case is not usually considered for practical applications due to the difficult fabrication and engineering process of 3D structures. In contrast, CMOS-based fabrication techniques make relatively easy to realize cavities based on PhC slabs, and the losses can be contained by adopting appropriate design strategies, as we shall discuss later.

As for any physical resonator, the losses of a PhC cavity mode can be quantified by a decay rate Γ . Under the assumption that the cavity loss can be described by the differential equation $\frac{dU}{dt} = -\Gamma U(t)$, where $U(t)$ is the total intracavity optical energy, the temporal dynamics of $U(t)$ is thus described by an exponential decay $U(t) = U_0 e^{-\Gamma t}$. In the spectral domain, this translates into a *Lorentzian lineshape* of the cavity response, centered at frequency ω_0 and characterized by a full-width half-maximum (FWHM) Γ :

$$L(\omega) = \frac{\left(\frac{1}{2}\Gamma\right)^2}{(\omega - \omega_0)^2 + \left(\frac{1}{2}\Gamma\right)^2} \quad (1.9)$$

A relevant figure of merit for the quantification of the losses is the quality factor:

$$Q = \frac{\omega_0}{\Gamma} \quad (1.10)$$

In practical applications, out-of-plane losses may not be the sole decay channel for the optical energy inside the cavity. In the presence of multiple, physically separated sources of (linear) losses, the decay rates can be summed up. Considering only the most important physical mechanisms which induce

losses in PhC cavities, the overall decay can be expressed as:

$$\Gamma = \Gamma_{int} + \Gamma_{abs} + \Gamma_{sc} + \Gamma_{ext} \quad (1.11)$$

which addends represent respectively the decay rates associated to out-of-plane scattering (intrinsic losses), the absorption rate by any absorber in the resonant mode volume, the scattering rate related to the disorder or imperfections introduced by fabrication and the extrinsic loss rate linked by any additional structure meant to couple to the cavity mode, such as, for instance, an evanescently coupled waveguide. For each of these contributions, an ad-hoc Q factor definition can be formulated on the lines of eq. (1.10), so that the overall Q factor can be expressed by the inverse sum $Q^{-1} = Q_{int}^{-1} + Q_{abs}^{-1} + Q_{sc}^{-1} + Q_{ext}^{-1}$. Notice how a classical lifetime or spectroscopic characterization could only provide the overall Q factor of the system.

Gentle confinement

A primary design target for applications of PhC cavities is the minimization of out-of-plane losses, or equivalently, the maximization of Q_{int} . The perhaps most popular strategy in view of this objective was proposed in the early era of PhC cavities research and it is known as *Noda's argument*. In 2003, S. Noda and collaborators [7] studied the fundamental mode profile in the reciprocal space of a L3 cavity, which is obtained by removing three holes from a PhC slab patterned with a triangular lattice of holes and its Q factor, under a slight symmetric modification of the position of the two inner-most remaining holes (fig. 1.12). It was shown that for a specific shift of the holes position, which corresponds to a smooth rather than abrupt transition of the mode profile envelope from the bulk dielectric to the patterned lattice, the fraction of the mode's energy in the reciprocal space falling within the light-cone region (represented as a circle in fig. 1.12) is minimized and hence the Q factor is maximized. The argument can be understood in view of the relation between the field distribution in the real and reciprocal space, the two of which are related by a Fourier transform. In particular, the highest value of Q is achieved if the profile of the mode in the real space approaches

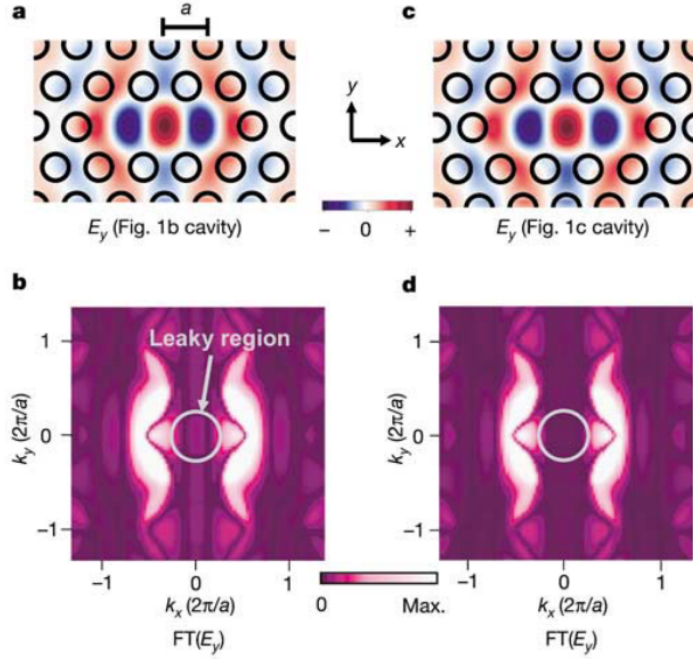


Figure 1.12: Gentle confinement in a L3 PhC cavity. The microresonator consists in the removal of three holes from a triangular lattice of holes (a) and, in the presence of gentle confinement (c), in the shift of the innermost residual holes along the x -direction. Panels (b) and (d) show how the far-field profile results modified in a way such that the amount of mode energy falling in the leaky (light cone) region is minimized, a situation corresponding to a Gaussian E_y field envelope in the real space. This setting represents the first experimental demonstration of a high- Q ($Q = 45,000$) PhC cavity, provided by Akahane *et al.* in 2003 [7].

a Gaussian distribution. This design approach, known as *gentle confinement*, can be recast to many cavity geometries (fig. 1.8) and it constitutes a powerful design tool for the engineering of PhC cavity based devices.

Mode volume

A second design target for actual PhC cavities is the *mode volume* of the localized state. Heuristically, this value quantifies the region of space effectively occupied by the mode energy, and thus the capability of a structure to confine light in the three dimensions (analogously, the Q factor quantifies the same figure of merit in time). Although several definitions of this quantity can be found in the literature, we will use here the one adopted in

the field of cavity quantum electrodynamics (cQED) [20], which is particularly meaningful under the treatment of Purcell effect, as we will discuss in section 1.2:

$$V = \frac{\int \varepsilon(\mathbf{r}) |\mathbf{E}(\mathbf{r})|^2 d^3\mathbf{r}}{\max \{\varepsilon(\mathbf{r}) |\mathbf{E}(\mathbf{r})|^2\}} \quad (1.12)$$

As aforementioned, this quantity is typically of the order of the wavelength of the resonant radiation inside the bulk dielectric medium $V \sim (\lambda/n)^3$. The literature provides several examples of structures where this quantity is strongly reduced, even to values much smaller than a wavelength cubed [21, 22, 23]. While it is still subject of debate whether a fundamental limit to the capability to confine light in three dimensions exists, it is worth noticing that the definition of V depends on the type of application which is aimed to implement, and thus its applicability as a figure of merit.

Many advantages stem from the minimization of the modal volume in the design of a PhC cavity. In Purcell's theory of spontaneous emission for a dipole emitter coupled to an optical cavity, it is shown how the emission rate is enhanced proportionally to the ratio Q/V [24]. On the other hand, the efficiency of several nonlinear processes of order n scale as $(Q/V)^n$ [25] and similarly, the power threshold of Kerr-type bistability scales as V/Q^2 [26]. Intuitively, the ratio Q/V for a resonant mode quantifies the "degree" of light-matter interaction for the region of space where this takes place. More rigorously, this quantity can be interpreted as a rescaling factor to the local density of optical states (DOS) [11, 27] as compared to the bulk case.

A small mode volume is not only object of interest because of the enhancement of light-matter interaction effect, but also, on a technological perspective, owing to the smaller device footprint available and on novel functionalities enabled by this feature, such as all-optical switching based on fast bistable effects [28].

The small modal volume is a specific feature of PhC cavities, and it relies on the presence of a PBG-type confinement mechanism. Other types of microresonators, such as microspheres, microtoroids and microrings, which rely only on TIR, require propagation of light which is always below the

critical angle θ_c , in order to minimize losses. Thus, the minimum size of the structure is typically strictly dependent on θ_c , while in the case of PhC resonators, even relying on hybrid PBG/TIR confinement like in the case of PhC slabs or nanobeams, confinement is automatically granted by the PBG, provided that the amount of components within the light cone is minimized. Thus, PhC cavities are among the best suited structures for the minimization of the mode volume in integrated optical devices.

1.2 Light-matter interaction

In this section we discuss the main effects of light-matter interaction which involve the confined mode of a PhC cavity and its surroundings. While the capability of this type of devices to confine light both in time and space has great interest in the framework of the control of spontaneous emission, a particular accent is given here on the effects of localization on the implementation of nonlinear optical processes, the application of which is particularly demanding in bulk optics in terms of optical powers. Conversely, a resonant integrated system can enhance the field at the point to require very small powers, which is a primary requirement for integrated photonics applications.

1.2.1 Control of spontaneous emission

Before introducing the formalism of nonlinear optics, we will briefly discuss the effects of a localized resonant mode on a dipole emitter, such as an atom, a quantum dot (QD) or a radiative crystalline defect coupled to the cavity field. A fundamental result in this direction was given in 1946 by E. Purcell [24], who showed that the spontaneous emission rate of atoms incorporated in a resonant electromagnetic cavity of quality factor Q and mode volume V is enhanced by a factor:

$$F_P = \frac{\Gamma_\mu}{\Gamma_0} = \frac{3}{4\pi^2} \left(\frac{\lambda}{n}\right)^3 \left(\frac{Q}{V}\right) \quad (1.13)$$

known as *Purcell factor*, where Γ_μ and Γ_0 are respectively the decay rate of the emitter coupled to the cavity mode μ and the natural emitter linewidth. Here, λ is the vacuum wavelength and n is the refractive index of the medium where the emitter is embedded, while V is defined by eq. (1.12). This fundamental result shows that the emission rate can be considerably improved whenever the ratio Q/V is large compared to the inverse volume of a cubic wavelength $(\lambda/n)^3$. This result, which can be obtained via a semiclassical model of the dipole-field interaction, assumes that the dipoles are perfectly aligned in space, spectrum and polarization with the cavity field and that both exhibit a Lorentzian response.

The physical interpretation of eq. (1.13) can be appreciated in the framework of first order time-dependent perturbation theory. It can be shown, indeed that the quantity Q/V is proportional to the density of final states (DOS) for the dipole *excited*→*ground* state transitions. If the DOS is reduced from the optimal value, for instance if the emitter is spectrally detuned from the optical resonance, the value of DOS is also remapped [29]. In the case of a narrow emitter, for instance, eq. (1.13) becomes:

$$F_P(\omega) = \frac{3}{4\pi^2} \left(\frac{2\pi c}{n\omega_0} \right)^3 \left(\frac{Q}{V} \right) L(\omega) \quad (1.14)$$

where $L(\omega)$ is the (normalized) Lorentzian response of the cavity centered at frequency ω_0 defined by eq. (1.9). A modified spectral (or spatial) distribution of the DOS can be thus exploited not only to enhance, but also to inhibit the natural spontaneous emission rate of a dipole emitter [2, 30].

Finally, we remark that Purcell's theory of spontaneous emission is accurate under the assumptions of a weak coupling between field and emitter. The main approximation involved here, which justifies the use of Fermi golden rule in the derivation Purcell factor, consists the assumption that any photon emitted is not reabsorbed (*weak coupling regime*). This is not true anymore for large values of the coupling rate (*strong coupling regime*): under these condition, a full quantum model, which includes the quantization of the electromagnetic field *and* of the emitter is required [31, 9].

1.2. Light-matter interaction

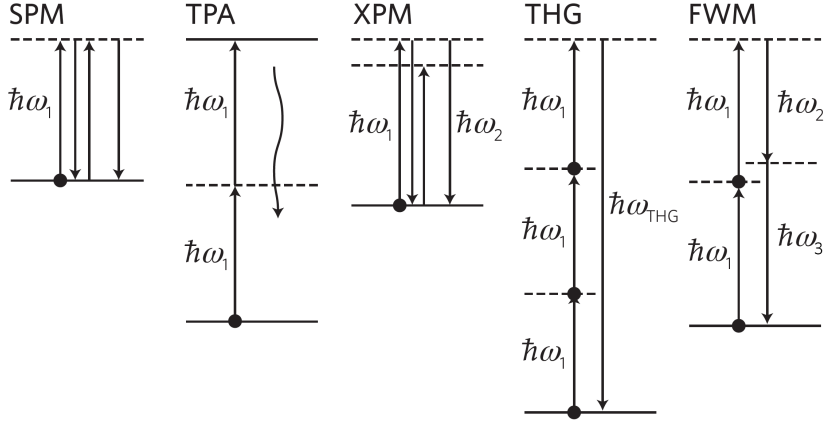


Figure 1.13: Energy level diagram for selected dipolar third-order nonlinear processes observable in silicon. From left to right: self-phase modulation (SPM), also known as Kerr effect, two-photon absorption (TPA), cross-phase modulation (XPM), third-harmonic generation (THG) and pump-degenerate four-wave mixing (FWM) [32].

1.2.2 Nonlinear processes

So far, we restricted our attention to linear dielectric media with zero or negligible losses. The linear response of a medium is described at a macroscopic level by the dielectric susceptibility tensor $\chi_{ij} = \varepsilon_{ij} - 1$ and the polarization vector $\mathbf{P} = \mathbf{D} - \varepsilon_0 \mathbf{E} = \varepsilon_0 \bar{\bar{\chi}} \mathbf{E}$. In order to model the nonlinear response of the medium, the relation between the \mathbf{P} and \mathbf{E} can be expanded in Taylor series [33]:

$$P_i = \varepsilon_0 \left(\chi_{ij}^{(1)} E_j + \chi_{ijk}^{(2)} E_j E_k + \chi_{ijkl}^{(3)} E_j E_k E_l + \dots \right) \quad (1.15)$$

where $\chi_{ij}^{(1)}$, $\chi_{ijk}^{(2)}$ and $\chi_{ijkl}^{(3)}$ are the first-, second- and third- order susceptibility tensors. Owing to the intense fields characteristic of atomic systems, a nonlinear response becomes appreciable only for high values of the electromagnetic field, typically of the order of $E \sim 10^5$ V/m. As a result of the nonlinear response, the interaction with a material can produce new frequency components. Moreover, if the susceptibilities are real, there is no exchange of energy with the medium, and the process can be modeled respectively as a

three- and four-photons interaction among respectively, for the $\chi^{(2)}$ and $\chi^{(3)}$ processes. In particular:

- Second order or processes include sum- and difference-frequency generation (SFG and DFG). A special case of the first is second harmonic generation (SHG) or frequency doubling. It is important to remark that the second order susceptibility tensor is non-zero only within a medium with lack of inversion symmetry. This can be for instance a crystalline solid or an interface between nonlinear dielectric. The $\chi^{(2)}$ processes consist either in the annihilation of one high energy *pump* photon and the generation of a pair of lower energy *signal* and *idler* photons (DFG) or in the reversed process (SFG). In both cases, the energy conservation condition implies $\omega_p = \omega_s + \omega_i$.
- Third order processes (fig. 1.13) include third-harmonic generation (THG) and four-wave mixing (FWM), where two photons are annihilated to create a signal-idler pair ($\omega_{p,1} + \omega_{p,2} = \omega_s + \omega_i$). The special case where the four frequencies coincide is at the origin of Kerr effect (or self-phase modulation, SPM), which consists in a modulation of the refractive index dependent on light intensity. Finally, the process of two-photon absorption (TPA) is modeled by the imaginary part of $\chi^{(3)}$.

Higher order interactions can also be considered, but their significance is typically low compared to leading order ones as far as the amplitude of the field is low compared to the atomic fields $E_a \sim 10^{10}$ V/m.

From a classical perspective, the nonlinear response can be deduced by introducing in eq. 1.15 terms which oscillate harmonically:

$$E(t) = E_{\omega_1} e^{i\omega_1 t} + E_{\omega_2} e^{i\omega_2 t} + E_{\omega_3} e^{i\omega_3 t} + c.c. \quad (1.16)$$

where *c.c.* denotes the complex conjugate. Limiting our attention to the third-order response $P^{(3)}$, we can write:

1.2. Light-matter interaction

$$\begin{aligned}
P^{(3)}(t) &= 3\varepsilon_0\chi^{(3)} [|E_{\omega_1}|^2 E_{\omega_1} e^{i\omega_1 t} + c.c.] && \text{SPM} \\
&+ 6\varepsilon_0\chi^{(3)} [(|E_{\omega_2}|^2 + |E_{\omega_3}|^2) E_{\omega_1} e^{i\omega_1 t} + c.c.] && \text{XPM} \\
&+ \varepsilon_0\chi^{(3)} [E_{\omega_1}^3 e^{i3\omega_1 t} + c.c.] && \text{THG} \\
&+ 3\varepsilon_0\chi^{(3)} [E_{\omega_1} E_{\omega_2} E_{\omega_3} e^{i(\omega_1+\omega_2+\omega_3)t} + c.c.] && \text{FWM} \\
&+ 3\varepsilon_0\chi^{(3)} [E_{\omega_1} E_{\omega_2} E_{\omega_3}^* e^{i(\omega_1+\omega_2-\omega_3)t} + c.c.] && \text{FWM} \\
&+ \dots
\end{aligned}$$

We omitted for clarity permutations and analogous interaction terms. The label XPM refers to cross phase modulation, namely a variation of the refractive index induced by other frequency components. The SPM and XPM terms are also responsible for TPA if a complex $\chi^{(3)}$ is considered. The above expressions do not take into account the spatial distribution of the field, and they describe the polarization vector only for a single point in space. In practice, the generated field is characterized by a phase distribution which depends on the one of the exciting fields. In order for a frequency conversion process to be efficient, a *phase-matching condition* has to be satisfied, in order to ensure that the phases of the processes interfere constructively. For plane waves, the phase matching condition can be interpreted as the conservation of photon's momentum. For instance, for a FWM process the following equality be satisfied:

$$\hbar\mathbf{k}_1 + \hbar\mathbf{k}_2 = \hbar\mathbf{k}_3 + \hbar\mathbf{k}_4 \quad (1.17)$$

In this picture, FWM makes possible the generation of new frequencies (except for the third-harmonic), in the presence of at least two frequency components. A more sophisticated model, based on the quantization of the electromagnetic field, shows that the generation of new frequency components can be observed even in the presence of a monochromatic field. The

effect, known generically as *parametric fluorescence*, can be interpreted as a consequence of the vacuum fluctuations associated to the field, which cover all the electromagnetic spectrum [29, 34]. For this reason, nonlinear processes capable to generate new frequencies are often distinguished in *stimulated* and *spontaneous* ones, distinguishing the cases where the processes are triggered respectively by a classical field or the quantum optical vacuum.

An analogous picture can be drawn for second order processes: here, the spontaneous counterpart of DFG is usually referred to as *spontaneous parametric down-conversion* (SPDC).

An important distinction between $\chi^{(3)}$ and $\chi^{(2)}$ processes is that “self-effects” (SPM and XPM) are in the latter case not allowed, unless one of the fields involved is static or quasi-static (Pockels effect).

The nonlinear materials treated in this work are isotropic. We will especially focus on the case of silicon, which is characterized by a cubic lattice with diamond-type crystalline structure. The presence of inversion symmetry forbids $\chi^{(2)}$ effects in the bulk material, while the isotropic properties of the diamond lattice make only 2 components of the $\chi_{ijkl}^{(3)}$ tensor, $\chi_{1111}^{(3)}$ and $\chi_{1122}^{(3)}$, independent and different from zero [33, 35]. Instead of the susceptibility, the nonlinearity of silicon is usually quantified in terms of the *nonlinear refractive index* (or *Kerr coefficient*) n_2 , which describes the dependence of the refractive index as a function of light intensity:

$$n(I) = n_0 + n_2 I + i \frac{\lambda}{4\pi} (\alpha_0 + \beta_{TPA} I) \quad (1.18)$$

For linear polarization, this is related to the nonlinear susceptibility via the relation:

$$n_2 = \frac{3}{4n_0^2 \varepsilon_0 c} \Re \left\{ \chi_{eff}^{(3)} \right\} \quad (1.19)$$

where $\chi_{eff}^{(3)}$ is an effective third-order coefficient which depends on the non-zero components of the susceptibility tensor [35]. With the growth of silicon photonics, this value has been accurately measured by several authors, via the *z-scan* technique. The value $n_2 = 4.4 \times 10^{-18} \text{ m}^2/\text{W}$ at $\lambda = 1.54 \text{ }\mu\text{m}$ is

1.2. Light-matter interaction

reported by Dinu *et al.* [36], which corresponds to $\chi_{eff}^{(3)} = 1.9 \times 10^{-19} \text{ m}^2/\text{V}^2$.

Equation (1.18) also models the linear and two-photon absorption. In semiconductors, this phenomenon consists in the creation of an electron-hole pair consequent to the annihilation of two photons. The phenomenon is possible only if the sum of the photons' energy is sufficient to promote an electron to the conduction band, namely $\hbar\omega > E_{gap}/2$, which is the case for light at telecom wavelength in silicon. The TPA coefficient is related to the imaginary part of the third-order effective susceptibility via the relation:

$$\beta_{TPA} = \frac{3\omega}{4n_0^2\varepsilon_0c^2} \Im \left\{ \chi_{eff}^{(3)} \right\} \quad (1.20)$$

and its value at telecom wavelength is $\beta_{TPA} = 0.8 \text{ cm/GW}$. More in general, the imaginary part (TPA coefficient) of the third-order susceptibility tensor is related to the real part (nonlinear index) via Kramers-Krönig type relations [37].

The model described so far provides a description of a nonlinear response without investigating its physical origin, which for semiconductors lies mainly in the anharmonicity of the Drude-Lorentz type response of the material charge carriers. Without entering in the details of the model (see e.g. [33] for reference) we observe that the electronic response occurs on timescales of the order of $\sim 10^{-15} \text{ s}$, comparable to the optical cycle, and they therefore can be considered instantaneous in most cases.

On the other hand, in the presence of linear and nonlinear absorption, the creation of free carriers may affect the optical response of the material. Although these processes are not intrinsically linked to the nonlinearity of the material, they can be interpreted and described as effective nonlinearities. The most important contributions on the dispersive properties of the medium are given by the variation of the refractive index associated to a variation of the concentration of free carriers, which we will refer as *free carrier dispersion* (FCD), and by the *thermo-optic* (TO) effect, associated to the local increase in temperature and consequent variation of refractive index due to the recombination of electron-hole pairs or to scattering events involving a

photon and a free carrier (*free carrier absorption*, FCA).

Nonlinear absorption and dispersive effects

We will briefly review the theory of nonlinear absorption processes and the related dispersive effects. Further details are left, where needed, as complementing discussion to each chapter.

The intensity dependent absorption coefficient of a semiconductor medium can be written as:

$$\begin{aligned}\alpha(I) &= \alpha_0 + \alpha_{TPA} + \alpha_{FCA} \\ &= \alpha_0 + \beta_{TPA}I + \sigma_{FCA}N(\mathbf{r})\end{aligned}\tag{1.21}$$

where $\sigma_{FCA} = \sigma_e + \sigma_h$ is the free carrier cross-section and $N(\mathbf{r})$ the electron-hole pair concentration. In stationary or quasi-stationary regime and in the absence of charge diffusion, $N(\mathbf{r})$ depends on the local field intensity and it is a function of the linear absorption and TPA coefficients. However, in general, nonlinear absorption and associated dispersive effects are related in a non-trivial way to the dynamics of any macroscopic quantity affecting the optical properties, such as carriers, phonons and heat flow.

For an optical microcavity, it is convenient to model absorption effects as independent decay channels which contribute to degrade the overall the Q factor, in way which in general depends on the cavity energy $U = \frac{Q}{\omega_0}P_{coupled}$. Following the models detailed in refs. [38, 39], these affect the natural (linear) cavity linewidth Γ_0 expressed in eq. (1.11) via the relation:

$$\Gamma(U) = \Gamma_0 + \Gamma_{TPA}(U) + \Gamma_{FCA}(U)\tag{1.22}$$

Similarly, an intensity-dependent expression for Q can be stated. A self-consistent model of equations, which describes the effect of the decrease in Q with the power on the coupling efficiency $\eta_c(U)$ and which includes the dependence of U on $Q(U)$ and $\eta_c(U)$ can also be formulated. For sake of clarity, we will neglect those feedback effects, unless required for a proper formulation, as their consequences are relevant only for high field intensities.

1.2. Light-matter interaction

An analogous treatment can be carried out for dispersive effects, which result in a shift of the resonant frequency. In first order perturbation theory, the (normalized) resonance shift can be expressed as follows:

$$\frac{\delta\omega_0(U)}{\omega_0} = -(\Delta\bar{n}_{Kerr} + \Delta\bar{n}_{FCD} + \Delta\bar{n}_{TO}) \quad (1.23)$$

where $\Delta\bar{n}$ represents the normalized shift $\frac{\Delta n(\mathbf{r})}{n(\mathbf{r})}$ averaged over the cavity mode volume:

$$\Delta\bar{n} = \frac{\int \left(\frac{\Delta n(\mathbf{r})}{n(\mathbf{r})}\right) n^2(\mathbf{r}) |\mathbf{E}(\mathbf{r})|^2 d^3\mathbf{r}}{\int n^2(\mathbf{r}) |\mathbf{E}(\mathbf{r})|^2 d^3\mathbf{r}} \quad (1.24)$$

The three contributions considered, Kerr effect (which is associated to a red-shift in silicon), FCD (blue-shift) and TO (red-shift), affect differently the overall shift, depending on the intracavity energy, the carrier lifetime and the thermal properties of the system.

Two-photon absorption

Applying the expression (1.21) to a given field distribution, the local time-averaged TPA loss rate can be written as:

$$\gamma_{TPA}(\mathbf{r}) = \frac{1}{2} \varepsilon_0 c^2 \beta_{TPA}(\mathbf{r}) |\mathbf{E}(\mathbf{r})|^2 \quad (1.25)$$

which can be related to the overall TPA rate by integrating over the whole space:

$$\begin{aligned} \Gamma_{TPA}(U) &= \frac{\int \gamma_{TPA}(\mathbf{r}) n^2(\mathbf{r}) |\mathbf{E}(\mathbf{r})|^2 d^3\mathbf{r}}{\int n^2(\mathbf{r}) |\mathbf{E}(\mathbf{r})|^2 d^3\mathbf{r}} \\ &= \xi_{TPA} \left(\frac{c^2}{n^2} \beta_{TPA} \right) \frac{U}{V_{TPA}} \end{aligned} \quad (1.26)$$

where ξ_{TPA} and V_{TPA} are respectively an overlap factor between the mode and the nonlinear material and an effective mode volume for the nonlinear

process. They are defined as follows:

$$\xi_{TPA} = \frac{\int_{cavity} n^4(\mathbf{r}) |\mathbf{E}(\mathbf{r})|^4 d^3\mathbf{r}}{\int n^4(\mathbf{r}) |\mathbf{E}(\mathbf{r})|^4 d^3\mathbf{r}} \quad (1.27)$$

$$V_{TPA} = \frac{(\int n^2(\mathbf{r}) |\mathbf{E}(\mathbf{r})|^2 d^3\mathbf{r})^2}{\int n^4(\mathbf{r}) |\mathbf{E}(\mathbf{r})|^4 d^3\mathbf{r}} \quad (1.28)$$

where the integral at the numerator in the former expression is performed over the volume of the nonlinear material, i.e. the semiconductor constituting the cavity in the assumption of a linear response from the cladding. In order to maximize the light-matter interaction, the field distribution should be such that $\xi_{TPA} \approx 1$ and $V_{TPA} \sim (\lambda/n)^3$.

Free-carrier absorption

The presence of free-carriers in a PhC cavity can be due to several factors. While the presence of ionized shallow dopants in the original SOI has usually a negligible effect (typically $N_{A,D} < 10^{16} \text{ cm}^{-3}$), the presence of crystalline defects, dislocations and surface states typically yields localized electron or hole states which may exhibit absorption under the gap energy, and increase the concentration of free carriers. Although scarce scientific literature exists on this topic, it is common belief that the fabrication process plays a major role in the introduction of these imperfections [40, 41, 42], also as a consequence of the large surface-to-volume ratio which is peculiar of PhC structures and of their fabrication process. For sufficiently high field intensities, a significant contribution to the population of free-carriers is given by TPA, which generates electron-hole pairs that quickly relax to the bottom (top) of the conduction (valence) band. Since in general the absorption from free carriers is a scattering process which is linear with the field intensity, as described by eq. (1.21), the decay channel that it introduces can be effectively either linear with respect to U , if the free-carriers are generated by scattering from localized defects, or $\propto U^2$ in the case where they result from TPA.

1.2. Light-matter interaction

Whatever the physical origin of the free carrier population, their effect can be described by a simple Drude model, where the optical loss rate at position \mathbf{r} is described by a cross-section:

$$\gamma_{FCA}(\mathbf{r}) = \frac{c}{n} \sigma_{FCA}(\mathbf{r}) N(\mathbf{r}) \quad (1.29)$$

where $\sigma_{FCA} = \sigma_e + \sigma_h$ is the sum of an electron and hole scattering cross-section. In general, the free carrier density $N(\mathbf{r}, t)$ is a spatially dispersive function of the carriers dynamics and it is affected by carrier-carrier scattering effects, such as Auger recombination. In order to simplify the model, we will describe these properties with a recombination time τ_r and we will neglect carrier diffusion, assuming $N(\mathbf{r})$ to be locally proportional to the carrier generation rate. With these assumptions, the local carrier density reads:

$$N(\mathbf{r}) = \frac{\tau_r}{\hbar\omega_0} \left(p_{lin}(\mathbf{r}) + \frac{p_{TPA}(\mathbf{r})}{2} \right) \quad (1.30)$$

where $p_{lin}(\mathbf{r})$ is the density of linearly absorbed power and $p_{TPA}(\mathbf{r})$ is the absorbed power density associated to TPA. They can be expressed as:

$$\begin{aligned} p_{lin}(\mathbf{r}) &= \frac{1}{2} \varepsilon_0 c n(\mathbf{r}) |\mathbf{E}(\mathbf{r})|^2 \alpha_0(\mathbf{r}) \\ p_{TPA}(\mathbf{r}) &= \frac{1}{2} \varepsilon_0 n^2(\mathbf{r}) |\mathbf{E}(\mathbf{r})|^2 \gamma_{TPA}(\mathbf{r}) \end{aligned} \quad (1.31)$$

where $\alpha_0(\mathbf{r})$ is the linear absorption coefficient. The overall FCA rate can then be expressed as:

$$\begin{aligned} \Gamma_{FCA} &= \frac{c\tau_r}{2n\hbar\omega_0} \frac{\int \sigma_{FCA}(\mathbf{r}) \left(\frac{\gamma_{TPA}(\mathbf{r})}{2} + \frac{c}{n} \alpha_0(\mathbf{r}) \right) \varepsilon_0 n^4(\mathbf{r}) |\mathbf{E}(\mathbf{r})|^4 d^3\mathbf{r}}{\int n^2(\mathbf{r}) |\mathbf{E}(\mathbf{r})|^2 d^3\mathbf{r}} \\ &= \xi_{FCA} \left(\frac{c^3 \tau_r \sigma_{FCA} \beta_{TPA}}{2n^3 \hbar \omega_0} \right) \frac{U^2}{V_{FCA}^2} + \xi_{TPA} \left(\frac{c^2 \tau_r \sigma_{FCA} \alpha_0}{n^2 \hbar \omega_0} \right) \frac{U}{V_{TPA}} \end{aligned} \quad (1.32)$$

The two addends in the last expression represent the contributions to FCA from the TPA-generated carriers and from the carriers produced by linear

absorption, in the absence of diffusion effects. Since the second rate scales linearly with the cavity energy, the mode volume and the overlap factor are the same as TPA. The mode volume and overlap factor for TPA-related FCA are given by:

$$\xi_{FCA} = \frac{\int_{cavity} n^6(\mathbf{r}) |\mathbf{E}(\mathbf{r})|^6 d^3\mathbf{r}}{\int n^6(\mathbf{r}) |\mathbf{E}(\mathbf{r})|^6 d^3\mathbf{r}} \quad (1.33)$$

$$V_{FCA}^2 = \frac{(\int n^2(\mathbf{r}) |\mathbf{E}(\mathbf{r})|^2 d^3\mathbf{r})^3}{\int n^6(\mathbf{r}) |\mathbf{E}(\mathbf{r})|^6 d^3\mathbf{r}} \quad (1.34)$$

Kerr effect

The local index shift induced by Kerr effect can be expressed as:

$$\Delta n_{Kerr}(\mathbf{r}) = n_2(\mathbf{r}) \frac{1}{2} \varepsilon_0 c n |\mathbf{E}(\mathbf{r})|^2 \quad (1.35)$$

which, by averaging on the cavity volume, can be related to an overall energy-dependent shift:

$$\Delta \bar{n}_{Kerr}(U) = \xi_{TPA} \frac{c n_2}{n^2} \frac{U}{V_{TPA}} \quad (1.36)$$

which follows the same scaling pattern of the TPA process.

Free-carrier dispersion

The dispersion introduced by electron-hole pairs can be quantified, in a Drude model as:

$$\Delta n_{FCD}(\mathbf{r}) = -\zeta(\mathbf{r}) N(\mathbf{r}) \quad (1.37)$$

1.2. Light-matter interaction

where $\zeta(\mathbf{r})$ is a material parameter² and the minus sign accounts for the blue-shift of the resonance.

The normalized contribution to the modal index change is given by:

$$\Delta\bar{n}_{FCD}(U) = -\xi_{FCA} \left(\frac{c^2\tau_r\zeta\beta_{TPA}}{2n^3\hbar\omega_0} \right) \frac{U^2}{V_{FCA}^2} - \xi_{TPA} \left(\frac{c\tau_r\zeta\alpha_0}{n^2\hbar\omega_0} \right) \frac{U}{V_{TPA}} \quad (1.38)$$

where we again the two terms of the equation represent two separate contributions to the free-carrier population.

Thermo-optic effect

A local increase in temperature of the medium induces a typically positive increase in the refractive index. In the case of silicon this amounts to $\alpha_{Si} = \frac{\partial n_{Si}}{\partial T} = 1.8 \times 10^{-4} \text{ K}^{-1}$ [43] at room temperature and it is mainly related to the acoustic phonon bands population. In a PhC cavity, a local increase in temperature is directly related to the absorption of power, which can be originated by the absorption of light through any of the mechanisms described above. In order to simplify the model, we assume that the increase in temperature is approximately uniform over the whole localized mode, which is true as long as the mode size is much smaller compared to the typical heat diffusion length³. In this model:

$$\Delta\bar{n}_{th}(U) = \xi_{TO} \left(\frac{1}{n} \frac{dn}{dT} \frac{dT}{dP_{abs}} P_{abs}(U) \right) \quad (1.39)$$

²In a Drude model, $\zeta = \zeta_e + \zeta_h$, where the electron/hole contributions are given by $\zeta_{e,h}(\omega) = \frac{e^2}{2m_{e,h}^* \varepsilon_0 n \omega^2}$, where $m_{e,h}^*$ is the effective mass. Due to screening effects, the actual FCD is more precisely given by $\Delta n_{FCD} = -\zeta_e N_e - (\zeta_h N_h)^{0.8}$. We will neglect for simplicity this correction throughout the text, and include it in the numerical results whereas needed.

³The diffusion length is given by $L_d \sim \sqrt{\frac{\kappa\tau}{c}}$, where κ is the thermal diffusion constant, c is the specific heat and τ is a characteristic time. In the case of silicon is $L_{th} \gg \lambda$ for characteristic times $\tau > 1 \text{ ns}$.

where:

$$\xi_{TO} = \frac{\int_{cavity} n^2(\mathbf{r}) |\mathbf{E}(\mathbf{r})|^2 d^3\mathbf{r}}{\int n^2(\mathbf{r}) |\mathbf{E}(\mathbf{r})|^2 d^3\mathbf{r}} \quad (1.40)$$

is the confinement factor. The absorbed power is related to the cavity energy via the relation:

$$P_{abs}(U) = [\Gamma_{abs} + \Gamma_{TPA}(U) + \Gamma_{FCA}(U)] U \quad (1.41)$$

The result of TO effect also depends on the factor dT/dP_{abs} , which depends on the cavity geometry and can be estimated numerically or experimentally. The last equation shows how the absorbed energy depends either linearly or nonlinearly on the physical process producing heat. Typically, at low power the TO shift is due to linear absorption (Γ_{abs}), which produces a red-shift linearly proportional to the incident power, while at larger $P_{coupled}$, the nonlinear effects dominate. Note that, according with this model, at very high cavity energy the TO effect due to FCA will produce a shift cubic in the cavity energy ($\propto U^3$), which will eventually dominate on any other resonance-shift effect.

A comparison of estimated linear and nonlinear contributions to absorption and dispersion is shown in fig. 1.14.

The theory presented here is valid at stationary or quasi-stationary (i.e. CW pumping) regime. In these conditions, it is impossible to discern the entity of each dispersive effect (for instance, Kerr and TO effect) without relying on any a priori knowledge of the system properties. On the other hand, the time scale of each process may significantly differ. In particular, the electronic response, which is at the origin of Kerr effect, FCD, FCA and TPA is characterized by a response time of the order of $10^{-15} \div 10^{-13}$ s [39] (specifically, the Kerr/TPA interaction has a timescale of 10^{-15} s, while the carrier relaxation time is $\sim 10^{-13}$ s), and it can be considered instantaneous

1.2. Light-matter interaction

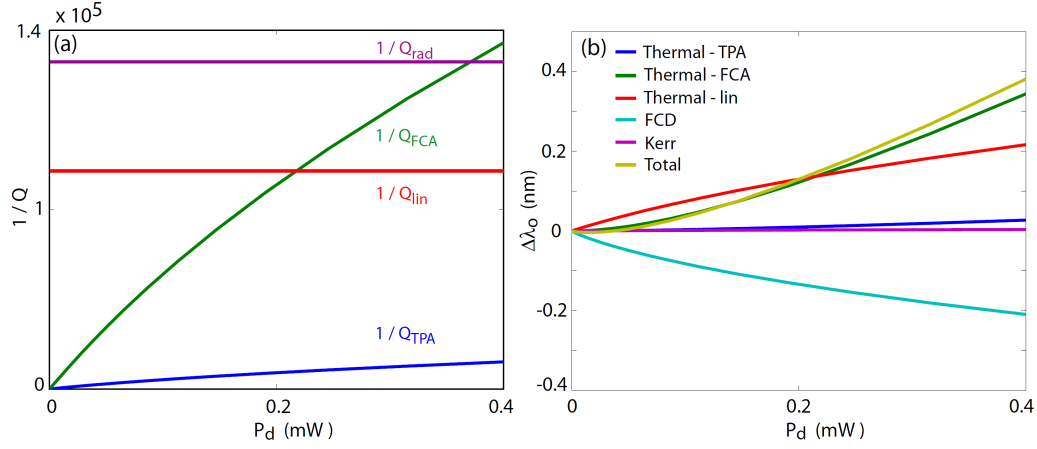


Figure 1.14: (a) Simulated decay rates for different loss mechanisms as a function of power dropped into the cavity. (b) Contributions from the different dispersive processes to the cavity resonance wavelength shift as a function of power dropped into the cavity. Numerical model and figure from ref. [38]. The FCA effects due to linear absorption are not included in this calculation.

as long as it is much smaller than the photon dwelling time. Because of their quick response time, free carrier effects have been successfully exploited for the demonstration of ultrafast all-optical switches [44, 45], with switching times of the order of $50 \div 300$ ps. This is ultimately limited by the free carrier recombination time, which in PhC cavities is of the order of 100 ps, dramatically reduced thanks to the high surface-to-volume ratio. It should be remarked that some authors [38] suggest a strong dependence of the carrier relaxation time on the carrier density N , as a consequence of carrier-carrier scattering events (fig. 1.15).

In contrast, TO effects are characterized by typical response times $\tau_{th} \sim 100$ ns. Due to the extremely small mode volume of PhC, this value is significantly smaller than other thermo-optical switches, and its application has also been proposed for all-optical control [46]. On the other hand, the ultrafast operation of PhC cavity is not susceptible of TO effects, due to the intrinsically slower thermal response, and it can be exploited to study the dynamics of FCA, FCD and Kerr effect in a separate fashion.

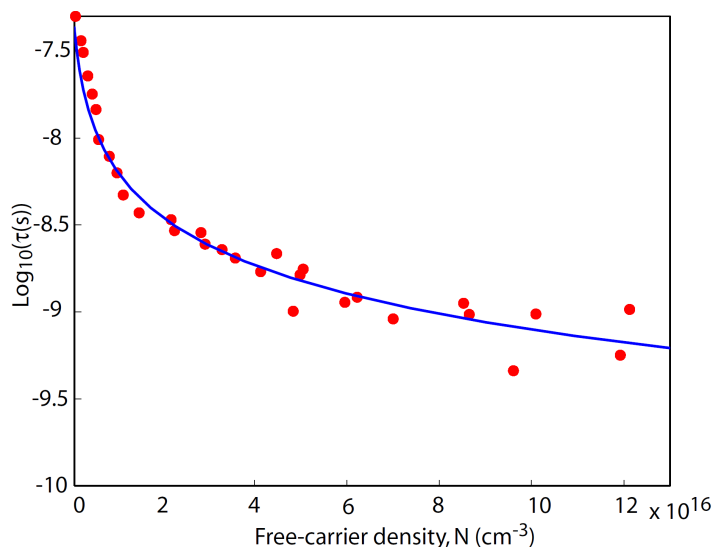


Figure 1.15: Estimated carrier lifetime as a function of the free carrier concentration for a silicon PhC crystal cavity. Numerical model and figure from ref. [38].

1.2.3 Optical bistability

The dispersive effects described so far carry important consequences on the dynamic response of PhC cavities. As aforementioned, the nonlinear optical response has been successfully exploited to mediate the all-optical switching of photonic signals. These applications rely on the fast modification induced by a nonlinear effect of the cavity resonance wavelength, which dynamically introduces a transmission or absorption window. At this regime, the PhC cavity usually exhibits *optical bistability*, which can also be exploited for the implementation of dynamic optical memories [28].

The phenomenon of optical bistability can be described as follows. In the presence of a power-dependent dispersive effect, the optical scan of a resonant mode produces a shift which is proportional to the input power. If the scan is performed in the direction of the shift (say, from blue to red for a Kerr-type effect), the coupled power induces an increase of the resonance wavelength which is more and more pronounced as the scan approaches the resonance peak. At this point, the coupled power is maximized, and for larger wave-

1.2. Light-matter interaction

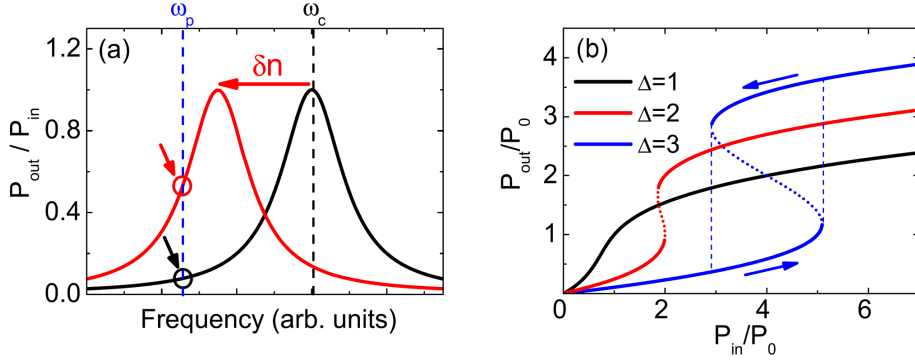


Figure 1.16: (a) Effect of a Kerr-type nonlinearity on a PhC cavity driven by an input power P_{in} . The presence of the nonlinearity under blue-detuned pumping results in an increase of the output power. (b) Transition from non-bistable to bistable regime as a function of the detuning parameter Δ [25].

lengths the resonance will switch back towards the original (“cold cavity”) resonance frequency ω_0 . The overall result is a characteristic asymmetric response of the system, which entity depends on the coupled power and on the entity of the nonlinearity involved.

This behavior is driven by a feedback mechanism for which the amount of the resonance shift depends on its previous physical states, exhibiting memory of the previous states. At sufficiently large input powers, this can result practically in an hysteretic response, which is experimentally observed as a discrepancy between spectroscopic measurements performed in different directions (blue to red, or vice versa). This behavior is schematically shown in fig. 1.16.

In the presence of a shift proportional to the coupled energy (Kerr-type nonlinearity), it can be shown [26, 25] that the system response is described by the following expression:

$$\frac{P_{out}}{P_{in}} = \frac{1}{1 + (\Delta - P_{out}/P_b)^2} \quad (1.42)$$

where $P_{in,out}$ are the input/output power to a loading channel of the cavity, P_b is a characteristic power which sets the scale of the bistable process to occur and Δ is the detuning parameter:

$$\Delta = 2Q \frac{\omega_0 - \omega}{\omega_0} \quad (1.43)$$

The expression (1.42) is a third-order polynomial equation in P_{out} . For small powers ($P_{out} \ll P_b$), the spectral response reduces to a Lorentzian, while for large input powers, the solution reveals a typical saw-tooth shaped response (fig. 1.17). Moreover, it can be shown that for $\Delta > \sqrt{3}$, the equation allows three distinct solutions (fig. 1.16b), two of which are stable and observed by scanning the resonant spectrum in each of the possible directions, giving rise to the hysteretic response. The third solution is unstable and cannot be observed practically [47].

The power scale P_b represents the power required to induce a significant shift of the resonant mode, which has to be of the order of a linewidth. This feature benefits directly from the intensity enhancement introduced by the confinement, which scales as V/Q , and is also reduced as soon as the linewidth is reduced: ultimately $P_b \propto V/Q^2$. In the presence of a Kerr nonlinearity, it can be shown rigorously [26] that:

$$P_b = \frac{V_{TPA}}{Q^2 \max(n_2/n^2)} \frac{\omega_0}{4c} \quad (1.44)$$

Fig. 1.17 shows a typical experimental spectrum obtained for high coupled power in a “dispersion adapted” (DA) PhC cavity [48]. By probing the spectrum with increasing input powers, the resonant scattering spectrum (see chapter 2) exhibits a crossover from the symmetric Lorentzian response to the characteristic saw-tooth response which characterizes bistability. The solid lines represent the best fit of the experimental signal obtained by analytically solving eq. (1.42) with respect to $P_{out}(\omega, P_{in})$ and taking the solution with maximum value. Although this model is suited for the accurate description of a Kerr-type nonlinearity, its validity can be extended to the case where the entity of higher-order nonlinear effects is small compared to the overall shift. The lower panel shows the resonance wavelength extrapolated from best fit of the experimental data with this model, showing a linear behavior corresponding to an overall shift of ~ 4 pm/ μ W, while a small superlinear

1.2. Light-matter interaction

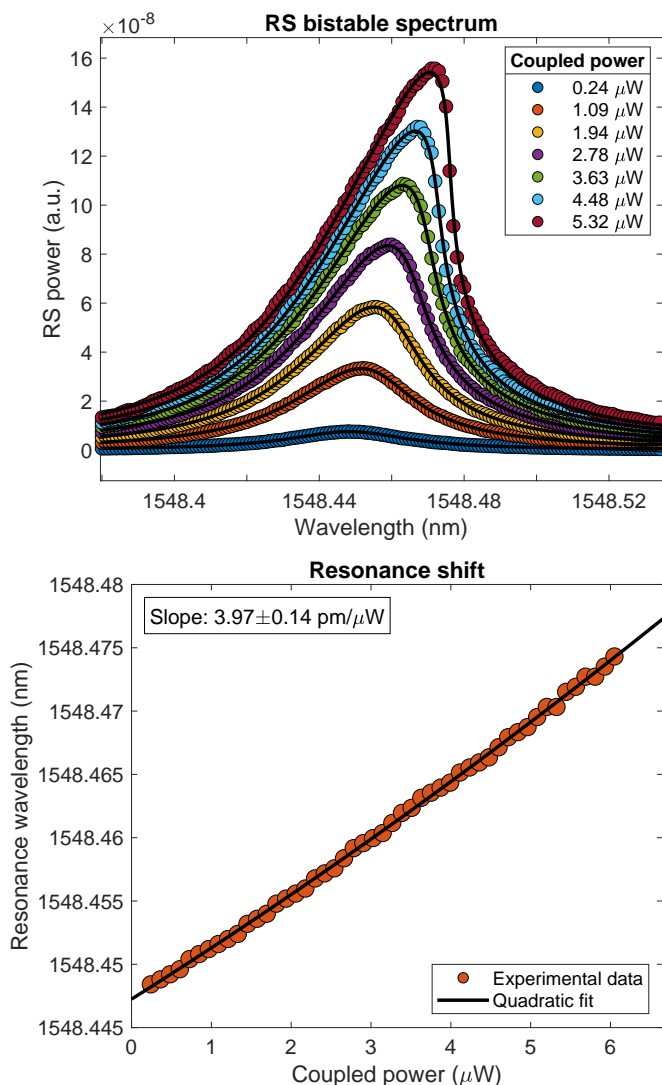


Figure 1.17: Experimental RS response (upper panel) of a far-field optimized DA cavity, with $Q = 40,000$. The data show a crossover trend from a symmetric, Lorentzian-type lineshape to a strongly asymmetric response, associated to the nonlinear behavior mainly due to TO effect. The scan is performed from lower to higher wavelength. Solid lines are best fit of the experimental data obtained with a bistability model associated to a Kerr-type nonlinearity (see main text). Note that the maximum shift at high power is well above the bistability threshold $\Delta = \sqrt{3}$. (lower panel) Estimated resonance shift obtained from best fit of the RS spectra. The points are fitted with a second order polynomial, and the value associated to the linear term (slope) is shown. A slight superlinear contribution is also appreciable, although limited by experimental accuracy at low power.

contribution, which is expected to become significant at high coupled power, is also appreciable.

Chapter 2

Experimental methods

The fast and reproducible fabrication and testing of experimental samples is an essential requirement for the realization and optimization of PhC devices. Here we review the nanofabrication processes exploited for this work and the spectroscopic techniques adopted for the study of the optical properties of PhC cavities.

2.1 Fabrication

We detail here the main processing steps for the fabrication of planar PhC cavities at the state of the art. Further details related to this topic can be found in refs. [49, 50, 51].

2.1.1 SOI wafer

The fabrication of planar PhC structures starts from thin membranes of high-quality semiconductor material. This essential requirement has been satisfied thanks to the development of electronic industry, which mature production processes have provided support for photonic devices as a by-product. In particular, silicon foundries developed the standard of silicon-on-insulator (SOI), which consists in a platform where a thin layer (of the order of ~ 200 nm) of Czochralski silicon is laid on the top of an amorphous silica (SiO_2)

buffer (thickness $\sim 3 \mu\text{m}$), in turn placed on the top of a thick substrate of crystalline silicon. In the years, SOI wafers have become a standard *de facto* and they are made available for the industry and for educational purpose. The fabrication procedure of a SOI wafer via SmartCut technique¹ is schematized in fig. 2.1. A thick wafer of Czochralski silicon is first thermally oxidized in order to create the silica buffer. Then, the surface of the wafer is bombarded by hydrogen ions (H^+), at a specific depth, in order to create a local damage inside the wafer. The wafer so processed is then flipped and bonded to a second wafer, which will act as substrate. The weak layer located at the mean depth of implantation of hydrogen ions is then used as cleavage plane. The resulting system is the SOI, which is diced in wafers and smoothed by chemical and mechanical polishing (CMP) in order to minimize the roughness. The leftover products are then recycled for the production of new SOI wafers. SOI wafers with standard thickness of the silicon layer (or device layer, DL) of 220, 270, 300 nm are currently employed in the photonic industry, while the buried oxide (BOX) consisting in the silica buffer is typically either $2 \mu\text{m}$ or $3 \mu\text{m}$ thick.

2.1.2 PhC fabrication process

We describe here the general fabrication process for planar PhC cavities. In the spirit of this research work, the process was customized and optimized for the experimental application depending on the specific target, by varying the parameters here detailed and by introducing or modifying some of the processing steps. The quantitative details reported are referred to the fabrication of the samples described in chapter 3.

The main steps are summarized in fig. 2.2. The SOI material was provided by SOITEC, with a DL thickness of 220 nm and a BOX thickness of $3 \mu\text{m}$. Each processing step is described in detail in the following paragraphs.

¹SmartCut is a proprietary fabrication process [52], developed by CEA-Leti.

2.1. Fabrication

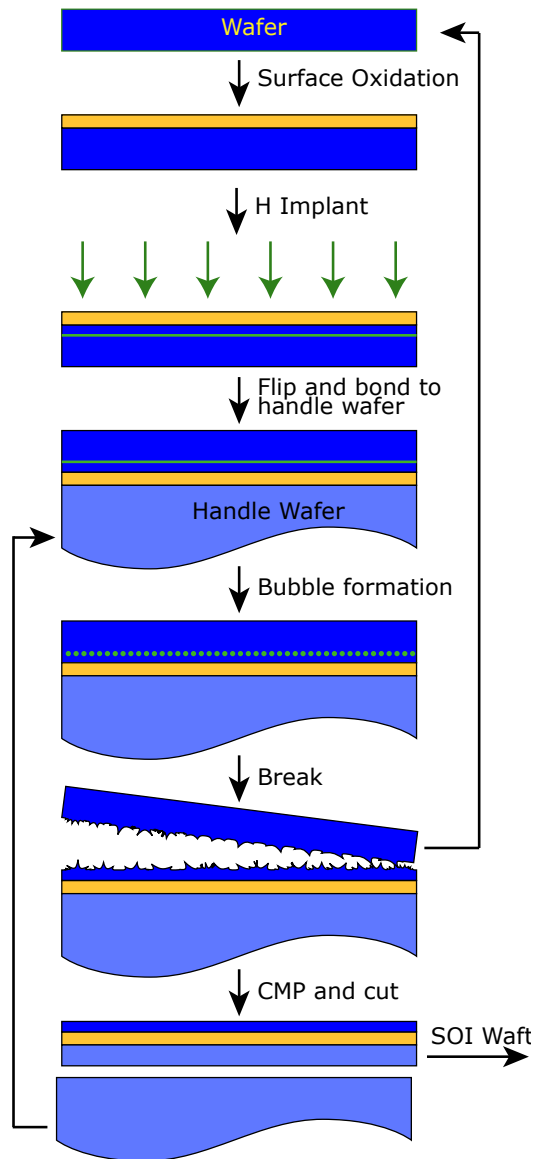


Figure 2.1: Schematic visualization of the SmartCut SOI fabrication process. The wafers are made of crystalline Czochralski silicon. The technique allows to re-use the leftover material for the iteration of the process.

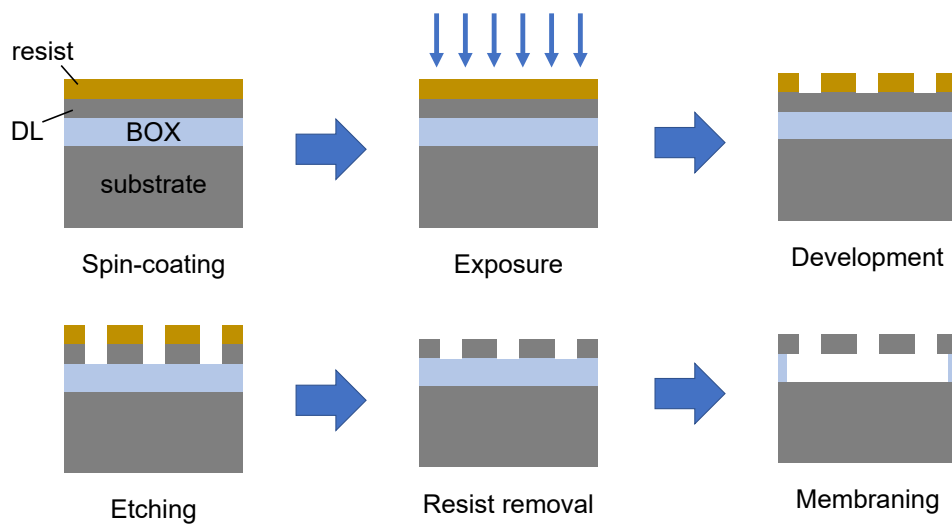


Figure 2.2: Main steps for PhC structures fabrication. First, the sample is coated with resist, then the mask is patterned by EBL and developed. The pattern is then transferred to the silicon DL by RIE and, once the leftover resist is removed, the buried oxide is dissolved by wet (HF) etching. The resulting structures consist in suspended membranes in correspondence of the patterned regions.

Resist spin coating

As a first step, the sample or the entire wafer is coated with a polymeric resist used for the electron beam lithography (EBL). A “positive” EBL resist consists in a solution of polymer molecules with a calibrated viscosity and chain length, which under bombardment by electrons is broken in smaller monomers. These can be dissolved with a specific developer: the high spatial resolution of the focused electron beam enables thus to accurately define the resist region to be removed. An e-beam resist is characterized by several figures of merit: the most relevant ones for PhC applications are the *resolution*, which sets the minimum feature size ($< \sim 5$ nm for positive resists), and the *contrast*, namely the selectivity to dry etching, which affects the verticality error obtained after the process. These features can be finely adjusted by tuning the fabrication process parameters, such as the soft- hard-bake temperature, the thickness of the layer and the accelerating voltage of the EBL system. A typical resist used for PhC fabrication is poly-methyl-metacrylate (PMMA) although novel and more performing solutions have been developed in the years.

The coating of the sample with a uniform thin layer of resist is obtained by spin-coating. After cleaning of the sample surface and chemical removal of the natural oxide, few drops of resist are deposited on the surface. Then, the spin-coater is put in rotation with angular speed of 6000 rpm for 1 minute. The final result is a uniform film of resist of with a thickness of 230 nm. The resist film is then baked on a hotplate for several minutes in order to remove the residual solvent.

Electron beam lithography

Electron beam lithography is a flexible lithographic technique which enables to achieve high resolution patterning of the spun resist. Conversely to optical lithography, where the minimum feature size achievable is mainly limited by the wavelength of the UV light employed, EBL accuracy is ultimately limited by the resolution of the resist used, with a minimum feature size of the order of few nanometers. This is usually required for the fabrication of high quality

PhC cavities, where the fabricated holes require a high resolution lithography. The main drawback lays in the long exposure time, which is limited by the maximum speed of the electron beam.

Fig. 2.3 shows the schematics of an EBL column (Zeiss Gemini). The electron beam is generated by a Schottky field-emission electron gun and accelerated by an electrostatic voltage. The steering of the beam and its focusing is actuated by a combination of electrostatic and magnetic lenses, which make possible to focus the beam to a spot size of ~ 1 nm. For imaging purpose, the beam is scanned over the surface of the sample, which is located on a moving stage actuated with high accuracy (10 nm) by using an interferometrically reference. The high-energy backscattered electrons can be detected via an in-lens detector, which is included in the electromagnetic lens system, while lower energy (~ 50 eV) secondary electrons are collected by a Everhart-Thornley type detector. The former imaging method provides an accurate visualization of the surface of the sample.

The column is part of the EBL system (Raith eLine Plus), which also consist of a high-speed pattern generator, a beam blanker and a high-speed (10 MHz) digital-to-analog converter (DAC). This hardware, used in combination with a proprietary design and fabrication software, converts the designed pattern to machine instruction, controls the electromagnetic lens and carries out the exposure of the resist.

The main parameters which characterize the exposure are the accelerating voltage and the electron dose. As reference values for PMMA resist, we used respectively 30 keV and $400 \mu\text{C}/\text{cm}^2$. Several other quantities are also relevant for a good exposure: among the others, an important role is played by the aperture size, which fixes the beam current, the writing speed, the design resolution and, in particular for holey structures, the writing mode. Another important issue to be considered is the compensation of proximity effects linked to the scattering of electrons from neighboring exposed areas. Fig. 2.3 shows the EBL machine used for part of this work.

Once the resist is exposed, the last lithographic step consists in the development, which is performed using an appropriate solvent, typically provided together with the resist. Fig. 2.4 shows an optical and a SEM picture of a

2.1. Fabrication

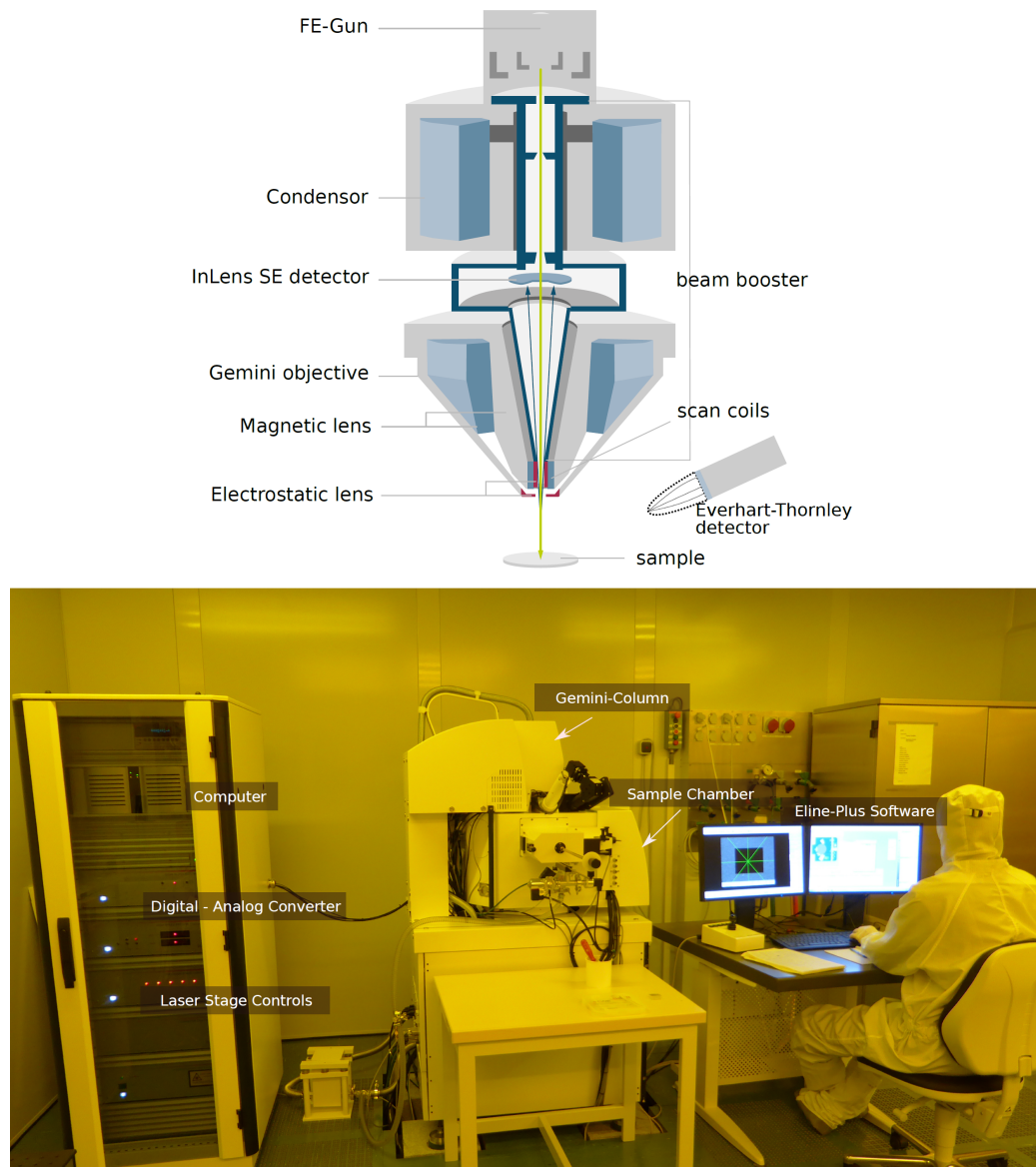


Figure 2.3: Schematic of the EBL and SEM system (Raith eLine Plus) of the Semiconductor Physics Institute of the Johannes Kepler Universität of Linz. The machine was used for the fabrication of the samples described in chapter 3. The upper panel shows the main elements of the Zeiss Gemini column, including the Schottky field-emission electron gun, the accelerating stage, the electromagnetic lens and two detectors. The lower panel shows the operating fabrication apparatus located inside the clean-room. This includes a computer-based control system, a fast DAC which converts the software-generated patterns to driving signals for the steering coils, the automatic interferometric stage control and the vacuum chamber where the writing and imaging processes are performed [51].

Recipe	Ashing	PhC etching
Temperature (°C)	-90	-90
Etching rate (nm/min)	0	55
SF ₆ (sccm)	0	2
O ₂ (sccm)	2	1
He (sccm)	300	300
ICP Power (W)	100	100

Table 2.1: Processing parameters elaborated for the ICP-RIE step. The two processes, ashing and PhC etching, are used respectively for plasma-cleaning of the sample and actual etching of the silicon device layer. Both processes are composed by multiple steps, essential for the sake of repeatability, which include chamber pre-conditioning, stabilization of temperature and gas flows, and stabilization of the plasma.

correctly exposed and developed pattern of holes.

Dry etching

The dry etching process is carried out by an inductively-coupled plasma reactive ion etching (ICP-RIE) system, which enables to transfer the exposed pattern to the DL of the SOI sample. A schematic of the machine is shown in fig. 2.5.

The sample is placed in a reactor chamber at low pressure (1 mTorr) and stabilized at a temperature of -90°C . The reactor chamber is wrapped with a RF coil driven at 13.56 MHz with power ranging from 0 to 200 W. Once the atmospheric conditions are stabilized, the chamber is filled by a constant flow of gases. For silicon etching, the gas mixture used consisted in sulfur hexafluoride (SF₆), oxygen (O₂) and helium (He), with the rates reported in table 2.1. The gases are ionized by the RF field, and the ions are accelerated towards the exposed silicon regions. The directional discharge results in an anisotropic etching action, while the reaction with silicon has two effects: the fluorine (F) ions etch the silicon, producing SiF₄ which is collected by the pumping system, while the oxygen produces compounds in the form SiO_xF_y, which catalyze the passivation of the vertical sidewalls (fig. 2.5). The latter condition is particularly favorable at cryogenic temperature.

2.1. Fabrication

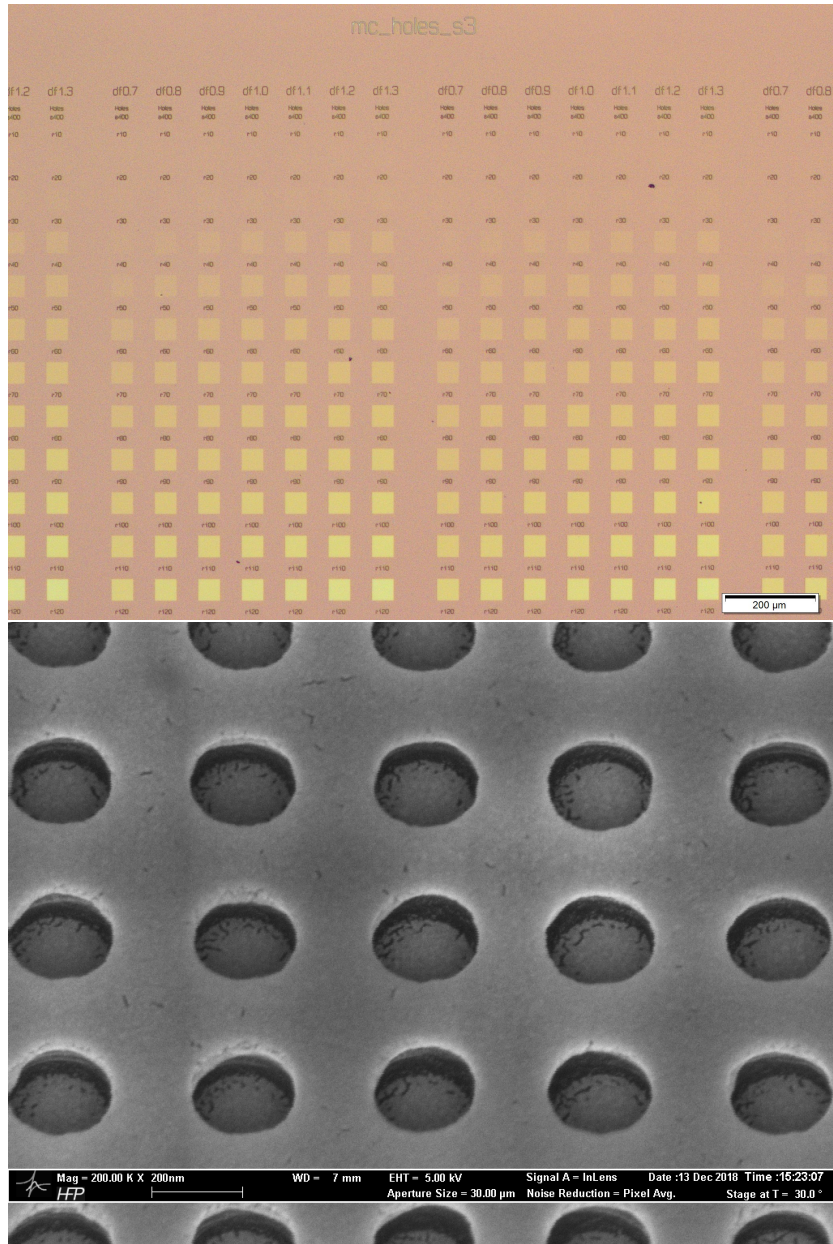


Figure 2.4: Optical (top) and SEM (bottom) images of a correctly exposed test sample, consisting of a square lattice of holes. In the left figure, a dose and lattice parameters test is performed. Correct exposure parameters were found to correspond to a dose of $400 \mu\text{C}/\text{cm}^2$ for a square lattice of holes with $a = 400 \text{ nm}$ and $r = 50 \div 120 \text{ nm}$. Right-hand figure shows the SEM picture of the same lattice, covered with a thin (1 nm) layer of gold (Au), in order to prevent the damage of the resist under electron irradiation.

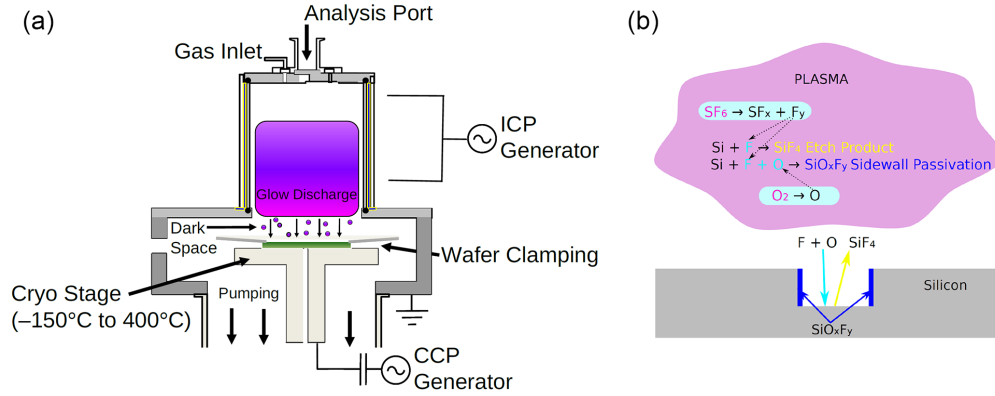
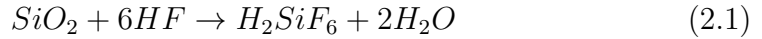


Figure 2.5: (a) Schematic and (b) working principle of an Oxford PlasmaPro System 100 ICP-RIE machine, similar to the one used for this work [51].

The side profile of an etched crystalline silicon sample is shown in fig. 2.6. The verticality mismatch with respect to the ideal condition depends on the size of the patterned holes and it is anyway kept lower than 2° .

Membrane under-etching

Before removing the leftover resist, a last processing step consists in the removal of the BOX underneath the processed DL. This is carried out by immersion in a 10% aqueous HF solution. The HF penetrates the DL and attacks the silica glass, following the chemical reaction:



The etching operation proceeds with this parameters at an average speed of 150 nm/min. Due to the capillarity effects of water, the reproducibility of the rate is strongly dependent on the processing conditions, and higher concentrations dramatically improve the etching rate. However, these tend to affect the final roughness of the silicon interfaces, and for this reason, diluted solutions are preferred.

Once the undercut is performed, the residual resist is removed with acetone and O_2 plasma cleaning at with RF power of 200 W. Finally, a dip in

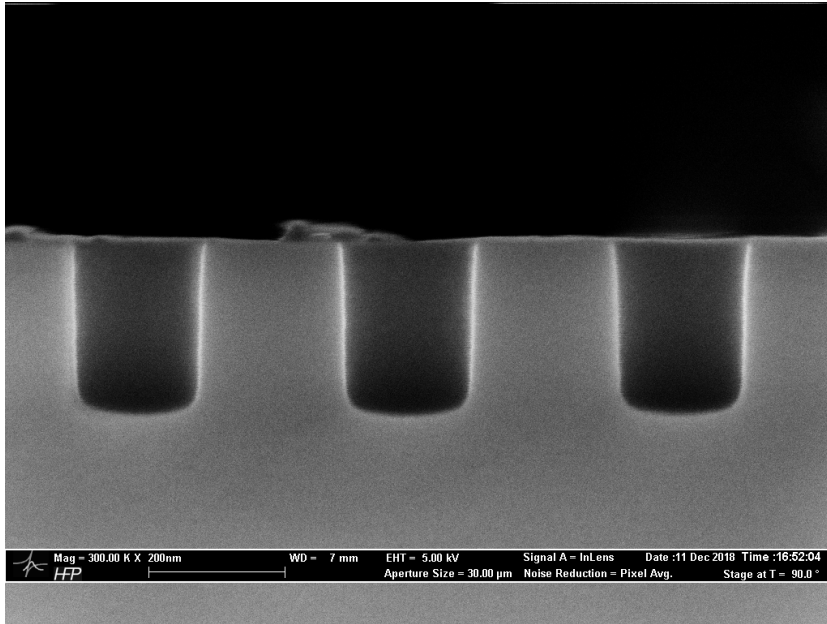


Figure 2.6: SEM cross-section of a cleaved test sample consisting in a square pattern of holes ($a = 400$ nm, $r = 100$ nm) etched in bulk silicon. Verticality mismatch is likely related to fringe effects of the ICP-RIE process.

diluted HF (1% aq. solution) removes the residual natural oxide, and slightly improves the final roughness of the silicon-air interfaces.

The final quality of the device can then be assessed by SEM imaging (fig. 2.7).

2.2 Resonant scattering

The optical characterization of PhC cavities is mainly targeted to the measurement of the resonance wavelength of confined modes and their Q factor and, secondly, on the study of their nonlinear response. The most popular experimental approaches consist in 1) characterizing the emission spectrum of the resonator, in the presence of an active medium coupled to the confined mode [53], 2) measuring the transmission (reflection) spectrum through an evanescently coupled waveguide and 3) resonantly probing the spectral response exploiting the far-field emission within the light-cone. We will here describe the latter technique, which was adopted in this work. Compared to

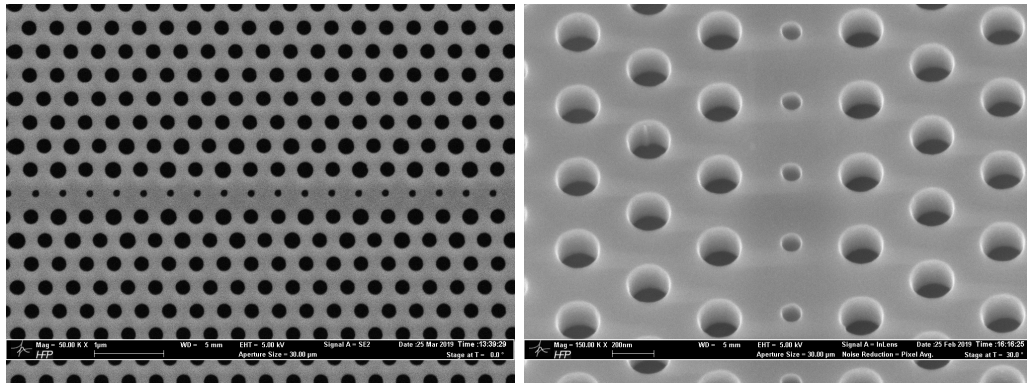


Figure 2.7: SEM images of fully processed bichromatic PhC cavities in silicon.

other spectroscopic methods, *resonant scattering* (RS) does not require the presence of emitters and does not introduce a loading effect to the cavity, which would result in a reduction of the maximum (or *intrinsic*) Q factor achievable.

2.2.1 Experimental apparatus

The experimental RS apparatus is schematized in fig. 2.8. Its first demonstration in 2005 was employed for the characterization of hexapole (H0) cavities [54] and its applicability is in general extended to any planar PhC cavity. Differently from the approach detailed in ref. [54], we adopted a reflection-based scheme [55]. In our experimental scheme, the light emitted from a tunable continuous wave (CW) laser source is linearly polarized by a high-extinction rate ($> 1 : 10^5$) thin-film polarizer (TFP) and focused on the sample by a high numerical aperture (NA) microscope objective (Nikon 50x, NA=0.8 and Nikon 100x, NA=0.9). The light reflected by the sample is collected using a 50:50 beam-splitter and analyzed by a second polarizer, which is in crossed polarization with respect to the first. Finally, the analyzed light is focused on a single mode optical fiber and detected by an InGaAs photodetector.

The working principle of RS relies on cross-polarized spectroscopy: the TE-like modes of the PhC slab, inherited by the localized resonant mode are mainly polarized in the membrane plane. Thus, by orienting the device at 45° with respect to the impinging polarization, it is possible to excite

2.2. Resonant scattering

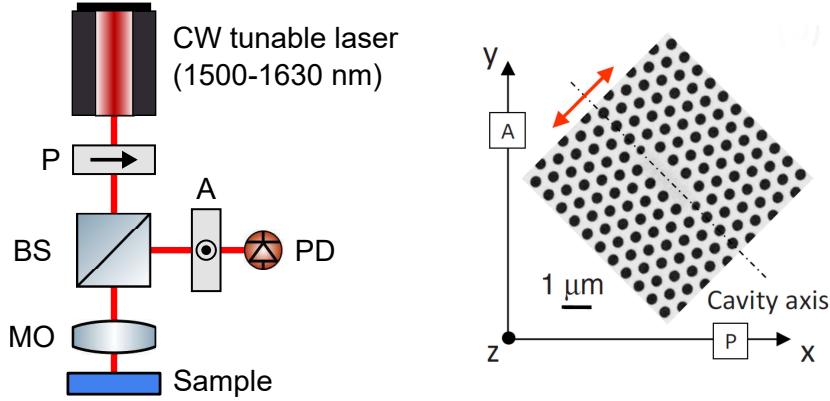


Figure 2.8: Schematic of the resonant scattering apparatus. The cavity is placed a 45° with respect to the polarization of the impinging mode (\hat{x}) and of the analyzer axis (\hat{y}). The mode polarization lays mainly along the $\hat{x} + \hat{y}$ direction.

the resonant mode. On the other hand, the light emitted will be linearly polarized in the diagonal direction, and thus part of it will be transmitted through the second polarizer. Although the efficiency in in-coupling and out-coupling to the cavity is reduced by an overall factor 2×2 , this technique enables to select the light which is actually resonantly coupled to the cavity mode and scattered back. In contrast, most of the light reflected by the PhC is not affected by a variation in the polarization, as long as the PhC pattern does not introduce (as in the case of the triangular lattice of holes) an appreciable birefringence. At the price of a reduced coupling efficiency, the RS apparatus dramatically improves the overall signal-to-noise ratio by removing any contribution from the continuum of modes constituting the reflection from the sample, and enabling to detect only the signal resonantly scattered by the cavity.

The resolution of the system is set by the accuracy of the tunable source, here a Santec TSL510 and Santec TSL710 external cavity laser (ECL), with tunable emission from 1500 to 1600 nm. For the works described here, this is of the order of 1 pm, fixed by the repeatability of the source. In order to further improve the resolution, referencing schemes based a bulk FP cavity and on reference gas absorption cells were also used, setting the ultimate limit of the setup to the laser linewidth ($\Delta\nu < 100$ kHz). The detection was performed either by amplified InGaAs photodetectors or by a liquid nitrogen

cooled InGaAs CCD array coupled to a monochromator. The latter device was used either for high sensitivity measurements and for coarse characterization of the resonance spectrum, by illuminating the sample via a broadband source (IR superluminescent LED), with a maximum resolution of 150 pm.

Fano lineshape

Fig. 2.9 shows two typical RS spectra from a L3 PhC cavity, obtained under different excitation conditions. Although one may expect a symmetric Lorentzian response, under tight focusing conditions the lineshape observed is strongly asymmetric. This phenomenology can be properly explained using the theory of interference between a continuum of states and a discrete energy level. Originally formulated by U. Fano [56], this model can be adapted to PhC cavities [55]: the resonantly scattered light (bound state) at the output of the analyzer interferes with a small background signal (continuum of states) which has the same polarization. The resulting spectrum exhibits the characteristic Fano lineshape:

$$F(\omega) = A_0 + F_0 \frac{[q + 2(\omega - \omega_0)/\Gamma]^2}{1 + [2(\omega - \omega_0)/\Gamma]^2} \quad (2.2)$$

where A_0 is a constant background factor, ω_0 and Γ are respectively the resonant mode frequency and linewidth, q is a parameter which represents the ratio between the resonant and non-resonant contributions. Depending on the value of q , the observed response can be either a dispersive asymmetric lineshape ($|q| \sim 1$) or the usual Lorentzian lineshape ($|q| \gg 1$ or $|q| \sim 0$).

The Fano lineshape (2.2) represents a good model for the RS response of PhC cavities, and it is routinely exploited as a fit function for the experimentally measured spectra. From this model it is possible to estimate ω_0 and Γ independently from the contribution of the continuum. Moreover, the product $F_0 \times q^2$ provides an estimate of the on-resonance signal from the modes, enabling to quickly compare the coupling efficiency among multiple devices.

2.2. Resonant scattering

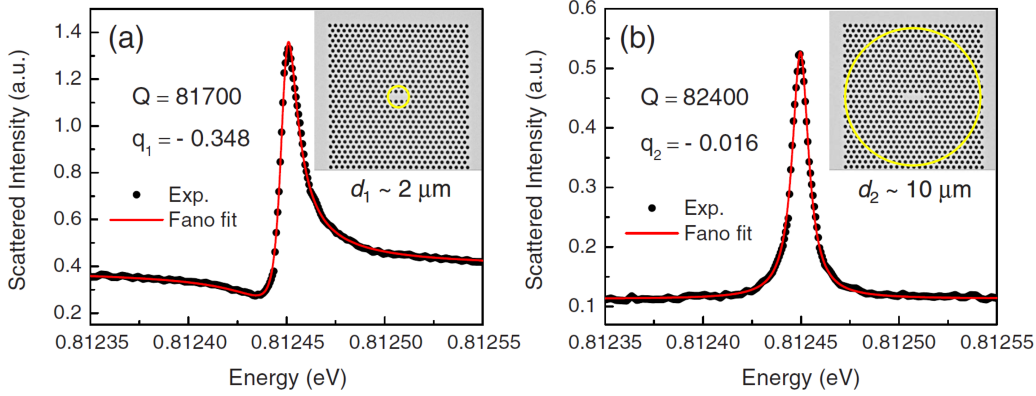


Figure 2.9: Experimental RS spectra of a L3 PhC cavity under different excitation conditions. (a) Asymmetric Fano lineshape obtained with a spot diameter $d \approx 2 \mu\text{m}$. (b) Symmetric Lorentzian lineshape, obtained with a slightly defocused spot ($d \approx 10 \mu\text{m}$) [55].

Far-field optimization

In chapter 1, we described the principle of *gentle confinement*, on which basis the Q factor of a PhC cavity can be maximized by reducing the weight of contributions to the localized mode in the k space which fall inside the light cone. A similar argument can be exploited in the opposite perspective, namely with the objective of engineering the far-field emission of the resonator in order to maximize the coupling efficiency from free-space excitation.

In this framework, the most favorable condition consists probably in the excitation orthogonal to the PhC slab plane and an almost Gaussian emission pattern, which optimizes the coupling to spatial transverse modes. Similarly to the case of grating couplers commonly used in silicon photonics [57], this condition can be obtained by means of an appropriate two-dimensional periodic pattern. In a PhC cavity, the mode profile in the reciprocal space is usually localized close to the photonic band edge, as a consequence of the gentle confinement principle: thus, an improvement of the orthogonal emission can be provided by introducing a periodicity which doubles the original one [58, 59]. Qualitatively, a doubled periodicity yields a folding of the two-dimensional BZ, for which the mode localized at the band edge is brought at the Γ point, with associated vertical emission in the light-cone.

In practice, far-field optimization is introduced as a small perturbation to the system, by increasing the size of selected holes in a way which mimics the doubled periodic pattern (fig. 2.10a). This results in a “loading” effect on the localized state, which introduces additional losses to the mode, decreasing the Q factor and improving at the same time the coupling efficiency $\eta_c := P_{coupled}/P_{incident}$. The dependence of Q and η_c on this perturbation is shown in fig. 2.10b, while the modification of the far-field emission pattern is shown in fig. 2.10c, highlighting the crossover from a regime where most of the emission is concentrated at a steep angle with respect to the plane, to a regime where this is mostly concentrated in the orthogonal direction.

The far-field optimization technique is particularly suited for RS measurements and for the experimental study of PhC cavities which require a good signal-to-noise ratio from the resonant modes and/or a high coupling efficiency, such as nonlinear experiments.

Coupling efficiency

In order to quantitatively study the nonlinear properties of PhC cavities by means of the RS apparatus, it is useful to estimate the fraction of optical power effectively coupled to the resonator. For a specific device and resonant mode, this is quantified by a coupling efficiency [60, 61], already introduced in the previous paragraph, under excitation from free-space²:

$$\eta_c = \frac{P_{coupled}}{P_{incident}} \quad (2.3)$$

Here $P_{incident}$ is the power impinging from a focused free-space Gaussian mode, which properties depend on the objective used to focus on the sample, while $P_{coupled}$ is the fraction of power effectively coupled to the confined mode. Unless otherwise specified, η_c is referred to the optimal coupling condition, namely at the spatial, spectral and polarization alignment configuration which maximize the power coupled to the localized mode.

²An alternative definition of the coupling efficiency and its relation to η_c is provided in sect. 5.3.

2.2. Resonant scattering

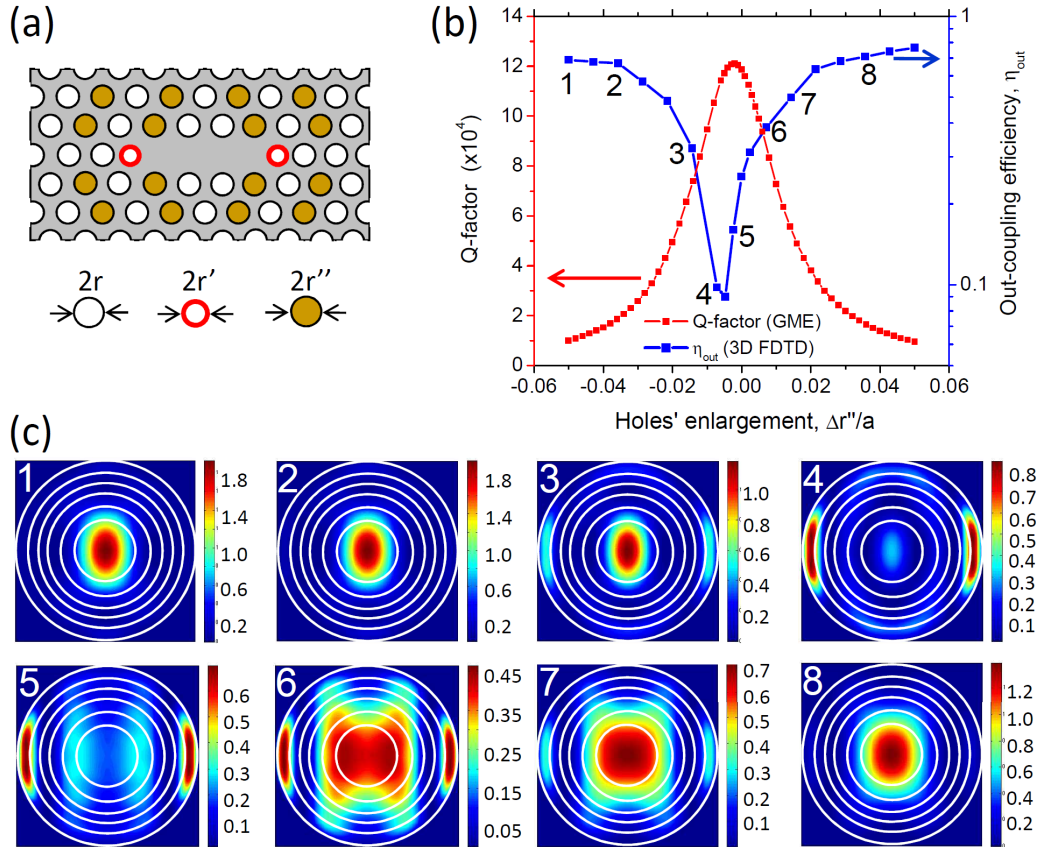


Figure 2.10: (a) Schematic of far-field optimized L3 PhC cavity. Holes marked in red are shrunk and shifted to optimize the Q factor. Dark yellow holes are modified to increase the vertical out-coupling. (b) Calculated Q factor and out-coupling efficiency ($\eta_{out} = P_{collected,obj}/P_{emitted}$) as a function of the filled holes' radius variation. (c) Calculated far-field patterns (electric field intensity profile, $|E|^2$) corresponding to the labeled numbers on the efficiency plot. Concentric circles correspond to $\theta = 20^\circ, 30^\circ, 40^\circ, 50^\circ, 60^\circ, 90^\circ$ from the inner to the outer one, respectively. Figure and model from [59].

The coupled power $P_{coupled}$ to a specific resonant mode can be easily estimated, once the incident power $P_{incident}$ (which also accounts for the setup losses from the laser source to the sample) is known, by experimentally evaluating η_c via the following procedure:

1. The RS signal P_{sample}^{RS} is measured using a tunable laser source which is spectrally matched with the resonant mode. The sample position is optimized in order to maximize the RS signal, and the device is placed at 45° with respect to the impinging polarization. The two polarizers are set in orthogonal configuration. The measurement of P_{sample}^{RS} is performed by focusing the RS signal on a free-space detector, in order to collect all the optical power from the microscope objective.
2. The sample is replaced with a high-reflectivity mirror, and the analyzer is aligned with the impinging polarization. The power P_{mirror} is measured using the same collection system as in step 1.
3. The RS signal and the signal from the reference mirror are compared, and the coupling efficiency is estimated via the formula:

$$\eta_c = 8 \frac{P_{sample}^{RS}}{P_{mirror}}$$

where the factor 8 accounts for the losses introduced by the crossed polarization (factor 4) and from the symmetric emission from the PhC membrane (factor 2).

Note that the estimation method does not account for the possible additional contribution given by the reflection from the SOI substrate. However, this is typically negligible owing to the very short Rayleigh range associated to the Gaussian beam parameters used in this work.

Part II

Results

PhC cavities for optical frequency combs

3.1 Motivation

In the last few decades, *optical frequency combs* have become a subject of great interest in photonics research [62]. Traditionally tied to the field of laser science and metrology, this branch of research has raised interest in the perspective of integrated applications made possible by the introduction and spread of microresonators [63]. The main breakthrough of this technology consists perhaps in the possibility to provide an accurate absolute reference in terms of optical frequency and it finds applications in the fields of optical clocks, precision spectroscopy, ultrafast optics, and in general all those applications which benefit from a wide spectral coverage of accurately controlled equally spaced frequency components. The shift of frequency combs towards integrated devices offers a number of benefits which are common of many other photonics technologies, such as compactness of the final device, energy efficiency and ease in high-volume fabrication. Besides, microresonators offer specific advantages to this peculiar field, such as a suitable pathway towards the increase of the free spectral range, which translates in higher repetition rates ($f_{rep} > 10$ GHz) of active devices, such as optical parametric oscillators (OPO), a difficult feature to achieve in bulk or fiber-based systems. Moreover,

integrated frequency combs are strictly related to novel applications which belong to the realm of quantum photonics, such as sources of nonclassical states of light based on spontaneous FWM processes [64, 65, 66, 67].

The generation of an optical frequency comb, namely an optical signal characterized by exactly equally spaced frequency components, and often accompanied by a well-defined phase relation, is based on the use of cavities which are characterized by a *comb-like* resonance spectrum. This condition is often encountered in optical resonators, such as in the case of the Fabry-Pérot (FP) cavity, where the condition of quantization of the wavevector translates into a set of modes $\nu_m = \frac{c}{2nL}m$ equally spaced in energy. This condition is true up to the frequency dispersion of the cavity components, namely up to the dependence of the refractive index $n(\omega)$ on the frequency. A common strategy in bulk optics is to exploit such a cavity, combined with an active medium and a nonlinear component (e.g. a saturable absorber or a modulator), to build lasers operating at mode-locking regime, which exhibit a frequency comb as emission spectrum.

The transition of this technology to the integrated domain is non-trivial, but achievable, and the purpose has stimulated the photonics research in the last years. The main obstacle towards integration is constituted by the lack of active media for on-chip applications, or their difficult implementation, which is limited to few material platforms (mainly III-V semiconductors) and often requires heterogeneous integration and a somewhat complex fabrication process. One possibility to overcome this limitation is to exploit the gain properties offered by nonlinear process, and in particular stimulated FWM, to either achieve self-sustained oscillations (OPO) or to use a seed signal to generate the frequency components constituting the comb, typically in a cascaded fashion.

The second aspect which is addressed in the integration of optical frequency combs is the requirement of a cavity with comb-like spectrum. In this framework, a major role was played by *whispering gallery mode* (WGM) microresonators, such as microtoroids, microspheres and microrings. Similarly to the case of the FP resonator, these structures are characterized by a natural condition for the uniform spacing of the cavity resonances, which

3.1. Motivation

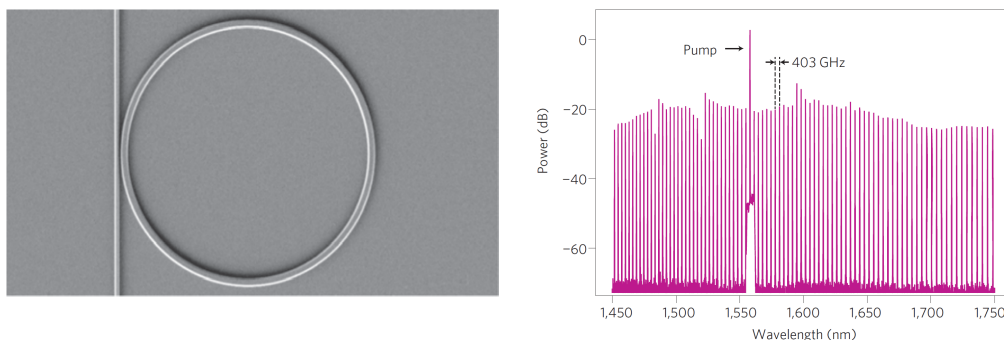


Figure 3.1: Optical parametric oscillator based on a silicon nitride microring resonator. (Left) SEM image of the SiN microring resonator ($58 \mu\text{m}$ radius, $Q = 500,000$, $FSR = 403 \text{ GHz}$) coupled to a bus waveguide, engineered to give anomalous group velocity dispersion (GVD), and thus equally spaced resonances, in the C-band and a zero-GVD point at 1610 nm . (Right) Output spectrum of the same structure used as optical parametric oscillator with a single pump wavelength tuned to resonance at 1557.8 nm . It shows numerous narrow linewidths at precisely defined wavelengths. The generated wavelengths were equally spaced in frequency, with a FSR of 403 GHz (3.2 nm) [68].

emerges from their circular symmetry and the consequent conservation of angular momentum. Moreover, especially for the case of microrings (fig. 3.1), these structures can be easily integrated with the current photonic fabrication technology in a planar layout. Very recent research has highlighted their compatibility with dielectric material platform characterized by an appreciable nonlinear response at telecom wavelength and, in some cases, a negligible detrimental contribution from TPA. On the other hand, the TIR-based confinement mechanism which is proper of this family of microresonators yields large mode volumes, which translate in high optical input powers needed to exploit the nonlinear effects required or into high Q factors, which are technology-dependent.

While the technological optimization is promising in terms of performance advances of WGM-based devices, another possibility is to exploit microresonators with smaller mode volume, such as PhC cavities, with a consequent dramatic increase of the FWM process efficiency and the reduction of the threshold for parametric oscillations. Nevertheless, this pathway sets many challenges: first of all, multi-mode PhC cavities do not provide automati-

cally comb-like resonant spectra, which constitute a necessary condition for the generation of a comb. Secondly, the tight confinement makes the in- and out-coupling somewhat more difficult than in other devices. Lastly, in contrast with travelling-wave resonators, such as WGM resonators, PhC cavities do not necessarily exhibit a full spatial overlap between different resonant modes.

Aim of this chapter is to investigate the possibility of exploiting PhC cavities to produce frequency combs, addressing the difficulties aforementioned. Here we present the design, realization and characterization of silicon PhC cavities exhibiting *comb-like* spectrum, namely a set of resonances equally spaced in energy up to the resonance linewidth. The structures here discussed are aimed to demonstrate a physical device supporting triply resonant FWM-type nonlinear processes in high Q/V microresonators. The cavity design is based on a *bichromatic* lattice, which stems from the superposition of two slightly mismatched periodic patterns and it is shown to yield multimodal localization in a single resonator, while keeping low the mode volume. After discussing the localization mechanism and the optimization of the design in terms of uniformity in the resonance spacing, we present the fabrication process and the experimental characterization of the devices. Finally, we present a strategy for the tuning of the cavity resonances based on local oxidation of the PhC membrane and show how this can be employed to compensate for fabrication imperfections and to achieve a PhC cavity supporting triply resonant FWM processes.

Details about the design and the localization mechanism can be found in ref. [69]. An early experimental demonstration of this cavity geometry was given in ref. [70], while a similar implementation of PhC cavities based on the bichromatic design and exhibiting nearly equally spaced modes was demonstrated in ref. [71].

3.2 Confinement mechanism

A schematic of the *bichromatic cavity* design is sketched in fig. 3.2a. The construction of the PhC cavity starts from a triangular lattice of holes, with

3.2. Confinement mechanism

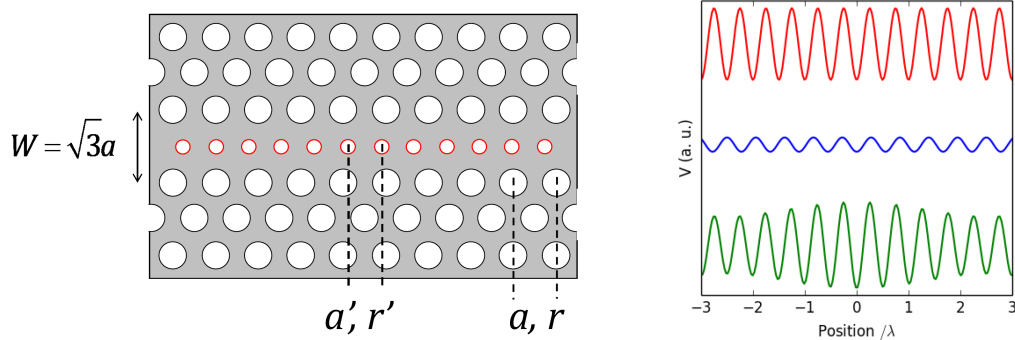


Figure 3.2: (Left) Schematic visualization of the “bichromatic” cavity: a and r represent the lattice step and hole radius of a triangular lattice of air holes (black circles), while a' and r' represent the radius and lattice constant of the one-dimensional defect lattice (red circles). Localization occurs whereas the defect lattice is shifted by $\delta = a'/2$ with respect to the main lattice. This phenomenology can be understood in terms of a superposition of two mismatched periodic lattices (left panel), which lead to a minimum of the resulting confinement potential where the “beating” between the two occurs in phase.

lattice constant a and radius r , etched in a silicon membrane of thickness t suspended in air. A row of holes is removed from this geometry and replaced with an array of smaller holes, of radius $r' < r$, and slightly smaller periodicity $a' < a$. This modification results in the superposition of two periodic dielectric lattices (in the xy -plane), characterized by a lattice mismatch $\beta = a'/a$, which also quantifies the degree of commensurability of the two lattices. In a heuristic picture, we can imagine the effective dielectric function (i.e. the confinement potential) along the line defect to be proportional to the superposition of the two periodic lattices. The resulting confinement potential (fig. 3.2b) can be thus expressed as the “beat” of the two potentials, as it will consist in a fast oscillating component with periodicity $\approx a'$, modulated by a slowly varying envelope (with periodicity $\sim a'/(1 - \beta)$):

$$\begin{aligned} V(x) &= V_1 \cos(2\pi x/a) + V_2 \cos(2\pi x/a') \\ &\approx V_{12} \cos(2\pi x/a') \cos[2\pi(1 - \beta)x/2a']. \end{aligned}$$

As such effective confinement potential shows an absolute maximum in $x = 0$, which gradually tapers down to zero as x increases or decreases, it is evident

how this configuration is capable to provide the conditions for the localization of one or more resonant modes.

A more rigorous and quantitative argument stems, once again, from a comparison with solid state theory, and it is detailed in ref. [69]. In this framework, the physics emerging from the superposition of two mismatched electronic lattices may lead to the exponential localization of electronic states, as described by the so-called Aubry-André-Harper (AAH) model [72, 73] and demonstrated experimentally in ultra-cold atoms ensembles [74]. In the context of our PhC cavity model, the role of atomic sites, corresponding to minima of the electronic potential, is replaced by the interstitial sites, corresponding to dielectric region between the holes of the line defect row. Each site is labeled by an index $j = 0, \pm 1, \pm 2, \dots, \pm N/2$ and located at position $x_j = ja'$, where N is an even positive integer, which is also used to fix the mismatch parameter $\beta = N/(N + 1)$. For values of j such that $|j| > N/2$, the main lattice periodicity is restored, namely $x_j = aj$.

With this formalism, the master equation (1.3) can be recast in the more convenient form:

$$[\omega_0^2 + \Delta \cos(2\pi\beta j)]c_j - J[c_{j-1} + c_{j+1}] = \omega^2 c_j \quad (3.1)$$

which is known as Aubry-André equation. Here, the eigenvalues ω^2 of the equation represent the resonant frequencies of the cavity, the while the eigenvectors c_j represent the coefficients of the expansion of the magnetic field \mathbf{H} in Wannier wavefunctions localized at each interstitial site $\mathbf{H} = \sum c_j \mathbf{H}_j$. The other terms appearing in eq. (3.1) represent:

- ω_0 : the central frequency of the non-mismatched line defect modeled in tight-binding approximation, which is expressed as $\omega_0^2 = c^2 \int \varepsilon^{-1} |\nabla \times \mathbf{H}_0|^2 d^3 \mathbf{r}$;
- Δ : which models the total (half) excursion of the on-site modulation potential, originating from the beat between the mismatched lattices;
- J : the tunneling term with the two neighboring lattice sites, again inherited from tight-binding approach. Assumed to be constant for

3.2. Confinement mechanism

each pair of neighboring interstitials, it can be explicitly computed as

$$J = -c^2 \int \varepsilon^{-1} (\nabla \times \mathbf{H}_{j+1}^*) (\nabla \times \mathbf{H}_j) d^3\mathbf{r}.$$

The theoretical framework provided by the AAH model reduces in practice the task of designing a PhC cavity to an appropriate choice of the parameters β , Δ and J . While the former can be chosen arbitrarily, the second two are both affected by the geometrical parameters which can be set at design, so that the easiest design strategy results in an appropriate evaluation of the defect holes radii compared to the other lattice dimensions r'/a . The central frequency ω_0 affects only slightly the Q/V figure of merit and it can be chosen to be close to the operating design frequency by an appropriate choice of the main PhC pattern (and thus of the PBG), and then later adapted via a scaling of the structure dimensions.

The localization mechanism described by the AAH, which was shown to match very well the FDTD calculations, brings about two remarkable consequences. First, the cosine-shaped confinement potential provides a natural condition for the occurrence of gentle confinement. This can be appreciated by expanding the confinement potential around its minimum:

$$V(x) \propto \frac{1}{2} \Delta \left[2\pi(1 - \beta) \frac{x}{2a'} \right]^2 \quad (3.2)$$

up to a constant. This approximately quadratic (harmonic) confinement potential yields, in analogy with the case of the quantized harmonic oscillator for massive particles, a fundamental Gaussian eigenfunction and higher order Hermite-Gauss modes. For the case of a localized electromagnetic mode, a Gaussian envelope is known to minimize the out-of plane scattering, thus providing the best achievable condition for gentle confinement and consequently high intrinsic Q factors. Secondly, it can be shown that within the same approximation, the bichromatic lattice yields mode volumes of the order of a wavelength cubed, which most importantly scale sublinearly with the size of the cavity, in particular $V \propto N^{1/2}$.

The effectiveness of the AAH model in the design of PhC cavities provided impressive results in terms of Q/V . In particular, FDTD calculations showed how the Q factor can be deliberately increased (with calculated $Q_{theory} >$

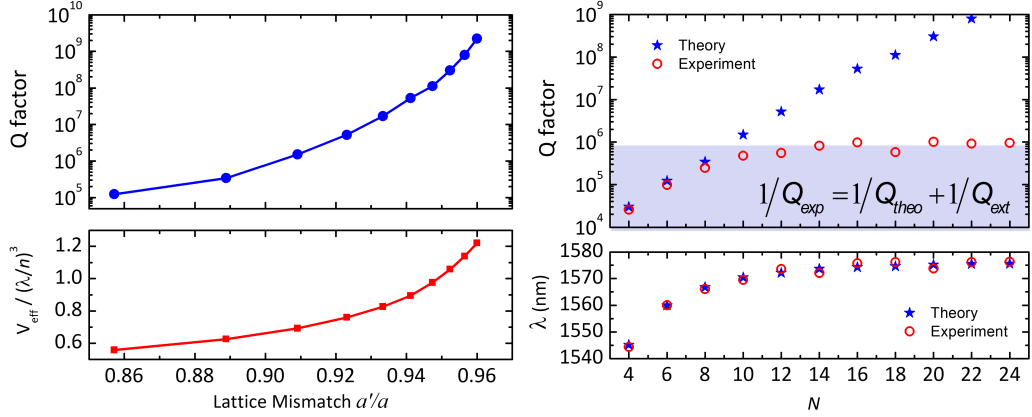


Figure 3.3: (Left) Numerically estimated (FDTD) values of quality factor and mode volume for the bichromatic cavity as a function of the lattice mismatch β . Remarkably Q factors of the order of 10^9 were estimated, with a monotonically increasing trend as a function of N . Moreover, the mode volume experiences slower growth, with a scaling trend $V \sim N^{1/2}$ [69]. (Right) Comparison between experimental and numerical data for bichromatic cavities with different N . The saturation of the experimental Q factor at $Q = 10^6$ suggests the presence of a dominating extrinsic loss mechanism, likely associated to fabrication [70].

10^{10}) by increasing N , namely for near-unit values of the lattice mismatch (fig. 3.3). At the same time, the values of V can be kept reasonably low. In practice, the bichromatic cavity provides a way to design microresonators where the Q factor is ultimately limited only by fabrication imperfections and other extrinsic losses. Fig. 3.3 shows how this contribution becomes prevalent over out-of-plane losses for increasing values of N .

A remarkable distinction exists between the original AAH model and the bichromatic cavity: while for the former exponential localization is predicted to occur only for $\Delta/J > 2$ in the most favorable conditions (namely, for irrational β), corresponding to a phase transition somehow analogous to Anderson localization, in a PhC cavity it is possible to identify localized states with high Q even at $\Delta/J \sim 0.2$. This evidence points to a substantial difference in the physics of the localization process compared to Anderson localization, which makes confinement easier than in our design.

3.2. Confinement mechanism

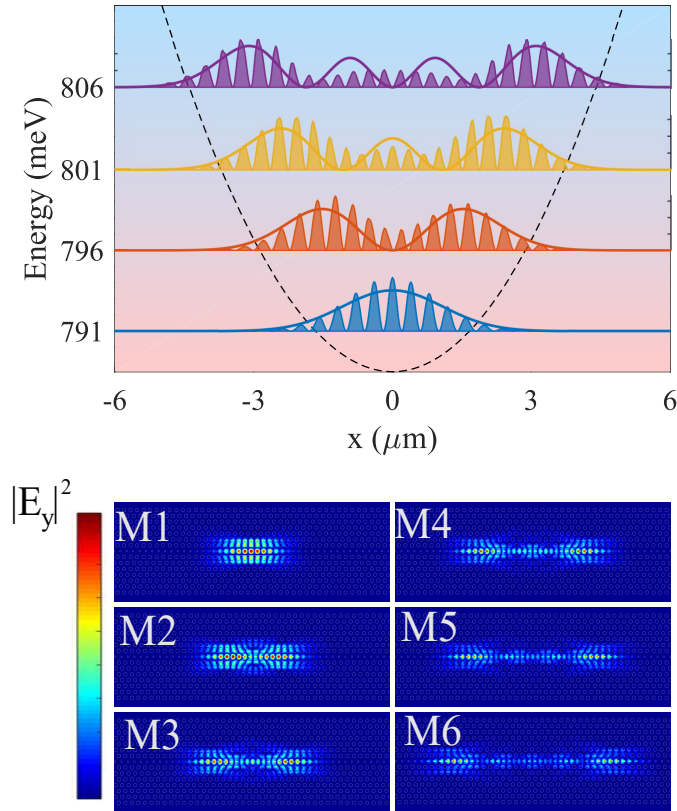


Figure 3.4: Working principle (upper panel) of the bichromatic cavity effective confinement potential. In analogy with a quantized harmonic oscillator, an approximately parabolic optic confinement potential yields Hermite-Gauss modes. Here, the envelope lines are Hermite-Gauss functions, while the filled areas are the $|E_y|^2$ component of the electric field calculated by FDTD simulations. (Lower panel) near-field distribution of the electric field intensity, as computed with FDTD.

Equally spaced modes

The physics of the AAH model provides an important insight on the multimodal behavior of the bichromatic cavity. As we already pointed out, the model provides an approximately harmonic confinement potential, which results in resonant modes characterized by an Hermite-Gauss envelope. Furthermore, the eigenvalues of eq. (3.1) are expected to be equally spaced, a condition which is reflected on the resonant frequencies ω_n , provided that $|\omega_n - \omega_{n+1}|a \ll \omega_0$, within the validity of the quadratic potential approximation. A qualitative picture of the localization mechanism is shown in figure 3.4, where the $|E_y|$ component of the electric field (FDTD calculation) for the first resonant modes is compared to the Hermite-Gauss function profile, showing a good agreement especially for lower order modes. As in the quantum-mechanical case, the spacing in energy of between resonant modes is determined by the convexity of the confinement potential and thus strictly related to β , which is perhaps the most critical design parameter. The depth Δ of the confinement potential also affects the mode spacing, and most importantly defines the range of validity of the quadratic approximation. It is worth emphasizing that the anharmonicity of the confinement potential induces a monotonous decrease in the modes spacing for higher energy values, due to the cosine-shaped term of the AAH equation. This mechanism can be however compensated via the dispersion of the line defect, which is modeled by the tunneling term J . In summary, an appropriate combination of the design parameters β , Δ and J defines the optimal conditions for the achievement of a comb-like spectrum, enabling an easy control of the design process of the spectral properties of the cavity.

3.3 Cavity design

Design parameters

The cavity geometry, superimposed on the SEM image of one of the fabricated samples is shown in fig. 3.5. As reference design parameters for our experimental demonstration, we chose a lattice constant $a = 400$ nm for a

3.3. Cavity design

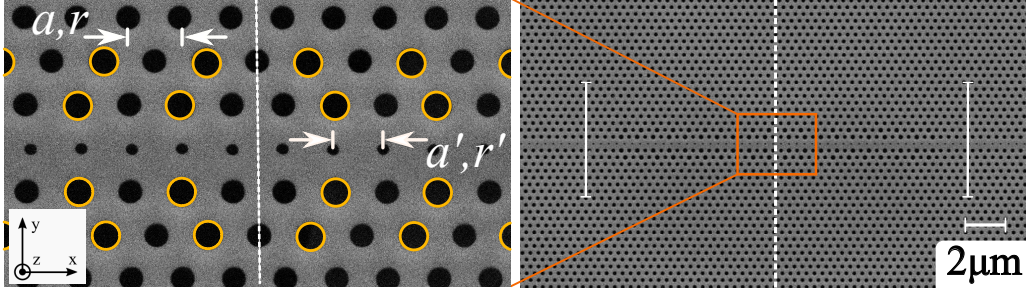


Figure 3.5: Design parameters for the bichromatic cavity designed to exhibit a comb-like spectrum with equally spaced resonances. As main differences with respect to the layout represented in fig. 3.2, here the lattice mismatch is very slight ($N = 48$) and a far-field optimization is introduced (holes marked in yellow). The vertical white solid lines in the right panel delimit the region where the line defect periodicity is mismatched with respect to the main lattice. The vertical dashed line identifies the yz -symmetry plane which determines a classification between even (antisymmetric) and odd (symmetric) order modes.

triangular lattice of holes with radius $r = 100$ nm, patterned in a suspended membrane of silicon in air with thickness $t = 220$ nm. This combination of parameters provides a main PhC lattice characterized by a 146 meV wide PBG for TE-like modes centered at 838 meV ($\lambda = 1.48$ nm, in the telecom wavelength range). We fixed a mismatch parameter $\beta = 0.98$ ($N = 48$) and we performed numerical simulations for defect holes radii ranging from $r' = 50$ nm to $r' = 80$ nm, thus probing a meaningful subset of the Δ/J parameter range. Finally, in order to both increase the visibility of the cavity modes under RS spectroscopy and to modulate the spectral linewidth of the modes, we further introduced a variation in the radius of specific holes (marked in figure 3.5) in the range $\Delta r = -4 \div +4$ nm.

FDTD results

The validity of the model was probed via full 3D-FDTD simulations, performed for different cavity parameters. As simulation parameters, we used a mesh resolution ranging from $a/20$ to $a/40$, a simulation time of 5 ps (in order to correctly isolate the high- Q modes ringdown) and PML boundary conditions.

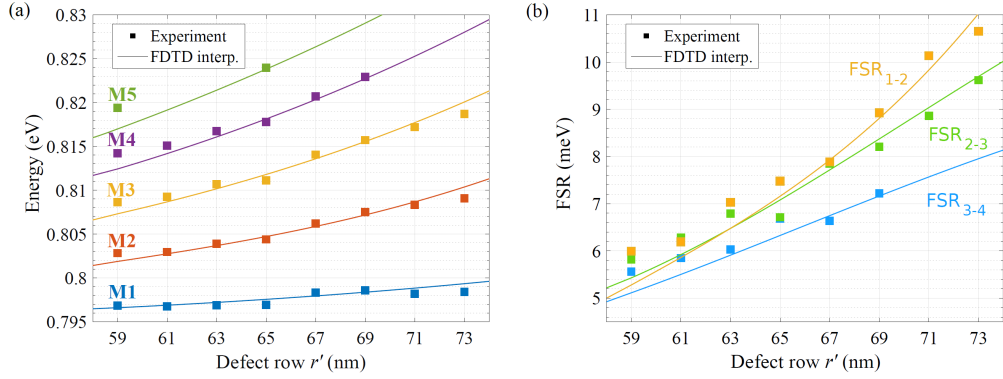


Figure 3.6: Bichromatic cavity modes dispersion (a) and FSR mismatch (b) as a function of the defect row holes radius r' . Solid lines are spline interpolations of FDTD results, while squares are experimental points obtained via high-resolution RS. The overlap of both the numerical and the experimental trends for $r' \approx 50 \div 60$ nm suggests points to the existence of a favorable region of parameters for the use of the cavities for triply resonant FWM.

The numerical analysis predicted up to 8 resonant modes with energy lying in the PBG range. The average free spectral range (FSR) related to lower order modes was found between 4 and 5 meV, as determined by Fourier transform and interpolation of the cavity ringdown. We selectively filtered the different resonances both according with parity under yz -plane reflections and with frequency, and estimated Q factors systematically higher than 10^7 for non far-field optimized cavities, by fitting the cavity ringdown using an exponential function. From a comparison with previous results, and in particular with the trend shown in fig. 3.3 it is clear how this value should be interpreted as a lower bound on the Q factor, which, especially for lower order mode, is expected to be several order of magnitude higher. An accurate numerical estimate of Q would require more sophisticated FDTD computations, which are beyond the purpose of this work. The simulation also provided an estimate for the mode volumes being of the order of $V = 2(\lambda/n)^3$. The xy -section of the mode profile for the first 6 modes is reported in figure 3.4.

A crucial insight is provided by fig. 3.6, which shows the predicted trend of the resonance energies and FSRs as a function of r' . The variation of this

3.4. Experimental results

parameter clearly affects the mode spacing (and hence Δ) in the first place, with larger values of FSR for higher r' . Secondly, the variation of r' also affects the dispersion of the modes energies, pointing to an inversion of the lowering trend for the FSR variation dictated by the anharmonicity of the potential, and highlighting the crucial role of the line defect dispersion in the determination of the modes' distribution. In particular, the second plot suggests the existence, for $r' \sim 50 \div 60$ nm, of an optimal condition where the free spectral ranges FSR_{12} and FSR_{23} (or FSR_{23} and FSR_{34}) coincide, realizing a set of three resonances with exact equal spacing in energy, namely a prototypical optical frequency comb suitable for triply resonant nonlinear applications.

3.4 Experimental results

Fabrication process

The fabrication of the devices was performed as much as possible using standard processes of CMOS technology, in a way compatible with the PhC structures. The sample processing started from a silicon SOI wafer with 220 nm thick DL and a 3 μm thick silica BOX. This platform was chosen to achieve a single TE mode slab with minimal evanescent coupling towards the substrate. The wafer was cut into 9x9 mm² chips, each of them constituting a sample. The sample fabrication procedure is detailed in chapter 2.

High resolution resonant scattering

The systematic characterization of the optical properties of the devices was carried out via RS technique associated with a highly accurate referencing of the probe wavelength. A schematic of the experimental setup is shown in fig. 3.7. The radiation emitted from the excitation laser (tunable external cavity laser, Santec TSL-710) was repeatedly swept in the 1500 \div 1600 nm wavelength range (750 \div 827 meV). The sample was stabilized in temperature ($T_{set} = 25 \pm 0.005$ °C), in order to compensate for slow thermo-optic drift of the resonant modes. The crossed polarization was collected by means of a

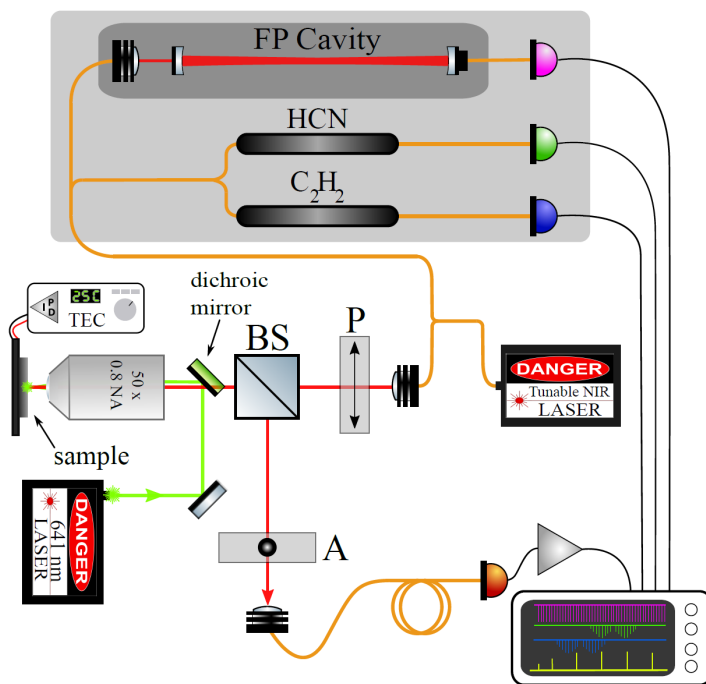


Figure 3.7: High resolution resonant scattering setup used for the accurate characterization of comb-like spectra. See main text for details.

3.4. Experimental results

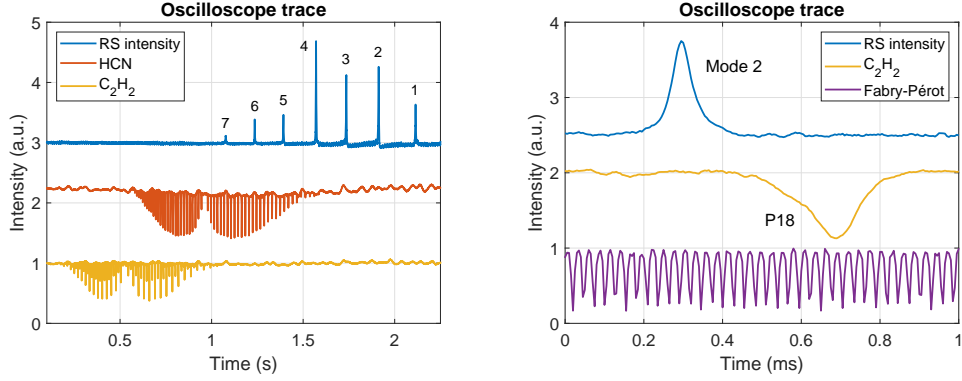


Figure 3.8: Experimental traces from the high resolution RS apparatus. The scan is performed by sweeping the laser wavelength from the blue to the red at a speed of 40 nm/s and the signal is digitized by a sampling oscilloscope. The two reference gas cells (left panel) exhibit roto-vibrational absorption spectra characterized by known absorption lines and provide both the information required for a coarse calibration and an absolute wavelength reference. The Fabry-Pérot trace (right panel) allows for the precise referencing of the measured cavity modes to the cell absorption lines. The RS spectra shown are measured on cavities with nominal parameters $a = 420$ nm, $r' = 44$ nm, $\Delta r = +21$ nm (left panel) and $a = 410$ nm, $r' = 52$ nm, $\Delta r = 0$ nm (right panel).

single mode optical fiber, in order to spatially filter only the light resonantly coupled to the microresonator. The optical signal was then photodetected and amplified using low-noise amplifiers and visualized on an oscilloscope triggered by the laser sweep. The resonant modes appear as sharp peaks with Fano lineshape in the measured signal.

With this arrangement, the absolute accuracy of the scan is substantially fixed by the accuracy of the laser source (± 1 μeV), while an accurate characterization of the devices requires an error necessarily lower than the minimum mode linewidth ($\delta E < 0.7$ μeV). In order to improve the accuracy of our system, every RS spectrum was then simultaneously acquired with the transmission spectra of two gas reference cells (low-pressure cyanide and acetylene gases, characterized by rotational-vibrational spectra, for a total of approximately 100 lines) with absorption lines ranging from 793 meV to 820 meV specified with accuracy of ± 0.05 μeV . To further extend the calibrated spectral range, we also measured the transmission through a 1 meter long air-spaced Fabry-Pérot (FP) interferometer ($\text{FSR}_{FP} = 0.6$ μeV).

Fig. 3.8 shows two examples of raw experimentally recorded trace. The acquired spectra were then automatically compared with the reference values using a linear interpolation algorithm. The combination of the two referencing strategies (gas cells and FP interferometer) enabled to evaluate the resonance energy of the cavity modes with an overall absolute accuracy of $0.2 \mu\text{eV}$.

An example of the measured RS spectra is represented in fig. 3.10, showing 6 modes unambiguously distinguishable. The average FSR measured was ranging from $\text{FSR}_{5-6} = 4.6 \text{ meV}$ for higher order modes to $\text{FSR}_{1-2} = 13 \text{ meV}$. A sample comparison of measured data with 3D-FDTD simulations for one of the devices is shown in fig. 3.6, which highlights the good agreement between the numerical estimate and the actual dispersion of the resonance energies as a function of the structural tuning parameter r'/a . For each of the multi-mode spectra acquired, we performed a Fano fit of the resonance lines, in order to estimate the resonant frequency and Q factor. Estimated values as high as $Q = 1.1 \times 10^6$ were retrieved for cavities without far-field optimization (fig. 3.9). In view of a spectral range exceeding 5 meV, this value corresponds to a finesse $\mathcal{F} = \text{FSR}/\Gamma = 8 \times 10^3$, which is among the highest values reported in the literature for integrated microresonators and the highest value achieved, to the best of our knowledge, for silicon microcavities. As a comparison, state-of-art ring resonators based on silicon nitride [75] exceed $\mathcal{F} > 3 \times 10^4$. It is worth noticing, however, that a strict parallel cannot be drawn: in the first place, the finesse does not refer, in our case, to perfectly equally spaced modes, due to the dispersion of the resonances distribution. Secondly, the quantity \mathcal{F} cannot be rigorously interpreted as a measurement of intensity enhancement as in the case of a WGM or FP resonator, as the physics of the confinement mechanism is dramatically different. Nevertheless, we believe the finesse still constitutes a valuable figure of merit for the evaluation of the potential performance of the devices in the presence of a comb-like structured spectral response such as the one discussed here.

The discrepancy between the measured value of Q and the FDTD prediction should be attributed to fabrication imperfections and induced absorption at the interfaces, which constitute the only relevant decay channels of cavities.

3.4. Experimental results

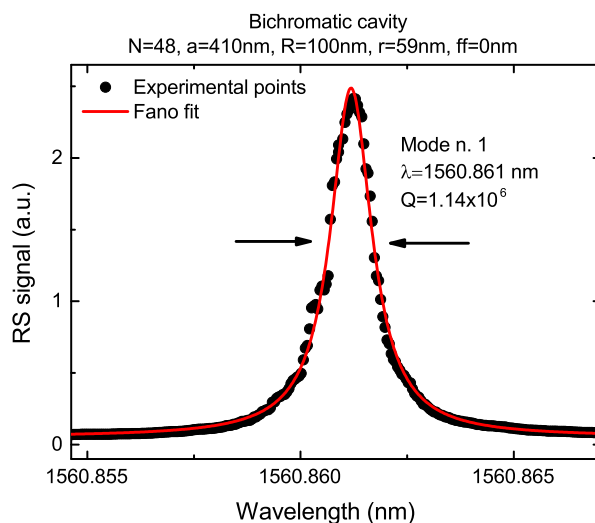


Figure 3.9: RS spectrum of one of the devices with the highest Q factor measured for this work. The resonance energy is $E_{M1} = 794.4$ meV while the spacing between the fundamental and the second resonant mode is $FSR_{1-2} = 5.65$ meV.

While the former are substantially a result of the disorder and systematic errors introduced by the fabrication process, which could up to a certain extent be optimized, the second ones are likely strongly related to the quality of the materials employed (commercial SOI) and on the chemistry of the interfaces between dielectric and air. Results obtained in analogous structures [42] suggest indeed how the natural oxidation of the silicon membrane might play a crucial role in the limitation of the maximum value of Q achievable, setting a practical limitation to technological applications of this kind of devices. In particular, the mentioned group showed how the natural oxidation present at the silicon/air interface introduces, even in the presence of a controlled inert atmosphere, a degradation in time of the Q factor within few days after the removal of the natural oxide. The analogous phenomenon was observed for the devices discussed here, where a degradation of Q from 1.1×10^6 to 0.9×10^6 was observed after repeating the RS measurement approximately one month later.

The above-million value of Q discussed above decreases to an average of 240,000 (a typical RS spectrum is shown in fig. 3.10b) for far-field optimized

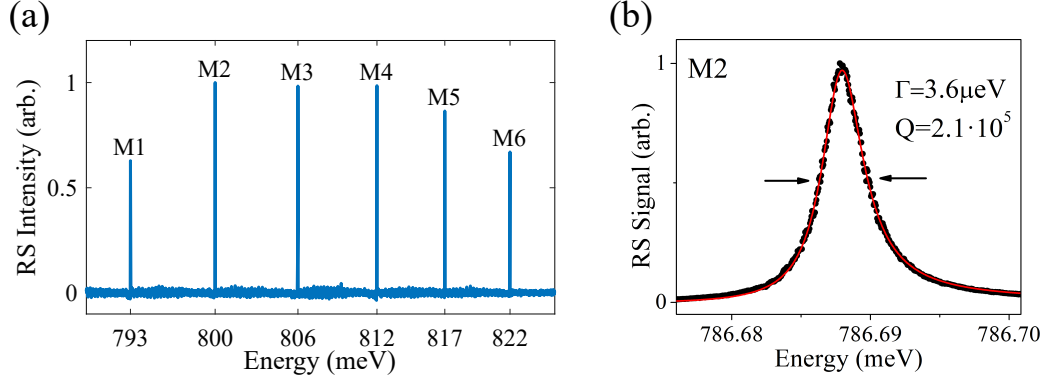


Figure 3.10: RS spectrum of a multimode bichromatic cavity engineered to exhibit comb-like spectrum. (a) Broadband response of the system, showing the first 6 resonant modes. Note the decrease in FSR for increasing mode index, as a consequence of the intrinsic anharmonicity linked to the AAH model. (b) High resolution spectrum of a typical resonant mode. The resonance showed here corresponds to mode 2 of the cavity used for the tuning demonstration.

cavities with $\Delta r = +4$ nm, which exhibit the best visibility observed in this work, as a direct consequence of the introduction of a loss channel. This affected not only the fundamental, but also higher order mode, with a slightly less pronounced effect ($\sim 5 \div 10\%$) on even order modes, likely as a consequence of a multipole cancellation effect.

The calculated and measured dispersion trends represented in fig. 3.6 suggest the possibility to find a combination of parameters for which the spacing between pairs of resonances is matched within the mode linewidth, which was the primary target of this investigation. In the perspective of non-linear applications, the high Q factor of the bichromatic design provides an enhancement in the efficiency of the nonlinear processes. On the other hand, this feature also contributes to tighten the requirement in the accuracy of the resonances' spectral alignment: as a rule of thumb, any triply resonant non-linear process would require at least three resonances equally spaced within one linewidth, in order to be appreciably efficient. In practice, even in the presence of a fine lithographic tuning of the design parameters, as performed in this case, the accuracy required to the fabrication process in the definition of the mode resonance energy ($\delta E \approx \pm 5 \mu\text{eV}$) would be by far unaccessible with the current technology, as it would require a precision σ_{holes} of the order

3.4. Experimental results

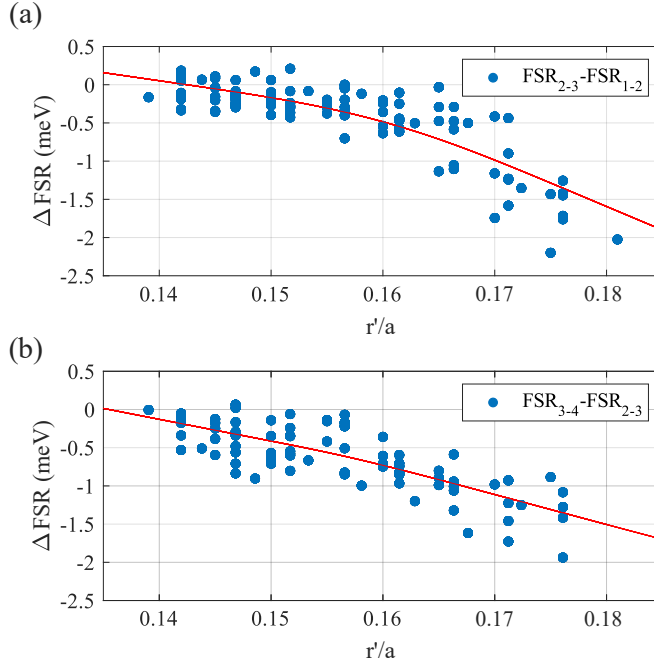


Figure 3.11: Statistics of the FSR mismatch $\Delta\text{FSR}_{i,j,k} = \text{FSR}_{j-k} - \text{FSR}_{i-j}$ for modes 1,2,3 (a) and 2,3,4 (b) as a function of the r'/a ratio over the entire poll of 106 measured devices. Red lines are guides to the eye. The wide deviation of the distribution is due either to fabrication imperfections and to the variety of design parameter for each value of r'/a . The trend suggests the presence of an optimal region where ΔFSR distributes around 0 meV for $r' \approx 50$ nm, in agreement with simulations.

of $\sigma_{holes} \approx \frac{\delta E}{E} a \approx 0.002$ nm, while the best precision reported is around 0.25 nm, and for this work we estimated $\sigma_{holes} \sim 1$ nm.

A more quantitative picture is represented in fig. 3.11, where the accumulated statistics of the FSR mismatch related to modes 1,2,3 and 2,3,4 for all the 106 devices measured on the sample is reported as a function of the r'/a ratio. The statistical deviation σ_E of the measured values is of the order of 1% of the resonance energy, which is comparable to the statistical aforementioned error in the EBL fabrication, as estimated from SEM imaging, on the design parameters.

3.5 Post fabrication tuning

The lack of a perfect alignment among at least three resonances of the comb-like spectrum constitutes a primary obstacle towards nonlinear applications. Among the possibilities to overcome this limitation, two possible solutions are 1) to deliberately increase the linewidth of the cavities by introducing a loading channel, such as a heavy far-field optimization or the coupling with a waveguide, at the cost of a reduced efficiency for any nonlinear process. Or 2) to introduce an *a posteriori* selective tuning step of one or more resonant modes with respect to the others, in order to compensate for the FSR mismatch. As we already mentioned, we already adopted the first adjustment at the design step, in order to improve the visibility of the experimental signal. Here we discuss the second technique, which was adopted on the completely processed sample.

We selected, among the measured devices, a resonator with FSR mismatch of $\Delta\text{FSR} = \text{FSR}_{3-4} - \text{FSR}_{2-3} = 6 \mu\text{eV}$ and far-field parameter $\Delta r = +4 \text{ nm}$, corresponding to a Q factor of 190,000 on all the three modes involved. By exploiting the same apparatus used for the measurements, we employed a focused visible laser (Coherent Cube, $\lambda_{ox} = 641 \text{ nm}$) to locally heat the device in order to oxidize the Si membrane as suggested by Chen *et al.* [76]. The accuracy of the oxidation process is very high and it is ultimately limited by the thermal diffusion length ($L_{th} \sim 1 \mu\text{m}$), rather than by the diffraction-limited spot size (fig. 3.12). The neat effect of this process on the first 4 cavity modes, as a function of the exposure time is represented in fig. 3.13, where the spot of the visible laser was focused at the center of the cavity. A systematic blue-shift of all the modes is observed, pointing to an overall reduction of the average effective index in the spatial volume where the modes are localized. As a main distinction in comparison to ref. [76], we notice here that the fundamental mode is the most affected by the local oxidation, while the higher order modes are systematically less affected by the process. This evidence is consistent with the predicted mode profile represented in figs. 3.4, where the mode energy is mainly located in lobes of increasing distance from the interstitial $j = 0$, constituting the center

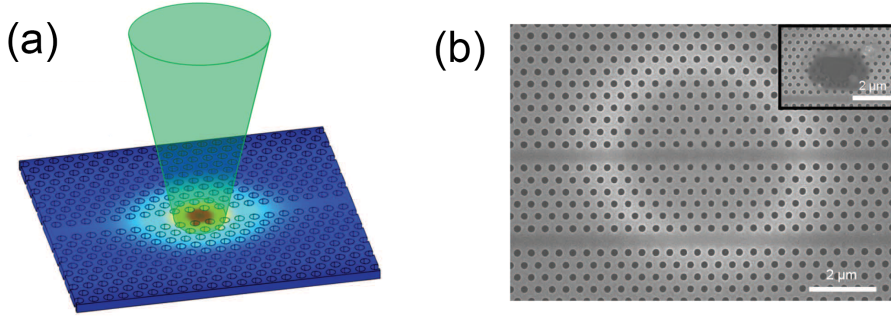


Figure 3.12: Conceptual scheme (a) and results (b) of local oxidation of a PhC silicon membrane including PhC cavity (heterostructure-type cavity in this example). The clear halo surrounding the exposed area which is observed after the exposure of a visible laser provides a quantitative picture of the extent affected by the oxidation process. This is larger than the diffraction limited spot, and results to be of the order of the thermal diffusion length $L_{th} \sim 1 \mu\text{m}$. This is even more evident from the burned region in the inset, and it is further confirmed by finite element simulations [76].

of the cavity, and can be interpreted as a first order perturbation emerging from the local variation of the refractive index $\Delta\lambda_i/\lambda_i \propto \Delta n/n$, as suggested in refs. [77, 78].

The effect of the selective tuning on the FSRs is illustrated in fig. 3.13, where the average linewidth of the two modes is visualized as a shaded area, to highlight the accuracy to which the equal-spacing condition has to be fulfilled in practice. The condition is achieved for the longest exposure times used in this work (13 min, 8 of which at a laser power of 10 mW and 5 min at 15 mW). It is worth noticing that the optical power employed, although small, is capable to provide a significant increase in the local temperature, owing to the low conductive dissipation rate of the PhC membrane compared of the bulk material. An approximate estimation¹ provides a local temperature variation of 600-800 °C, which is typical of silicon thermal oxidation processes [80]. This datum is corroborated by the fact that at higher input power (~ 30 mW), the temperature increase results in the perforation of the membrane (fig. 3.12b, inset). It should be remarked, however, that also non-thermal

¹Anticipating the formalism presented in chapter 5 (eq. 5.4), it is possible to estimate the local temperature as $\Delta T = P_{abs}/K$, where the thermal conductivity is chosen $K = 1.25 \times 10^{-5}$ W/K as reported for instance by Haret *et al.* [79].

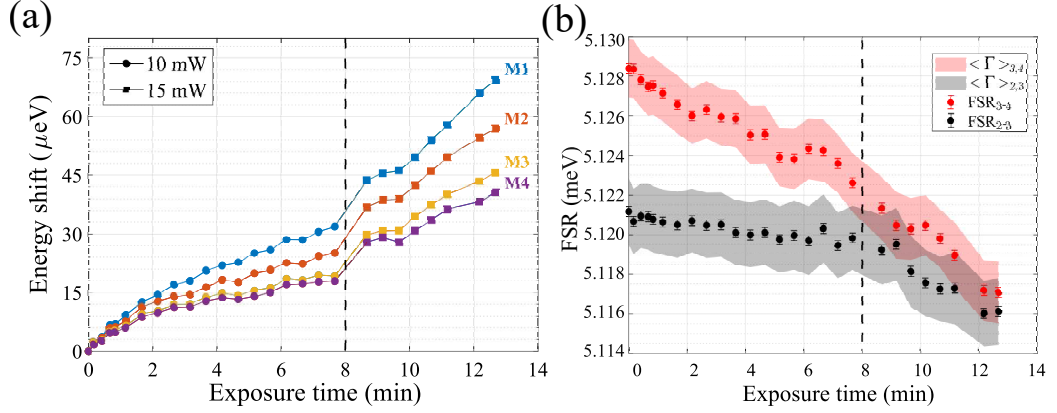


Figure 3.13: (a) Energy shift of the first 4 modes after local oxidation operated at the center of the PhC cavity. The vertical dashed line marks the increase of the oxidation power from 10 mW to 15 mW. The total shift depends on the mode order, with a more pronounced effect on lower order modes and a maximum overall shift of 69 μeV for the fundamental. (b) FSR shifts of the pairs of modes 2,3 and 3,4 exploited in the tuning experiment. The average linewidths (full width half maximum) of the pairs of modes involved are represented as shaded areas. Error bars, which are specifically evaluated for each tuning step, are systematically smaller than mode linewidths.

processes triggered by hot carriers injection) may contribute to the permanent blue-shift of the resonances [81].

Remarkably, the process results in an average overall shift of 53 μeV while the FSR discrepancy compensated here amounts to only 6 μeV . Finally, the regularity of the trends shown in figs. 3.13a,b points to the high accuracy achievable with this tuning process, which can be further adjusted by a careful choice of the exposure time.

3.6 Four wave mixing

The combination of the PhC cavity design described above and the post-fabrication tuning technique enables in principle the implementation of triply resonant nonlinear processes in the bichromatic PhC cavity device. This configuration satisfies the *energy matching* condition for FWM. In order to quantify the overall efficiency of the process, the *phase matching* condition should also be investigated over the relevant volume where the nonlinear

3.6. Four wave mixing

process occurs. For the case of a resonator, such as a PhC cavity, the phase matching condition can be expressed as the requirement of a significant mode overlap in the real space [25, 82].

A quantitative treatment of the stimulated FWM process dynamics can be formulated in terms of coupled mode theory (CMT) [83, 82, 84]. Considering three resonant modes satisfying the energy matching condition $\omega_s + \omega_i = 2\omega_p$, the CMT equations for pump, signal and idler read:

$$\frac{da_s}{dt} = \left(i\omega_s - \frac{\Gamma_s}{2} \right) a_s - i\omega_s \beta_{fwm,s} a_p^2 a_i^* + \sqrt{\eta_s \Gamma_s} s_s \quad (3.3a)$$

$$\frac{da_i}{dt} = \left(i\omega_i - \frac{\Gamma_i}{2} \right) a_i - i\omega_i \beta_{fwm,i} a_p^2 a_s^* \quad (3.3b)$$

$$\frac{da_p}{dt} = \left(i\omega_p - \frac{\Gamma_p}{2} \right) a_p - 2i\omega_p \beta_{fwm,p} a_p^* a_s a_i + \sqrt{\eta_p \Gamma_p} s_p \quad (3.3c)$$

where $a_k(t)$ are the modal field amplitudes, defined such that $|a_k|^2$ is the energy of the resonant mode, Γ_k is the total decay rate of the mode involved, which in absence of nonlinear absorption is given by $\Gamma_k = \omega_k/Q_k$. Similarly, the forcing terms s_k model the incoming waves and are related to the incident power via the expression $P_{inc,k} = |s_k|^2$, while η_k is a coupling efficiency factor. The efficiency of the FWM process with respect to the intracavity energy can be quantified by the coupling term $\beta_{fwm,k}$, which depend on an overlap integral of the interacting fields and on the third-order susceptibility tensor:

$$\beta_{fwm,s} = \frac{\frac{3}{16}\epsilon_0 \int d^3\mathbf{r} \left(\mathbf{E}_s^* \cdot \overline{\overline{\chi}}^{(3)} : \mathbf{E}_p^2 \mathbf{E}_i^* \right)}{\sqrt{\int d^3\mathbf{r} \left(\frac{1}{2}\epsilon |\mathbf{E}_s|^2 \right) \int d^3\mathbf{r} \left(\frac{1}{2}\epsilon |\mathbf{E}_i|^2 \right) \int d^3\mathbf{r} \left(\frac{1}{2}\epsilon |\mathbf{E}_p|^2 \right)}} = \frac{3\chi_{1111}^{(3)}}{4n^4\epsilon_0 V_{fwm}} \quad (3.4)$$

where V_{fwm} is an effective ‘‘nonlinear’’ mode volume for the process, which is defined as:

$$V_{fwm} = \frac{\chi_{1111}^{(3)} \sqrt{\int d^3\mathbf{r} (\varepsilon |\mathbf{E}_s|^2) \int d^3\mathbf{r} (\varepsilon |\mathbf{E}_i|^2) \int d^3\mathbf{r} (\varepsilon |\mathbf{E}_p|^2)}}{n^4 \varepsilon_0^2 \int d^3\mathbf{r} (\mathbf{E}_s^* \cdot \overline{\overline{\chi}}^{(3)} : \mathbf{E}_p^2 \mathbf{E}_i^*)} \quad (3.5)$$

This quantity represents the equivalent volume of bulk nonlinear medium in which a uniform field with the same energy would yield the same nonlinearity β_{fwm} . In the case of crystalline silicon, the full permutation symmetry of $\overline{\overline{\chi}}^{(3)}$ implies:

$$\beta_{fwm,s} = \beta_{fwm,i} = \beta_{fwm,p}^* =: \beta_{fwm} \quad (3.6)$$

By solving equations (3.3) in steady state regime, under low pump depletion approximation, we find the intracavity energies:

$$|a_{s,p}|^2 \approx \frac{4\eta_{s,p}}{\Gamma_{s,p}} |s_{s,p}|^2 \propto \eta_{s,p} Q_{s,p} \quad (3.7a)$$

$$|a_i|^2 = \frac{4\omega_i^2 |\beta_{fwm}|^2}{\Gamma_i} |a_s|^2 |a_p|^4 \propto Q_i \quad (3.7b)$$

from which it is possible to calculate the total generated idler power:

$$P_{gen,i} = \Gamma_i |a_i|^2 = \frac{64\eta_p^2 \eta_s \omega_i^2 |\beta_{fwm}|^2}{\Gamma_p^2 \Gamma_s \Gamma_i} P_{inc,p}^2 P_{inc,s} \quad (3.8)$$

We observe that the overall idler generation rate is proportional to $|\beta_{fwm}|^2$ and thus $P_{gen,i} \propto 1/V_{fwm}^2$. Expressing the decay rates as a function of the modes' Q factors, the scaling trend for the overall generation efficiency results:

$$\rho_{fwm} = \frac{P_{gen,i}}{P_{inc,p}^2 P_{inc,s}} \propto \frac{Q_p^2 Q_s Q_i}{V_{fwm}^2} \quad (3.9)$$

This can be interpreted as a consequence both of the cavity field enhancement affecting the pump and signal modes (which is $\propto \sqrt{Q_k}$) and of the increased density of states for the idler mode. The result is consistent with the analogous theory for microring resonators [85], where the scaling trend is

3.6. Four wave mixing

Structure	β_{fwm} [$\text{J}^{-1} \times 10^6$]	V_{fwm} [μm^3]
Bichromatic (modes 1,2,3)	19	3.1
Bichromatic (modes 2,3,4)	24	2.5
Microring [82]	29	2.1

Table 3.1: Figures of merit comparison for FWM processes in different types of microresonators.

$\rho_{fwm} \propto Q^4/R^2$. Finally, following the argument proposed in ref. [85], one can estimate the scaling trend for the related spontaneous process by substituting $|a_s|^2$ with the characteristic energy $\hbar\omega_s$. Although a rigorous derivation is beyond the purpose of this work, the argument provides the correct scaling trend:

$$\rho_{fwm}^{sp} = \frac{P_{gen,i}}{P_{inc,p}^2} \propto \frac{Q_p^2 Q_i}{V_{fwm}^2} \quad (3.10)$$

For silicon bichromatic cavities discussed here, we assumed a nonlinear susceptibility $\chi_{1111}^{(3)} = 1.7 \times 10^{-19} \text{ m}^2/\text{V}^2$ [36] and we evaluated V_{fwm} from the field profiles calculated by FDTD. The estimated values of the nonlinear coupling coefficient and mode volumes are reported in table 3.1, where we made the hypothesis of involving either modes 1,2,3 or 2,3,4 as idler, signal and pump respectively. The calculated values are comparable to a microring design in silicon aimed to implement self-sustained oscillations (OPO), which requires a bending radius $R = 3 \mu\text{m}$ and a quality factor $Q = 10^6$. These values are currently not achievable via microring technology, since bending losses limit dramatically the maximum Q factor. In contrast, the bichromatic design shows values comparable in an experimentally demonstrated device with comparable $Q \approx 10^6$. At ideal coupling condition ($\eta_p = 1$) these values would provide a spontaneous generation efficiency of the order of $\rho_{fwm}^{sp} \sim 10^8 \text{ Hz}/\mu\text{W}^2$, which is by far larger than the highest value experimentally demonstrated so far in a PhC molecule [86] $\rho_{fwm}^{sp} = 300 \text{ Hz}/\mu\text{W}^2$.

A full benchmark comparison with the experimental samples presented here was unfortunately not possible, owing to the large variance in coupling efficiency associated with the excitation from far-field. A different approach, including one (*all pass* configuration) or two (*add-drop* configuration) evanes-

cently coupled W1 waveguides, would allow to increase the coupling efficiency and the experimental control over this value. Experiments in this configuration are currently still ongoing.

3.7 Conclusions

In this chapter we presented the design and demonstration of a PhC cavity based on a bichromatic lattice exhibiting comb-like spectrum and Q factors above 1 million. The essential limitations to employing these devices emerge from the accuracy of the fabrication process, which limits the maximum value of Q achievable and the repeatability in the alignment of the resonant modes. As supported by recent experimental studies [42], we believe that the former issue is intimately connected with the standard fabrication process for silicon PhC devices, and in particular with the parasitic absorption provided by defect states at the interfaces. Conversely, we showed how the latter issue, which emerges as a consequence of the absence of a natural condition for the equal spacing of the resonances, can be overcome by post-fabrication tuning of the fabricated devices performed via local oxidation. Furthermore, we evaluated theoretically and numerically the possibility of using this kind of microresonator for the implementation of highly efficient nonlinear processes, and we showed that, despite a non-perfect spatial overlap between different resonant modes, the figures of merit are much higher than any silicon-based microresonator demonstrated so far characterized by comb-like resonant spectrum.

In the perspective of nonlinear applications such as fully resonant frequency conversion, OPO and spontaneous or stimulated FWM, our devices are extremely promising thanks to the silicon photonics compatible platform, to the large Q/V figure of merit, which yields record-high values of finesse, and to the large nonlinear response of silicon, all key-features for the implementation of low power nonlinear photonic devices.

Nonlinear optics in silicon-rich silicon nitride PhC cavities

4.1 Motivation

The success of *silicon photonics* is strictly linked with the widespread of electronic industry, and in particular of the CMOS platform, which contributed to provide a mature technological background for the design, fabrication and testing of photonic devices [57]. In this perspective, the SOI in particular is the starting point for the fabrication of any integrated optical device, which may include linear and nonlinear optical components, such as multiplexers, filters, modulators, detectors and even light sources, which can be obtained by hybrid integration. A particular attention is also given to the possibility to complement photonic devices with electronic ones, in order to expand the range of applications of current technology by accessing the optical domain. For this reason, the realization of novel optical devices and the improvement of existing ones is often focused on the target of “CMOS compatibility”, which sets several technological constraints (e.g. an upper bound on processing temperatures, or the use of specific materials) on the fabrication processes.

For what concerns nonlinear applications, the SOI platform also provides several advantages, such as a high refractive index contrast ($n_{Si} = 3.47$,

$n_{SiO_2} = 1.44$ at $\lambda = 1550$ nm), which enables a tight light confinement: in particular, this property has been crucial for the realization of high-Q PhC cavities. Another advantage consists in the pronounced third-order nonlinear response, with a Kerr index $n_2 = 4.4 \times 10^{-18}$ m²/W. On the other hand, silicon presents several issues for nonlinear operation at telecom wavelength. In particular, TPA and related processes (FCA, FCD and TO effect) often become detrimental at high power by introducing additional absorption or dispersive effects, making the use of devices unpredictable or inefficient. Additionally, the thermo-optic coefficient of silicon is fairly large ($\alpha_{Si} = \frac{\partial n_{Si}}{\partial T} = 1.8 \times 10^{-4}$ K⁻¹ [43]) at room temperature, making frequency-sensitive nonlinear devices susceptible to conspicuous misalignment.

For these reasons, several alternative material platforms have been investigated in recent years, such as hydrogenated amorphous silicon [87], silicon oxynitride [88] and silicon nitride [89, 90], characterized by a wider transparency window in the visible and near-infrared range, which rules out the issue of TPA.

Among these materials, silicon nitride (Si₃N₄) has gained significant attention because of its optical properties. With a transparency window extending from $\lambda = 400$ nm to the mid-infrared and a TO coefficient as low as $\alpha_{Si_3N_4} = 2.4 \times 10^{-5}$ K⁻¹ [91], it exhibits negligible TPA and a wide range of tunability of its optical properties accessible during fabrication.

In this chapter, we present the experimental study of PhC cavities realized in suspended membranes of non-stoichiometric silicon nitride. In our samples, the concentration of silicon was purposely increased during fabrication in order to increase the refractive index of the resulting material, which we will refer to as *silicon-rich silicon nitride* (SRSN) [92], from $n_{Si_3N_4} \approx 2$ to $n_{SRSN} \approx 2.5$, thus enabling a more efficient confinement, and to improve its nonlinear response. The fabrication procedure was operated at low temperature ($T < 350$ °C) by plasma-enhanced chemical vapor deposition (PECVD), in order to be compatible with CMOS standards, while keeping low the inclusion of hydrogen, source of linear losses, which is usually associated to this technique. We show that the material quality is high enough to realize high- Q cavities which exhibit negligible TPA and we present the results of

cavity-enhanced second- and third- harmonic generation in resonant pumping conditions.

The results presented here are based on the work published in refs. [93], [94] and [92].

4.2 The SRSN material platform

Silicon nitride depositions employed in photonics are generally considered non-stoichiometric, as their element composition tends to depart from the stoichiometric nitrogen to silicon ratio (N/Si) of 1.3, and they are often classified into N-rich (N/Si > 1.3) and Si-rich (N/Si < 1.3). Moreover, SiN layers are usually rich in hydrogen, that incorporates into their structure to chemically stabilize their non-stoichiometric configuration. As such, SiN films are characterized by the presence of Si-H and N-H bonds, whose concentration is determined by their N/Si material composition [95]. Several properties of SiN, such as optical absorption, depend on its hydrogenation and they degrade if the hydrogen bond concentration is considerable (27% to 30%). Additionally, N-H bonds are especially problematic for the near-infrared, as they generate an absorption peak close to 1550 nm. Similarly, Si-Si bonds are important defects responsible for the formation of undesired grains, pores and columns that can cause additional scattering and absorption losses.

The optical transparency window of silicon nitride is wider than that of silicon, with a gap energy which can be varied by increasing the N/Si ratio of the material. This ranges from 2.7 eV for Si-rich films up to 5.0 eV for the N-rich medium. Similarly to that of silicon, the transparency window of SiN extends at low frequencies to the mid-infrared. Also the refractive index of SiN layer depends strictly on the material relative concentration, ranging from 1.7 for N-rich films up to values close to 3.0 for Si-rich ones, as shown in fig. 4.2, according with the relation:

$$\frac{N}{Si} = \frac{4}{3} \frac{n_{Si} - n}{n - 2n_{Si_3N_4} + n_{Si}} \quad (4.1)$$

The thin films of SiN are growth by chemical vapor deposition (CVD)

4. Nonlinear optics in silicon-rich silicon nitride PhC cavities

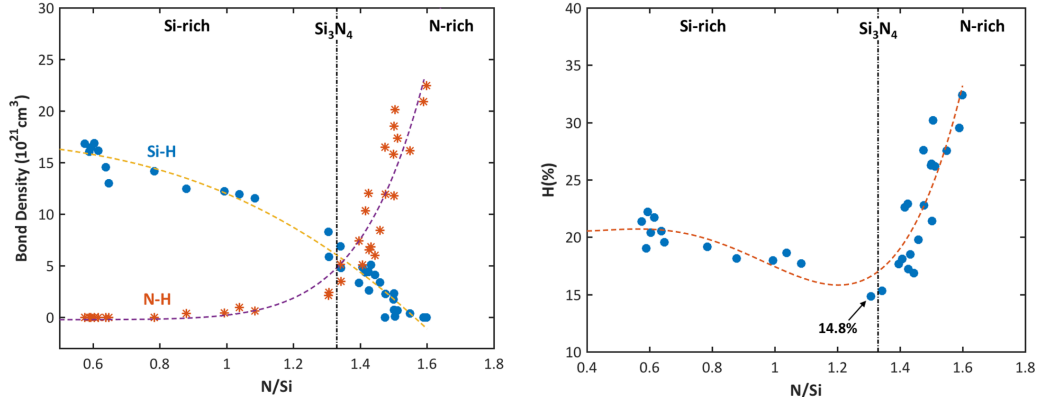


Figure 4.1: (Left) Si-H and N-H bond concentrations, as estimated by Fourier-transform infrared spectroscopy, for different N/Si ratios. The vertical line indicates the stoichiometric ratio of 1.33. Si-H bonds are dominant in Si-rich layers ($N/Si < 1.33$) and N-H bonds in N-rich layers ($N/Si > 1.33$). Both Si-H and N-H bond concentrations are almost the same near stoichiometry. The dashed lines are a guide to the eyes. (Right) Hydrogen concentration as a function of the N/Si ratio. A minimum of 15% is found for nearly stoichiometric films [96].

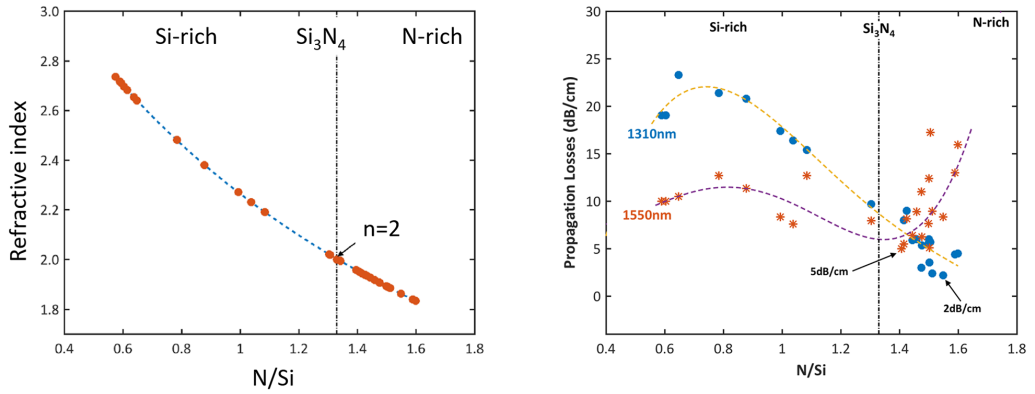


Figure 4.2: Refractive index at $\lambda = 1550$ nm (left) and propagation losses (right) of a PECVD silicon nitride thin film as a function of the N/Si ratio. The relation between stoichiometric ratio and refractive index is given by eq. (4.1). Dashed lines are guides to the eye [96].

4.3. High-Q photonic crystal cavities

techniques. The most popular technique for stoichiometric material is low-pressure chemical vapor deposition (LPCVD), which minimizes the hydrogen content. However, the high temperatures reached in the process ($T > 1000$ °C) set a limitation to CMOS compatible integration. For this reason, the growth of low-loss SiN by other techniques, such as PECVD, has been investigated. The severe incorporation of hydrogen which is typically associated to this low-temperature growth is mainly attributed to the supply of silane (SiH_4) and ammonia (NH_3) as precursor gases. It was recently shown [89] that a modified deposition process based on the use of nitrogen (N_2) as precursor instead of ammonia can dramatically reduce the concentration of hydrogen (fig. 4.1). This technique enabled to demonstrate waveguide propagation losses < 2 dB/cm comparable to the value of stoichiometric LPCVD silicon nitride [96]. The propagation losses and the refractive index of the material as a function of the stoichiometric ratio are shown in fig. 4.2.

More specifically, the linear and nonlinear properties of Si-rich silicon nitride (SRSN) waveguides were studied in detail in ref. [97]. Here the authors demonstrate, for a deposition characterized by $n \approx 2.5$, propagation losses as low as 1.5 dB/cm and they estimate a Kerr index of $n_2^{\text{SRSN}} = 1.6 \times 10^{-18}$ m²/W via FWM frequency conversion, which is almost one order of magnitude higher than the value reported for stoichiometric SiN ($n_2^{\text{Si}_3\text{N}_4} = 2.3 \times 10^{-19}$ m²/W). Most remarkably, the authors claim the absence of TPA even at input peak powers of the order of ~ 10 mW (fig. 4.3).

4.3 High-Q photonic crystal cavities

The advantages enumerated so far suggest the suitability of the SRSN as material platform for the fabrication of nonlinear optical microresonators. We thus designed and fabricated SRSN samples patterned with PhC cavities: our primary purpose was to show the suitability of this material platform for the efficient light confinement. Secondly, we aimed to show the nonlinear operation of these devices, taking advantage of the absence of TPA and of a presumably important nonlinear response. The quality of the material and in particular the low absorption coefficient are essential for achieving a high

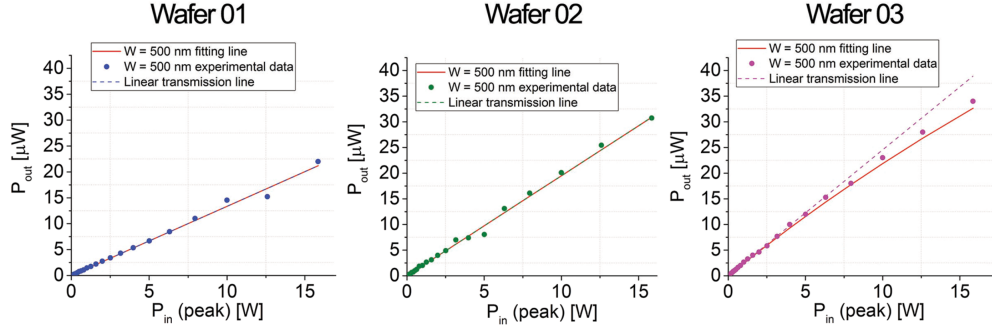


Figure 4.3: Time-averaged transmitted power in SRSN waveguides with cross-sectional dimensions $w \times h = 500 \times 220$ nm, under pulsed excitation. The three test wafers correspond to different deposition conditions, corresponding to increasing Si/N ratio. Wafer 02 exhibits a nonlinear response comparable to silicon ($n_2 = 1.6 \times 10^{-18}$) and negligible TPA. Wafer 03 exhibits the same Kerr index of silicon, associated to a eight-fold lower TPA absorption coefficient ($\beta_{TPA} = 0.1$ cm/GW) [97].

Q factor, while the low refractive index contrast sets a challenge in keeping low the out-of-plane losses.

For the high- Q demonstration, we adopted a line-width modulated cavity design, originally proposed by Kuramochi *et al.* [98], also known as *A1 cavity*. We chose a triangular lattice of air holes etched in a 300 nm thick SRSN slab. The target refractive index was about $n = 2.5$, consistently with previous investigations [97, 92]. A schematic of the cavity layout is shown in fig. 4.5a. The lattice constant was chosen $a = 570$ nm and $r = 0.3a$ in order to match the 0.17 eV wide PBG with the target telecom wavelength range, as calculated by GME (fig. 4.4a). The cavity was defined by a W1 line defect in the $\Gamma - K$ direction. With this cavity geometry, the confinement is provided by locally increasing the width of the W1 by laterally shifting the position of selected holes, outwards from the center of the waveguide. With reference to fig. 4.5a, the holes marked in red, yellow and purple were shifted in the y -direction of an amount $\Delta A = \Delta y$, $\Delta B = 2\Delta y/3$ and $\Delta C = \Delta y/3$ respectively, where Δy is a lithographic tuning parameter. This geometry yields a very effective strategy for gentle confinement, which produce in silicon Q factors well above ten millions [98]. The confinement principle is based on the local increase of the effective index (i.e. confinement potential) of the

4.3. High-Q photonic crystal cavities

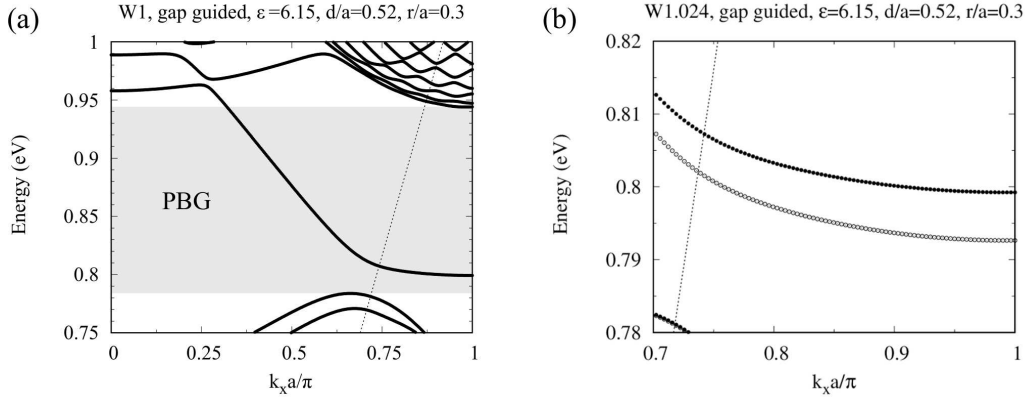


Figure 4.4: Guided mode expansion (GME) calculation of the photonic bands for a W1 waveguide (left). The calculation is performed with a rectangular supercell. The band corresponding to the gap-guided mode lays completely inside the PBG region under the light-cone (dashed line). In the right-hand panel, the same guided mode (black dots) is compared with the guided mode of a similar structure with increased width of $w' = w + 24$ nm (white dots), corresponding to the central region of the cavity. This mode cannot propagate outside the defect region due to the presence of the PBG. The spacing at the band-edge between the guided modes results to be of approximately 7 meV.

guided modes of the W1. If the transition is gradual such as in this case, the localized modes which emerge from the guided ones exhibit a distribution in the k -space which is close to the band edge, with few components falling into the light cone. To give a conceptual idea of the confinement mechanism, fig. 4.4b shows a GME calculation of the guided modes of a W1 waveguide compared with the same results for a width increased by $2\Delta y = 24$ nm. The gap-guided modes spacing at the band edge amounts to approximately ~ 7 meV.

The Q factor was estimated by FDTD simulations, with a mesh size of the order of $a/50$ and a hole shift sweeping from $\Delta y = 3$ nm to $\Delta y = 21$ nm. The highest value of Q was found to be $Q = 5.2 \times 10^5$ for a shift $\Delta y = 12$ nm, with an associated modal volume $V = 0.77(\lambda/n)^3$ at the resonance wavelength $\lambda = 1569$ nm. The $|E_y|$ component of the simulated near-field profile is shown in fig. 4.5b.

The fabrication of the samples was performed starting from a 6-inch sil-

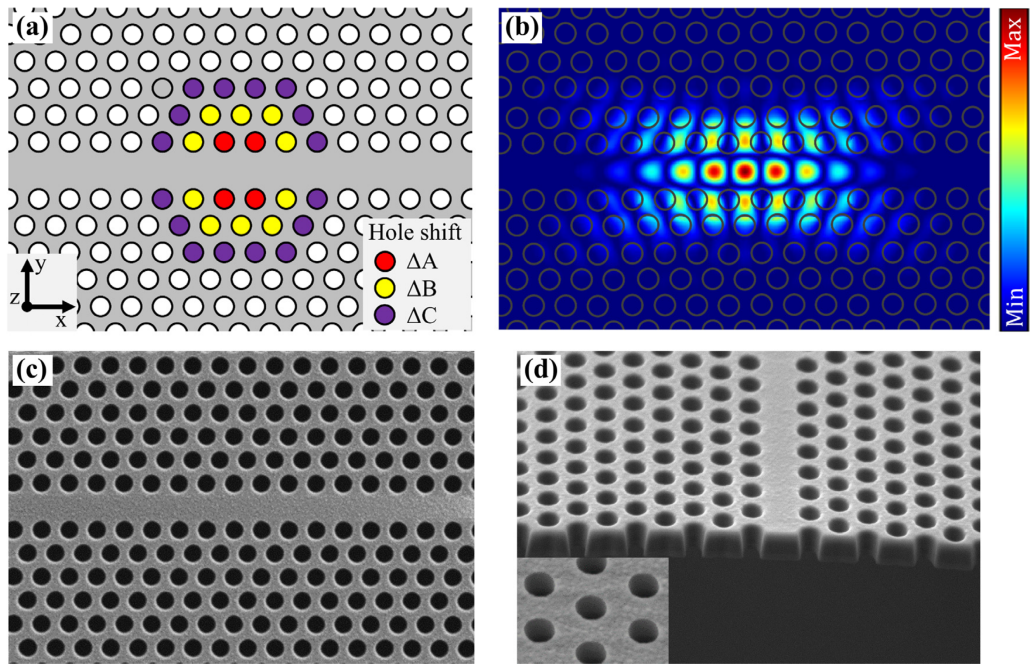


Figure 4.5: (a) Layout of the A1 PhC cavity. The holes marked by colors are shifted outwards along the y -axis in order to create a local increase of the waveguide width, yielding localized modes (b) Simulated (FDTD) $|E_y|$ component profile for the cavity with $\Delta y = 12$ nm. (c) SEM image of the fabricated PhC cavity. The hole shifts are too small to be distinguished visually. (d) SEM image showing the cross-section of the suspended PhC structure. The inset shows a zoomed in view of the structure. Surface roughness due to the deposition process is appreciable at this scale [93].

4.3. High-Q photonic crystal cavities

icon wafer with (100) surface orientation. A 300 nm thick SRSN layer was deposited by PECVD with a SH_4 flow of 3.6 sccm and a N_2 flow of 650 sccm at a sample temperature of 350 °C. The chamber pressure was set to 980 mTorr and the RF power to 60 W. A comprehensive discussion of the deposition process and its optimization can be found in refs. [96, 97, 99]. Ellipsometric characterization of the deposited film provided a refractive index value of $n = 2.48$ at 1550 nm wavelength. The wafer was spin-coated with a 450 nm thick layer of positive e-beam resist ZEP520A and exposed by EBL. After development with ZED-N50, the pattern was transferred to the SRSN layer via ICP-RIE, using a SF_6/CHF_3 gas chemistry. Once removed the remaining resist, the wafer was immersed in a 25% aqueous solution of Tetra-methylammonium hydroxide (TMAH). The action of TMAH selectively etches the silicon substrate underneath the patterned regions and leaves the PhC structures suspended in air. A SEM image of a fabricated sample is shown in fig. 4.5c. Figure 4.5d shows the cross-sectional view of the suspended PhC structure. A zoomed in view of the PhC region, shown in the inset, reveals some surface roughness, probably associated to the deposition process and characterized by a rms error of approximately $\sigma = 4$ nm, according to AFM measurements. SEM imaging also reveals a deviation from perfect verticality of the holes' sidewalls, which we believe is associated to the RIE process.

RS spectroscopy

The cavities were characterized at room temperature using the RS technique, in order to evaluate the intrinsic Q factor by coupling to the natural far-field emission of the resonators. A CW tunable laser source (Santec TSL-510) was scanned across the resonance range and the scattered light was collected in the crossed polarization and detected by a photodiode (Newport 918D InGaAs power-meter head). Typical experimental spectra are shown in fig. 4.6. From Fano fit of the experimental data, we estimated Q factors ranging from 71,000 to 122,000 for different values of the shift Δy (fig. 4.7) and we observed a linear scaling trend in the resonance wavelength as a function of this parameter. The highest quality factor measured $Q =$

1.22×10^5 corresponded to $\Delta y = +6$ nm. The discrepancy of this value with the numerical prediction should be attributed to the extrinsic losses associated to the fabricated devices. In particular, the residual material absorption (~ 1.5 dB/cm) is likely to constitute the most important loss channel, limiting the ultimate value of Q achievable. An estimate of the Q factor associated to extrinsic losses can be computed by the formula:

$$Q_{ext} = \frac{2\pi n}{\lambda \alpha_0} \approx 1.45 \times 10^5 \quad (4.2)$$

where n is the refractive index and α_0 is the linear absorption coefficient of the material. The formula is valid for a Fabry-Pérot resonator with a length $L \approx \lambda$, and it provides an upper bound estimate on the maximum experimental Q achievable. This upper bound is represented in fig. 4.7a as an horizontal dashed line. Figure 4.7b shows a good agreement between the simulated and measured values of the resonant wavelength, pointing to a systematically smaller value of the effective index in the fabricated device compared to the nominal parameters, which translates in a slight blueshift of the resonances.

Finally, we characterized the cavities at different input powers. By sweeping the excitation from blue to red wavelengths, we were able to observe a crossover from the linear Fano response at low power to a bistable regime, as shown in fig. 4.9. The red-shift of the resonance wavelength, which can be identified at bistable regime with the peak of the sawtooth-shaped RS curve, is originated by the TO effect, which induces a local increase of the refractive index. The calculated values of coupled power were estimated as $P_{coupled} = \eta_c/2P_{incident}$, where $P_{incident}$ is the incident power on the sample from free space and η_c is the coupling efficiency in parallel cavity/polarizers configuration, which we measured $\eta_c = 6\%$ using the procedure detailed in section 2.2. The factor 2 at the denominator accounts for the polarization mismatch between the incident mode and the localized one. A maximum wavelength shift of $\delta\lambda \approx 1.2$ nm was observed for a maximum input power of $180 \mu\text{W}$, which corresponds, according with the measured thermo-optic co-

4.3. High- Q photonic crystal cavities

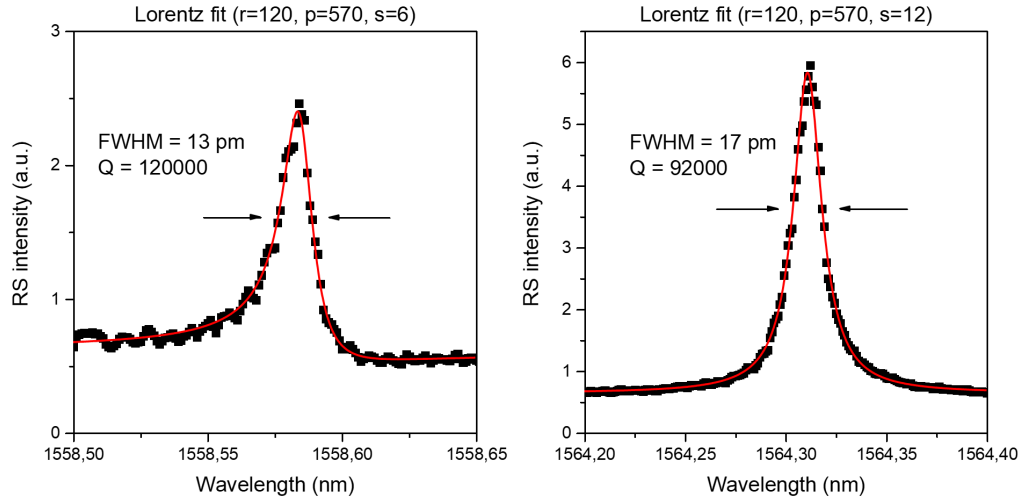


Figure 4.6: Typical RS spectra of high- Q PhC cavities with A1 design. The nominal parameters are $a = 570$ nm, $r = 120$ nm, $\Delta y = 6$ nm (left) and $\Delta y = 12$ nm (right).

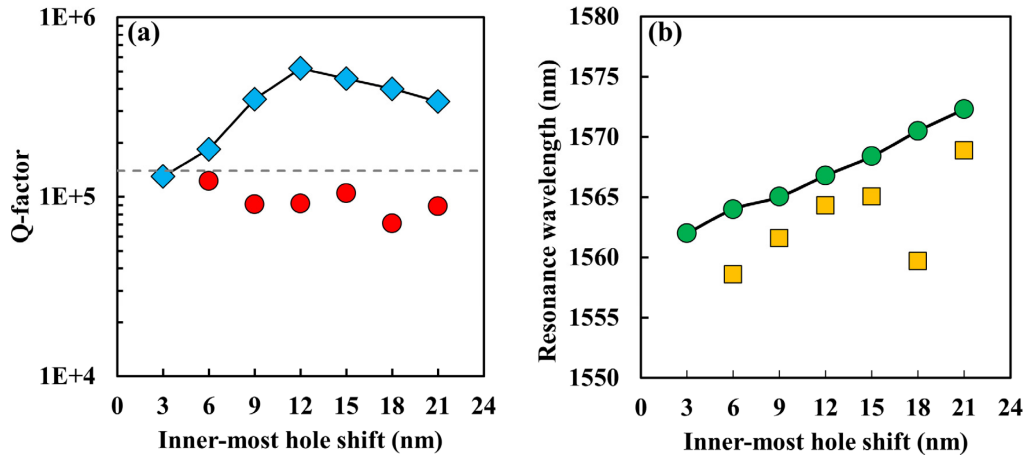


Figure 4.7: (a) Cavity Q -factors as a function of inner-most hole shift (Δy). Blue diamonds represents the numerically simulated Q values and red circles represent the RS measured Q values. (b) Cavity resonance wavelengths as a function of inner-most hole shift. Green circles represents the simulated resonance wavelengths and yellow squares represent the measured resonance wavelengths [93].

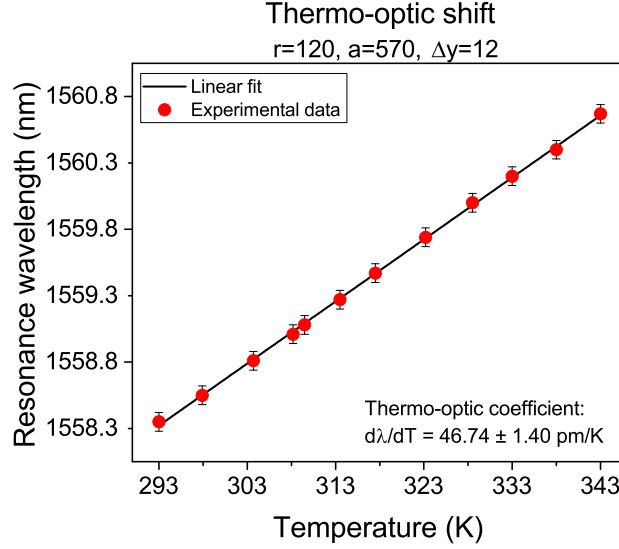


Figure 4.8: Measured shift of the resonance wavelength as a function of the sample temperature, for SRSN PhC cavity with A1 geometry. Note that the thermo-optic coefficient $\alpha = \frac{1}{\lambda_0} \frac{d\lambda_0}{dT} \approx \frac{1}{n} \frac{dn}{dT} = 3.0 \times 10^{-5}$ is lower than silicon and larger than the Si_3N_4 value.

efficient value (fig. 4.8), to a local effective temperature increase of $\Delta T \approx 25$ °C.

The physical mechanism which induces a temperature variation and thus TO effect can be various. The most significant contributions are usually linear (material) absorption, TPA and FCA. The former in particular is associated to the population of the conduction band as a consequence of the former effects. One way to identify the dominant absorption process is to relate the resonance shift to the coupled power. Since TPA and FCA are nonlinear phenomena, the increase in temperature associated is superlinear with respect to the coupled power, while linear absorption induces a shift which is proportional to the coupled power (see section 1.2). Following this argument, we can deduce from fig. 4.9b that the main mechanism involved is in our case the linear absorption from the SRSN layer, associated to the presence of Si-H, Si-Si and residual N-H bonds. Moreover, we suggest that the effect of FCA is strongly reduced thanks to the low carrier lifetime which is typical of amorphous materials.

4.3. High-Q photonic crystal cavities

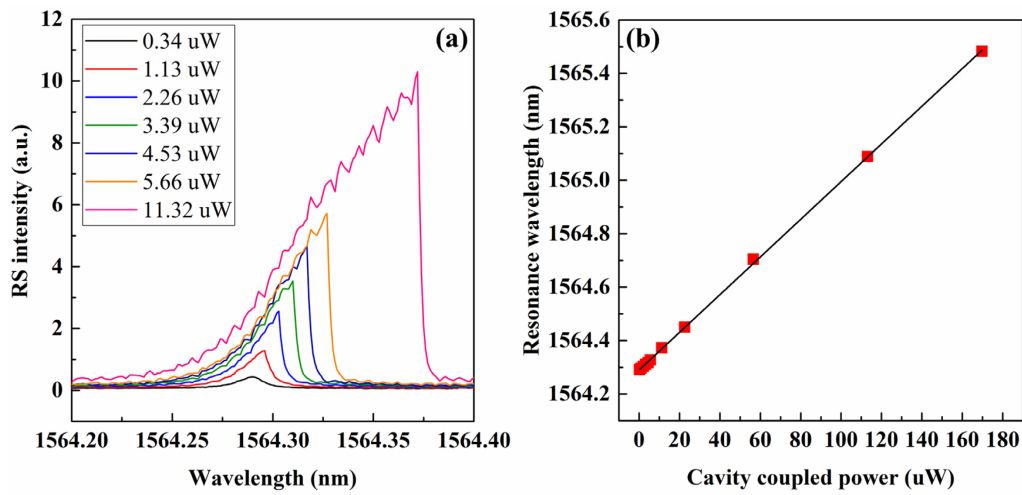


Figure 4.9: (a) Power-dependent RS response of SRSN PhC cavities. The redshift of the cavity resonance, associated to the bistable response of the cavity mode, is principally related to TO effect induced by the linear material absorption. Legend shows the estimated coupled power. (b) Peak resonance wavelength (red squares) as a function of the coupled power and linear fit of the trend (solid black line). Note the linearity of the trend, which suggests how even at high coupled power ($\sim 100 \mu\text{W}$, not shown in panel a), the wavelength shift is mainly due to linear absorption [93].

4.4 Cavity-enhanced harmonic generation

The results described in the previous section constitute a promising basis for the investigation of the performance of PhC-based nonlinear devices in SRSN. In this study, we focused in particular on the generation of second and third harmonic. As discussed in chapter 1, both processes take advantage of the field enhancement related to the resonance at fundamental wavelength, although the absence of a “destination” mode at the second or third harmonic wavelength does not provide any benefit in terms of density of states for the generated signal. However, the efficiency related to the incident pump power is still expected to be strongly improved by the resonant nature of the process.

The investigation of SHG has been particularly prolific in previous literature works, where several material platforms were object of analysis. Among the others, indium phosphide (InP) [100], gallium arsenide (GaAs) [101] and silicon [60] are characterized by a relatively narrow bandgap, which introduces absorption in the second harmonic (SH) signal for a pump at telecom wavelength. In the perspective of applications, other materials, characterized by a wider spectral window, were investigated, including gallium phosphide (GaP) [102], silicon carbide (SiC) [103] and gallium nitride (GaN) [61, 104]. In this framework, SRSN provides a CMOS compatible platform which at the same time, is characterized by transparency at SH wavelength. On the other hand, the amorphous structure of SRSN forbids a bulk $\chi^{(2)}$ nonlinearity, as the random dipole orientation results in an zero-averaged second order response. Nonetheless, the process can still occur thanks to the breaking of inversion symmetry introduced by the interfaces constituting the structured material, and it takes advantage of the large surface-to-volume ratio of the PhC structure. A previous example of SHG in PhC cavities made of a centrosymmetric material (silicon) can be found in ref. [60], while an analogous result referred to stoichiometric Si_3N_4 microrings can be found in ref. [105].

Less attention has been devoted on THG with PhC cavities, perhaps because of the frequent presence of absorption at third-harmonic wavelength. Still, the presence of a bulk $\chi^{(3)}$ and the possibility to exploit THG imaging for a mapping of the near-field of the localized mode provide good reasons for

4.4. Cavity-enhanced harmonic generation

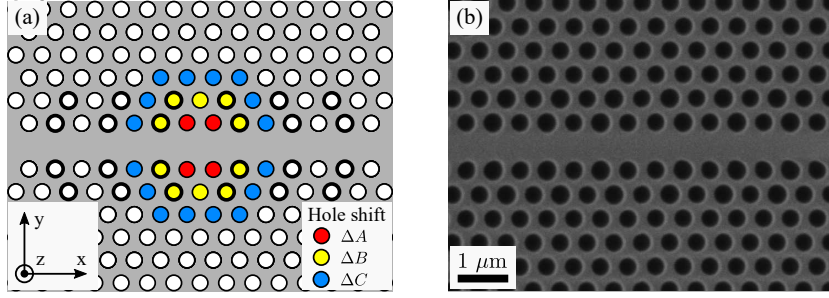


Figure 4.10: (a) Schematic of the PhC cavity design. The red, yellow and blue holes are shifted on the y -axis away from the line defect of an amount $\Delta A = 15$ nm, $\Delta B = 10$ nm and $\Delta C = 5$ nm respectively. As a main distinction with fig. 4.5, the holes marked by bold circles are characterized by a radius larger than the nearby holes of $\Delta r = +12$ nm, in view of far-field optimization. (b) SEM image of the fabricated sample. Nominal parameters are specified in the main text [94].

the investigation of the phenomenon. In this perspective, the high Kerr index of SRSN and the high refractive index contrast of the material, compared with Si_3N_4 , which provide the possibility of a tighter confinement, constitute a good starting point.

The samples employed for HG experiments were based on a similar design of that described above, and realized on a second chip with analogous fabrication process. As a main design difference, a far-field optimization was included by increasing the size of specific holes with doubled periodicity with respect to the original lattice (marked bold in fig. 4.10a). The normalized efficiency of the n -th order harmonic generation process is expected to scale proportionally to $(\eta_c Q/V)^n$, where $\eta_c = P_{\text{coupled}}/P_{\text{incident}}$ is the overall coupling efficiency for resonant excitation from free space. Thus, our design target was to maximize, for fixed V , the $\eta_c \times Q$ product, rather than the Q factor alone. The optimization resulted in a significant increase of the η_c related to the transverse mode of the impinging excitation laser, at the cost of a reduced Q factor. After a linear characterization of the devices, we selected a cavity with $a = 580$ nm, $r = 0.30a$ and $\Delta y = 15$ nm.

We validated our design via three-dimensional finite-difference time-domain (FDTD) simulations. Employing a mesh cell size of $0.02a_x \times 0.02a_y \times 30$ nm we calculated a Q factor as high as 21,000 for the fundamental mode centered

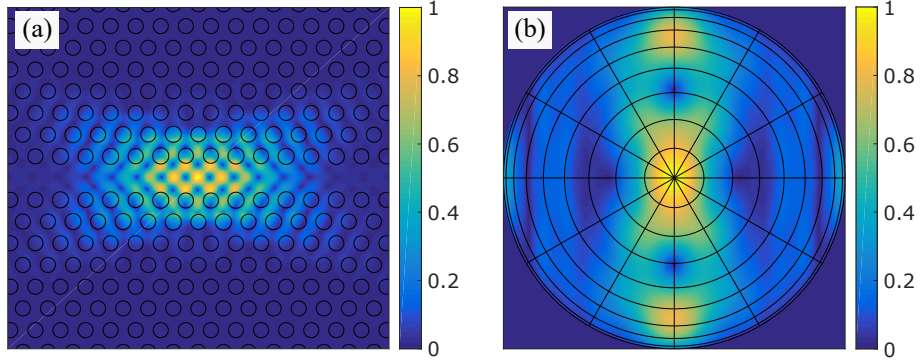


Figure 4.11: (a) Simulated near-field profile of the fundamental resonance mode (in-plane electric field amplitude $|E|$, normalized linear scale). (b) Far-field projection of the simulated fundamental resonant mode (electric field amplitude $|E|$). The main lobe at $\theta = 0^\circ$ was optimized to match a focused Gaussian beam profile impinging orthogonal to the cavity plane. Grid ranges from 0° to 90° [94].

at $\lambda_0 = 1577$ nm and a mode volume $V = 0.73(\lambda/n)^3$, very close to our previous result. The simulated near- and far-field profiles for the fundamental mode are shown in fig. 4.11a and 4.11b.

We fabricated the samples in a 300 nm thick suspended membrane of SRSN, following the same procedure described in the previous section. Fig. 4.10b shows a SEM image of one of the realized samples.

Experiment and Results

We performed a preliminary linear (low-power) RS characterization of the fabricated samples, in order to select the best suited. The experimental apparatus, modified to implement the HG measurement, is depicted in fig. 4.12a. We employed a tunable CW laser source (Santec TSL-510) for the excitation of the fundamental cavity mode.

By employing lithographic tuning of the fabrication parameters (fig. 4.12c and 4.12d), we were able to select the sample which maximizes the figure of merit $\eta_c \times Q$. We found the optimal value for a cavity with modification of the holes' radii $\Delta r = +12$ nm, for which we measured a resonance wavelength $\lambda_0 = 1546.3$ nm and a quality factor $Q = 13,000$, as retrieved from Fano fit of the measured RS spectrum [55], represented in fig. 4.12b.

From comparison of the measured Q factor with the one of non-optimized

4.4. Cavity-enhanced harmonic generation

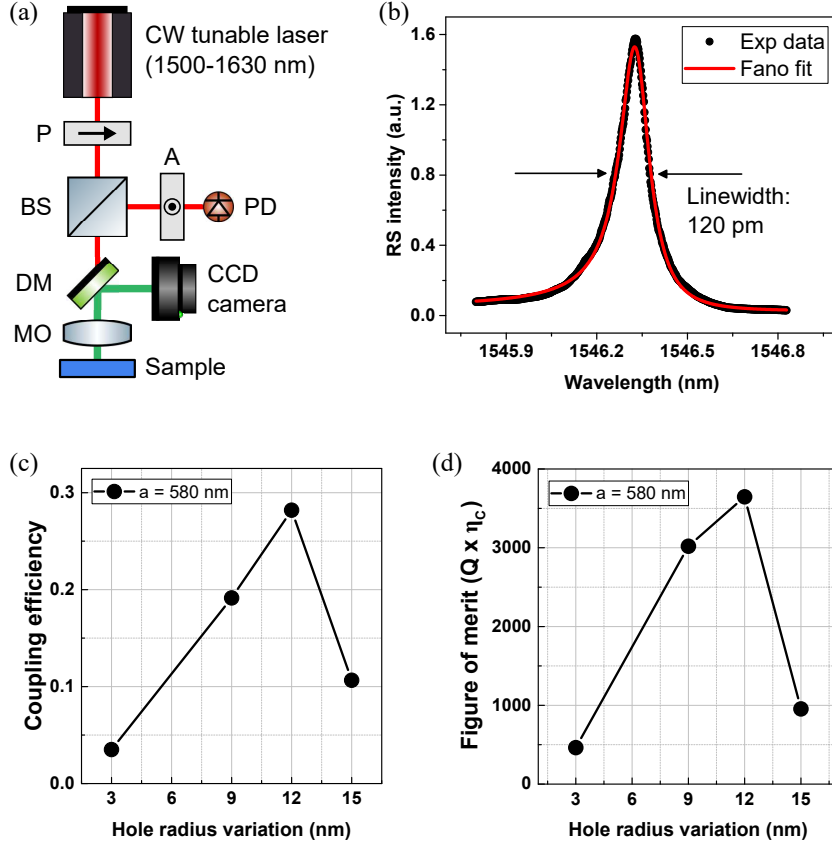


Figure 4.12: (a) Schematic of the experimental apparatus. The collimated light from a CW tunable source is polarized (P) and focused through a microscope objective (MO) on the sample, which is placed in the focal plane at 45° with respect to the laser polarization. The same excitation path is used to collect the RS signal and the generated SH and TH, which are separated from the pump via a dichroic mirror (DM) and imaged on a CCD camera. The RS signal is then filtered by a crossed polarizer (A) and collected by a InGaAs-based photodetector (PD). (b) RS spectrum and Fano fit for the fundamental (pump) resonant mode of the cavity. (c) Estimated coupling efficiency and (d) figure of merit ($\eta_c \times Q$) for selected samples as a function of the radius variation Δr introduced to optimize the coupling to far-field [94].

cavities [93], we estimate the far-field coupling to be the dominant decay channel for the localized mode.

In order to evaluate the coupling efficiency, we compared the peak RS signal at the resonance wavelength with the one measured by replacing the sample with a reference mirror and aligning the polarizers in parallel directions [60]. We were thus able to estimate a coupling efficiency from free-space to the cavity as high as $\eta_c \approx 30\%$. Besides the intrinsic factor 1/2 due to the symmetry of the system, we expect this value to be limited mainly by 1) the mode mismatch of the focused Gaussian beam with the far-field pattern and 2) the finite numerical aperture of the optical system. As a comparison, we used the calculated far-field pattern of the cavity (fig. 4.11b) to evaluate the fraction of power emitted within the field-of-view of the objective, thus estimating¹ a maximum theoretical coupling efficiency $\eta_c^{theory} \approx 92\%$ for the far-field optimized cavity ($\Delta r = +12$ nm) and $\eta_c^{theory} \approx 35\%$ for the non-optimized device. These values are very high, owing to the high numerical aperture (NA=0.8) of the objective used. The discrepancy between the experimental value and the theoretical one is probably due to the mismatch between the far-field pattern distribution and the impinging Gaussian mode, and secondly to any residual misalignment (position, focus, polarization) in the experimental setup, pointing to a possible considerable improvement in the coupling efficiency via far-field engineering.

We then probed the nonlinear response of the selected cavity mode. We employed the same apparatus to collect the generated SH and TH signal, and included a dichroic mirror (DM) and an appropriate sequence of filters to separate it from the pump at fundamental wavelength. We imaged the near-field of generated harmonics on a silicon-based CCD camera (PI Acton, liquid nitrogen cooled). By increasing the pump power, we were able to observe the generation of light at SH and TH wavelengths (fig. 4.13), which we later confirmed by spectroscopic measurements (fig. 4.14a-b).

Fig. 4.13a shows the generated SH emission from the sample. The large

¹The coupling efficiency was estimated as $\eta_c^{theory} = \frac{\int_0^{2\pi} \int_0^\theta |E(\theta, \phi)|^2 d\theta d\phi}{\int_0^{2\pi} \int_0^\pi |E(\theta, \phi)|^2 d\theta d\phi}$, where $E(\theta, \phi)$ is the far-field distribution calculated via FDTD and $\theta = \arcsin NA \approx 53^\circ$ is (half) the objective angular field of view.

4.4. Cavity-enhanced harmonic generation

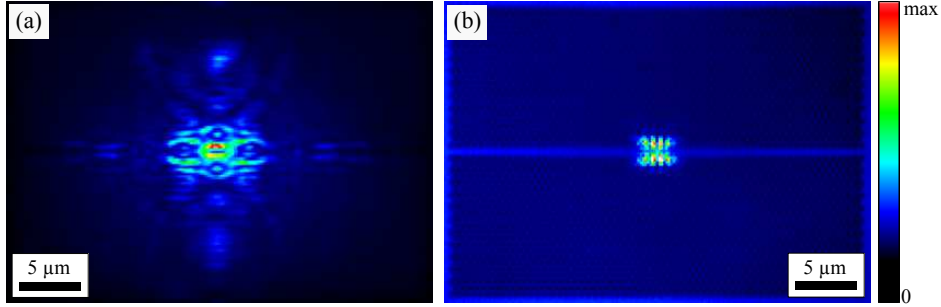


Figure 4.13: False color images of the generated (a) SH and (b) TH near-field profiles (linear scale). The sample background was artificially illuminated for sake of clarity [94].

modal area suggests transparency of the SRSN material at $\lambda_{SH} = 773.2$ nm. As the material consists in an amorphous deposition [96], we hypothesize that the intrinsic $\chi^{(2)}$ response of the medium is averaged to zero on the ensemble. The physical origin of the observed phenomenon relies then in the breaking of inversion symmetry mainly provided by the multiple interfaces between the bulk material and the air holes. Since the structure is not resonant at the SH wavelength, the signal here generated couples to the quasi-guided (leaky) modes of the PhC slab and eventually radiates outside the the membrane.

Fig. 4.13b shows the generated TH. Because of the bulk nature of the non-linear process, the TH near-field profile mimics the one of the fundamental mode, as one can notice by comparison with fig. 4.11a. A qualitative comparison between fig. 4.13a and fig. 4.13b suggests that the material absorption at $\lambda_{TH} = 515.4$ nm is significant. This datum was confirmed by ellipsometric measurements, which highlighted an absorption band edge wavelength of 600 nm. The underlying physical mechanism here is the following: the TH is originated from the bulk $\chi^{(3)}$ nonlinearity of the material, which is expected to be larger than the one of stoichiometric silicon nitride [97], but it is soon absorbed by the material itself. The small fraction of TH light which is not absorbed can be then observed in the experiment, and closely follows the near field profile of the fundamental (localized) mode.

Fig. 4.14b illustrates the spectral response of the system for large coupled power. The relatively large coupled power ($P_{coupled} \approx 1$ mW) induces heating

of the cavity region, originated by the linear absorption of the material [93] at resonance wavelength. Thus, the measured spectrum exhibits a markedly asymmetric, sawtooth-shaped response, which is a characteristic signature of the regime of optical bistability [47, 79, 101], in this case originated by thermo-optic effect due to residual linear absorption of the silicon-rich nitride material. The plotted SH and TH spectra are acquired simultaneously with the fundamental (pump) RS spectrum and clearly follow the squared and cubed trend of the latter respectively, confirming the cavity-enhanced nature of the nonlinear processes under investigation.

In order to confirm the validity of our observations, we characterized the power scaling trend of the nonlinear processes. The analysis is represented in fig. 4.14c. By varying the input power to our setup and tuning the wavelength of the excitation laser to compensate for the thermo-optic shift of the resonance [47, 93], we were able to scan the coupled power at the fundamental wavelength from $\sim 100 \mu\text{W}$ to 1.6 mW. We estimated the total collected power by integrating over the region-of-interest of our CCD detector. The plot shows with good confidence a quadratic and cubic scaling trend for the generated SH and TH respectively. From the best fit of our results we were able to estimate the normalized generation efficiencies $\rho_{SH} = P_{SH}/P_{coupled}^2 = (4.7 \pm 0.2) \times 10^{-7} \text{ W}^{-1}$ and $\rho_{TH} = P_{TH}/P_{coupled}^3 = (5.9 \pm 0.3) \times 10^{-5} \text{ W}^{-2}$. It should be remarked that these results represent extrinsic values, as they do not take in to account the fraction of generated power which is not collected by the optical system as it is absorbed, coupled to the guided modes of the membrane or scattered outside the numerical aperture of the system. However, these values provide a lower bound on the overall efficiency of the process for practical applications and we believe that they can be significantly improved by engineering the extraction mechanism of the generated signal from the cavity at the SH and TH frequencies.

To provide a term of comparison, generation efficiencies of the order of $\rho_{SH} \approx 10^{-5} \text{ W}^{-1}$ and $\rho_{TH} \approx 10 \text{ W}^{-2}$ were reported in silicon-based PhC cavities [60], while the relevant data for microring resonators based on stoichiometric silicon nitride [105] are $\rho_{SH} \approx 10^{-3} \text{ W}^{-1}$ and $\rho_{TH} \approx 10^{-9} \text{ W}^{-2}$. It should be remarked that the former platform exhibits a tighter confinement

4.4. Cavity-enhanced harmonic generation

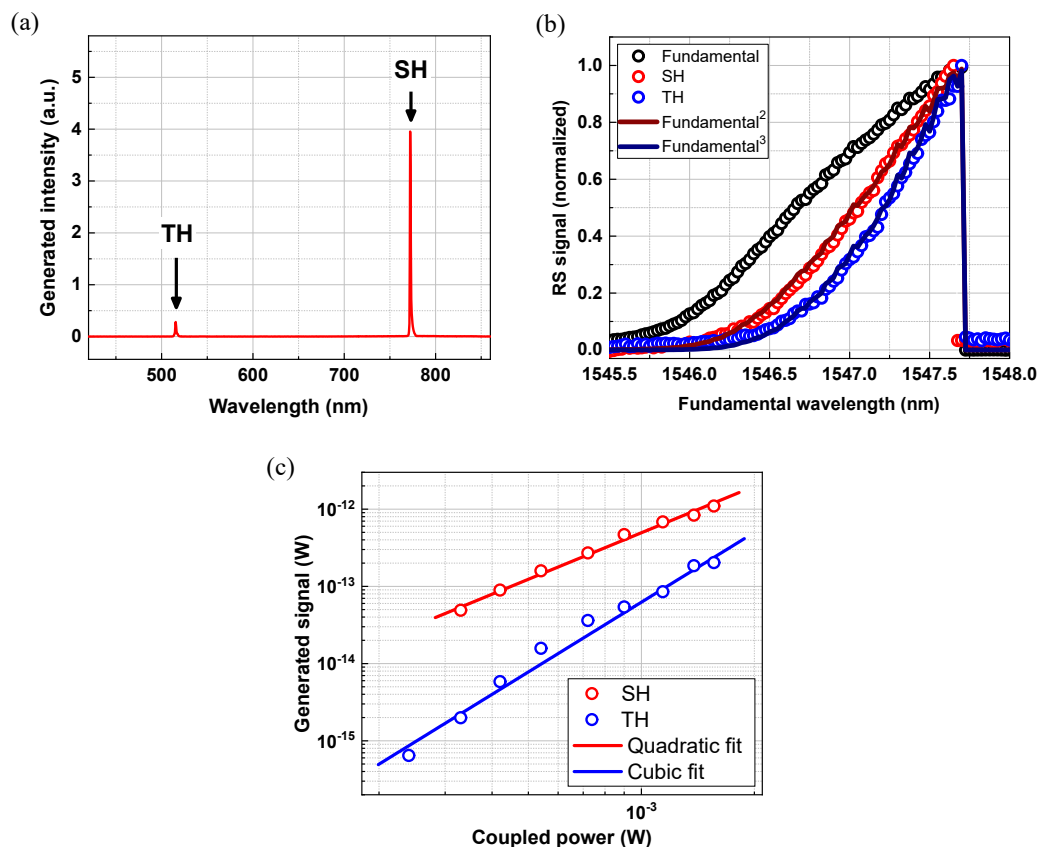


Figure 4.14: (a) Sample spectrum of the generated SH and TH. (b) High power spectrum of the cavity resonance and comparison with the generated SH and TH signals. The large coupled power ($P_{coupled} \approx 1$ mW) leads the system to operate at a regime of strong thermo-optic bistability [47, 79, 101], providing the characteristic sawtooth-shape to the spectrum at fundamental wavelength. The generated SH and TH signals closely follow the squared and cubed trend of the fundamental RS signal respectively, highlighting the cavity-enhanced, nonlinear nature of the phenomenon under investigation. (c) Scaling trends of the (peak) generated SH and TH signals. The pump wavelength was systematically adjusted in order to compensate for thermo-optic shift of the resonance. Experimental deviations from the expected trends are mainly related to 1) strong background for points at low power and 2) thermo-optic instability [47, 93] for points at high power [94].

than the one here presented, due to the higher refractive index contrast of the silicon/air interface, while the latter is characterized by a weaker confinement due to the lower refractive index and the significantly larger mode volume. It should be also noted that the SH generation efficiency reported here is significantly lower compared to materials exhibiting non-vanishing bulk second order nonlinearity [61, 102, 101, 106], with measured values of generation efficiency ranging from $\rho_{SH} \approx 2 \times 10^{-3} \text{ W}^{-1}$ to $\rho_{SH} \approx 4 \text{ W}^{-1}$. We remark that a quantitative comparison between harmonic generation efficiencies in different resonant photonic devices would require the knowledge of the second and third-order nonlinear polarization in the presence of highly anisotropic nanostructured surfaces, as in the case of photonic crystal nanocavities. This non trivial task is, however, beyond the scope of the present work.

Remarkably, the data presented here highlight the absence of saturation effects due to TPA [38], typical of silicon-based devices. A quantitative comparison may be obtained by looking at the power-dependent generation efficiency curves reported in ref. [60] for silicon PhC cavities having a figure of merit $\eta_c \times Q = 4,000$ and a Q factor and mode volume very similar to those presented in this work. Indeed, while silicon cavities display a clear saturation of the SHG and THG signals for coupled power of a few tens of μW , our SRSN cavities do not show any evidence of saturation even for coupled powers in the mW range. This result confirms the suitability of SRSN as a valid alternative to silicon for the fabrication of CMOS compatible integrated nonlinear optical devices.

4.5 Conclusions

In this chapter, we presented the numerical and experimental study of PhC cavities based on the SRSN material platform. We discussed the physical properties of the material deposition and their effect on the suitability of the material for applications to integrated photonics. We showed how the tuning of the refractive index achieved via fabrication enables to achieve a refractive index contrast dielectric/air sufficient to fabricate high- Q PhC cavities. We presented the linear and nonlinear spectroscopic characterization

4.5. Conclusions

of these devices, showing that quality factors as high as $Q = 120,000$ can be achieved, while the residual linear absorption from the material plays a significant role as a limitation. The nonlinear properties were investigated by studying the thermo-optically induced bistability, and pointed to the absence of TPA and TPA-related detrimental effects. Finally, we studied the generation of second- and third-harmonic under resonant pumping conditions, and we quantitatively estimated the normalized generation efficiencies $\rho_{SH} = P_{SH}/P_{coupled}^2 = (4.7 \pm 0.2) \times 10^{-7} \text{ W}^{-1}$ and $\rho_{TH} = P_{TH}/P_{coupled}^3 = (5.9 \pm 0.3) \times 10^{-5} \text{ W}^{-2}$. Remarkably, our investigation points to the absence of TPA effects for coupled power as high as few milliwatts, in cavities characterized by a quality factor as high as $Q = 21,000$.

Thermo-optically induced transparency

5.1 Motivation

The active control over light propagation in a medium is one of the main goals of optical engineering and photonics. Extensive studies of the factors affecting the *group velocity* of light $v_g = \frac{\partial\omega}{\partial k}$, which in most of practical cases coincides with the speed of energy (or information) transfer, have been performed in order to either gain a better understanding of the underlying physical processes or to investigate novel technological applications [107, 108, 109]. The applications of *slow light* (where $v_g \ll c$), in particular [110], include optical delay lines [111, 112], all-optical memories [113], enhanced nonlinear devices [114, 115, 116] and quantum memories [117, 118]. A fast and accurate control can even be used to achieve *stopped light*, as already shown in different experiments [119, 120].

Depending on the underlying physical mechanism which makes possible to dramatically reduce v_g , it is usually made a distinction between *structural slow light* and *material slow light* [121]. Although a stark distinction is not always possible, as a general rule the former effect refers to the interaction of light with structured media where a peculiar arrangement of the dispersion relation is achieved, without however an exchange of energy between the

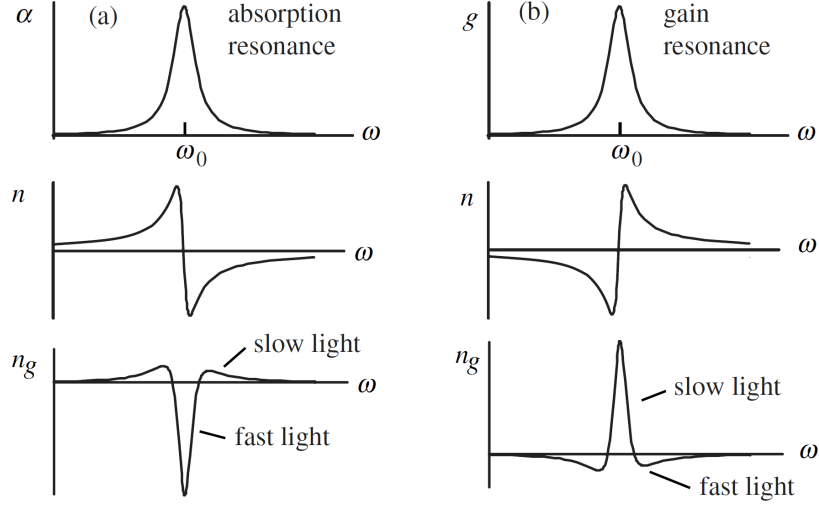


Figure 5.1: Dispersion and group index profile associated to an isolated absorption (a) and gain (b) resonance. A Lorentz type absorption resonance is associated to a steep anomalous dispersion profile. Owing to the relation $n_g = n + \omega_0 \frac{dn}{d\omega}$, this is related to fast light at the resonance frequency ω_0 . Similarly, a pronounced slow light peak is associated to gain resonances. This phenomenology is the basic concept behind material slow-light. Figure from [121].

medium and the electromagnetic field. A paramount example of this case are PhC waveguides, where the flatness of the photonic bands close to the band edge yields $v_g \rightarrow 0$ [110]. The underlying mechanism relies here in the reciprocal exchange of energy between forward- and backward-propagating modes, which makes experimentally possible to achieve a pulse propagation velocity of the order of $v_g \sim c/100$, without incurring in excessive losses.

In contrast, material slow light is based on the exchange of energy (coupling) between the propagating field and another physical system, such as an atomic cloud for instance [113]. The strong dispersion which is exploited to achieve low group velocities is typically associated to strong absorption (fig. 5.1), as it can be described by a simple Lorentz model and, more in general, as a consequence of Kramers-Krönig relations [122]. Being detrimental for applications, this issue can be overcome by taking advantage of the phenomenon known as *electromagnetically induced transparency* (EIT) [123, 124], where a strong control field is applied in order to induce a narrow transparency window in the material absorption spectrum. Moreover, the narrow-band

character of the EIT phenomenon is associated to a further reduction in the group index. It was shown experimentally how this and related techniques allow to produce a slow down of light of the order of $v_g = 17$ m/s by exploiting cold atoms clouds [113]. Stopped (or stored) light can also be achieved by dynamically operating the control beam [119]. Other notable examples of material slow light include coherent population oscillations (CPO) [125, 126], stimulated Brillouin scattering (SBS) induced transparency [127], where the interaction between photons and acoustic phonons is exploited, and optomechanically induced transparency (OMIT) [128, 129], where the physical system involved is a macroscopic or mesoscopic mechanical resonator.

In the perspective of applications, structural slow-light, SBS and CPO are particularly appealing as their effect can be observed even at room temperature. The latter process in particular is capable to provide a slow-down comparable to the one associated to EIT, but it is bound to work spectrally close to an atomic resonance, limiting its technological applicability. Moreover, from the device standpoint, often the concept of group velocity is substituted by the one of *group delay* (or *group advance*), which is more suitable for the description of lumped element systems such as optical resonators, and especially significant in view of applications to optical memories. Regardless the size of the optical system, this quantity determines the performance of an optical storage unit to retain information.

In this chapter, we describe an effect of induced transparency originated by the *thermo-optical interaction* in optical microcavities. We draw a parallel with the phenomenon of OMIT, which realizes a valuable case study. We present an original analytic model which effectively describes the process. We discuss the experimental technique developed to characterize the process and the results obtained. Finally, we investigate further perspectives and the possible technological impact of our results.

5.2 Overview

The phenomenon we describe hereby stems from the oscillation in time of a cavity resonance wavelength as a consequence of the thermo-optic (TO)

effect, which is observed in the presence of a time-varying field intensity. This results in a very narrow (~ 1 MHz) absorption or gain spectral window in the output signal of the cavity. According to our model, the effect is exclusively linked to the effective thermo-optical response of the resonator and, as opposed to EIT and OMIT, it is independent from any atomic or mechanical resonance.

Under static driving conditions, the TO effect manifests itself as a red-shift of the resonance wavelength, which is due to the increase in temperature consequent to the (linear or nonlinear) absorption of the part of the energy of the confined mode [47, 38]. The absorption of light generates heat, which diffuses in the physical cavity volume, producing a variation in the refractive index. This induces, in first order perturbation theory, a proportional variation in the resonance frequency:

$$\bar{\omega}_0 = \omega_0 - \omega_0 \alpha \Delta T \quad (5.1)$$

where ω_0 is the “cold cavity” resonance frequency, $\alpha = \xi_{TO} \frac{1}{n} \frac{dn}{dT} \approx \frac{1}{n} \frac{dn}{dT}$ is the normalized TO coefficient¹ and ΔT is the effective local temperature variation, which we will assume for the moment to be constant over the cavity mode volume. In practice, the value of α can be accurately estimated by evaluating experimentally the variation in the resonance wavelength of a cavity mode as a function of the cavity temperature (see e.g. fig. 4.8). If the temperature variation ΔT is treated as a dynamical variable of the system, one can define, in analogy with the cavity opto-mechanics formalism [84], an effective thermo-optical coupling factor $G = \omega_0 \alpha$ which parametrizes the interaction. Here, the quantity $G \Delta T$ represents the frequency shift associated to the coupling between the optical and thermal systems.

Similarly, in stationary conditions, the temperature of the system will be increased with respect to the thermal bath by a constant amount $\overline{\Delta T}$, which is associated to absorption of the energy of the confined electromagnetic

¹The overlap factor ξ_{TO} introduced in chapter 1 is approximately unitary for a tightly confined dielectric mode and we will neglect it for simplicity.

5.2. Overview

field. According to eq. (1.41), the absorbed power is proportional to the cavity energy U , and it thus provides a constant heat supply:

$$P_{abs}(U) = \bar{\Gamma}_{abs}(U)U \quad (5.2)$$

where $\bar{\Gamma}_{abs}(U) = \Gamma_{abs} + \Gamma_{TPA}(U) + \Gamma_{FCA}(U)$ takes into account the linear and nonlinear contributions to light absorption within the cavity mode volume. For sufficiently low values of cavity energy, the linear term dominates and thus $\bar{\Gamma}_{abs}(U) \approx \Gamma_{abs}$. The diffusion of heat is locally governed by the equation:

$$\rho c_p \frac{\partial(\Delta T)}{\partial t} + \nabla \cdot (-\kappa \nabla(\Delta T)) = \frac{\partial Q}{\partial t} \quad (5.3)$$

where ρ is the density of the material, c_p is the mass specific heat, κ is the thermal conductivity and $\frac{\partial Q}{\partial t}$ is a source term describing the heat flux density towards the system, in this case associated to the optical power absorbed $P_{abs}(U)$. The second term at the left-hand side of the equation represents the local form of Fourier's law for heat conduction. The expression above can be related to the previous treatment by eliminating the spatial dependence of ΔT and Q . In the most simple model [130, 47], this can be done by introducing two effective quantities, namely a heat capacity $C_p = \rho c_p V_{th}$ and the (extensive) thermal conductivity K :

$$C_p \frac{d(\Delta T)}{dt} = P_{abs}(U) - K \Delta T \quad (5.4)$$

where we replaced the forcing term with the absorbed power from the optical field. In this simplified picture, the heated system is modeled by an effective thermal volume V_{th} , which is characterized by a temperature increase ΔT with respect to a thermal bath, to which it is coupled via the thermal conductivity K . In practice, V_{th} is associated to the physical size of the heated region, while K is related to the temperature gradient. Both values can be estimated via stationary heat diffusion simulations, obtained for instance

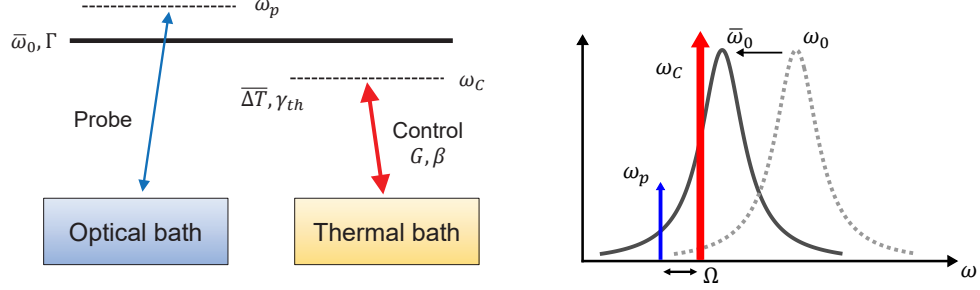


Figure 5.2: Conceptual scheme of a thermo-optically coupled resonator. The physical system (left panel) consists in a resonant mode at frequency $\bar{\omega}_0$, characterized by a decay rate Γ , and a thermal system, characterized by a temperature decay rate γ_{th} , which is out of equilibrium by an offset ΔT with respect to a thermal bath. The optical system is driven by an intense control field oscillating at frequency ω_C and a weak probe field at frequency ω_p . The thermo-optical interaction couples the two systems and it is quantified by the coefficient G . (right panel) Phenomenology of the TO interaction: the “cold” resonator frequency ω_0 is red-shifted by the control field to the lower frequency $\bar{\omega}_0$. The probe field, detuned from the pump by an offset Ω , is used to investigate the spectral properties of the driven resonator.

via finite element method (FEM). In the absence of a driving heat source, eq. (5.4) is characterized by an exponential temperature decay which is described by the rate $\gamma_{th} = K/C_p$, while in the case where the absorbed power is constant, the equilibrium temperature is $\bar{\Delta T} = P_{abs}/K$.

The model given so far describes the stationary behavior of the two quantities which characterize the effect of *thermo-optically induced transparency* (TOIT) that is the object of this chapter. Before detailing the analytical treatment of the dynamical response of the thermo-optical system, we will give a qualitative overview of the phenomenon and introduce the formalism used.

An energy levels schematic of the physical system is shown in fig. 5.2. Suppose that the cavity is driven by an intense control (pump) field $s_{in}(t) = \bar{s}_{in}e^{-i\omega_C t}$, which oscillates at a frequency $\omega_C = \omega_0 + \Delta$, slightly detuned from the “cold” cavity resonance. The absorption of optical energy will produce a temperature shift $\bar{\Delta T}$ which in turn modifies the resonance frequency to

5.2. Overview

$\bar{\omega}_0$. The overall frequency offset with respect to the “hot” cavity is then $\bar{\Delta} = \omega_C - \bar{\omega}_0$. Let us now consider a second weak (probe) field $\delta s_{in}(t) = \delta s_{in} e^{-i\omega_p t}$, with $\delta s_{in} \ll \bar{s}_{in}$, oscillating at frequency $\omega_p = \omega_C + \Omega$. Owing to the detuning with respect to the pump, the field intensity inside the cavity will oscillate at the beating frequency Ω , with a small ripple with respect to the average value U . If the beat frequency is smaller or of the order of the thermal response $\Omega \sim \gamma_{th}$, however, the variation in intensity will affect the temperature dynamics. Since the latter affects in turn the cavity frequency via the TO interaction, this will result in a modulation of the pump field, producing sidebands interfering with the probe field. As a neat effect, depending on the sign and the amount of the interference, the effect results in the induced absorption or amplification of probe itself, which can be observed as a narrow spectral hole or a gain peak in the output signal from the cavity. Anticipating the results that will be detailed in the next section, the phenomenology of the effect, as predicted by the present model of the nonlinear cavity response, is visualized in fig. 5.3.

Summarizing in a simple picture what discussed so far, the physical process can be described as follows:

1. the pump field heats the cavity, producing a (static) thermo-optic red-shift of the Lorentzian resonance;
2. the probe field, detuned by Ω from the pump, induces a beating in the intracavity optical energy, at frequency Ω ;
3. the beating induces the oscillation in time of the temperature, and thus of the cavity resonance frequency;
4. this produces an anti-Stokes (Stokes) shift of frequency $+\Omega$ ($-\Omega$) of the pump field: the shifted pump oscillates out of phase (in phase) with the original probe;
5. the shifted pump field interferes destructively (constructively) with the probe field, resulting in a dip (peak) in the probe output signal from the cavity.

It should be remarked that the effect stems from the interference between pump and probe fields, and it relies on their mutual coherence.

Given the extremely narrow bandwidth of thermal phenomena compared to the optical wavelength, the width of the transparency or gain region results to be of the order of the MHz in the smallest PhC structures. Moreover, due to the Kramers-Krönig type relation which exists between the intensity spectral response and dispersion (fig. 5.1), this is associated to a marked group delay or advance, depending on the detuning conditions at which the interaction occurs, for the probe signal, which can be understood qualitatively as a result of the mutual energy exchange between the electromagnetic field and the thermal reservoir. While the former property is particularly interesting in view of narrow-band filtering applications, the second is even more appealing considering applications to integrated optical delay lines and optical memories. Moreover, the effect is here demonstrated in a standard silicon PhC cavity, but it could be extended in principle to any SOI-based resonator. Finally, the phenomenon does not depend on any mechanical, atomic or acoustic resonance and it thus could be implemented in a cascaded fashion via a series of resonators.

5.3 Theory

With the formalism introduced in the previous section, we hereby derive the fundamental differential equations which describe the dynamics of TOIT.

Consider a lossy optical resonator, characterized by linear and nonlinear absorption of the optical energy, which is affected by thermo-optical interaction. In the formalism of input-output relations [1, 84] (already adopted in chapter 3), this can be described by the following dynamic equations:

$$\frac{da(t)}{dt} = \left(i\Delta - \frac{\Gamma(U)}{2} \right) a(t) + i\omega_0\alpha\Delta T(t)a(t) + \sqrt{\eta\Gamma(U)}s_{in}(t) \quad (5.5a)$$

$$C_p \frac{d(\Delta T)}{dt} = \bar{\Gamma}_{abs}(U)|a(t)|^2 - K\Delta T(t) \quad (5.5b)$$

5.3. Theory

where $a(t)$ is the modal field amplitude, normalized such that $|a(t)|^2$ is the mode energy, $\Gamma(U)$ is the mode decay rate, which depends on the mode energy due to nonlinear effects, according to the definition (1.22), $s_{in}(t)$ is the driving field, expressed such that $|s_{in}(t)|^2$ is the input power, which is related to the cavity coupled power via the coupling efficiency η . The electromagnetic field is expressed in a frame rotating at ω_C , thus enabling a description in terms of the pump-cavity detuning $\Delta = \omega_C - \omega_0$. The terms $\bar{\Gamma}_{abs}$, C_p and K , already introduced in the previous section, represent respectively the (nonlinear) absorption rate for the mode energy, the heat capacity associated the cavity volume and the related thermal conductivity.

Equations (5.5) are nonlinear and mutually coupled via the dynamic variables $a(t)$ and $\Delta T(t)$. In particular, owing to nonlinear absorption effects², the cavity decay rate and the optical absorption rate depend explicitly on the cavity energy. However, we will limit ourselves for simplicity to the case where linear absorption only contributes to heating, while the cavity decay rate depends on both linear absorption and out-of-plane scattering. This approximation is well justified provided that $\Gamma_{abs}/\bar{\Gamma}_{abs}(U) \approx 1$, namely the parasitic absorption from TPA and FCA is low compared to linear absorption. Moreover, in the presence of important nonlinear absorption originated by a strong driving field, the presence of a weak probe allows to model $\bar{\Gamma}_{abs}(U)$ as a static contribution, upon which the problem is linearized.

With these assumptions, the equilibrium solutions to eqs. (5.5) in the presence of the pump field read:

$$\bar{a} = \frac{\sqrt{\eta\bar{\Gamma}}}{-i(\Delta + \omega_0\alpha\overline{\Delta T}) + \Gamma/2} \bar{s}_{in} \quad \overline{\Delta T} = \frac{\Gamma_{abs}}{K} |\bar{a}|^2 \quad (5.6)$$

where $|\bar{a}|^2 = U$ is the intracavity optical energy under constant driving field.

Remarkably, even in the absence of nonlinear absorption, the equations above may have a bistable solution in the presence of appropriate conditions

²We are neglecting the dispersive contributions from FCD and Kerr effects, which are negligible with respect to TO effect in this context.

($\Delta > \frac{\sqrt{3}}{2}\Gamma$ and $|\bar{a}| \gg \bar{a}_b = \sqrt{\frac{K}{2Q\alpha\Gamma_{abs}}}$), as one can deduce by comparison with eq. (1.42). In these conditions, one of the two stable equilibrium solutions should be appropriately chosen [47].

We include now in the model the weak probe field, which in the rotating frame reads $\delta s_{in}(t) = \delta s_{in} e^{-i\Omega t}$, such that $|\delta s_{in}|^2 \ll |\bar{s}_{in}|^2$. The overall driving field is thus given by $s_{in}(t) = \bar{s}_{in} + \delta s_{in}(t)$. We then linearize the equations of motion (5.5) at the equilibrium point: assuming a system response $a(t) = \bar{a} + \delta a(t)$, $\Delta T(t) = \bar{\Delta T} + \delta T(t)$ we can rewrite:

$$\frac{d}{dt}\delta a(t) = \left(i\bar{\Delta} - \frac{\Gamma}{2}\right)\delta a(t) + iG\bar{a}\delta T(t) + \sqrt{\eta\Gamma}\delta s_{in}(t) \quad (5.7a)$$

$$\frac{d}{dt}\delta T(t) = \beta\bar{a}(\delta a(t) + \delta a^*(t)) - \gamma_{th}\delta T(t) \quad (5.7b)$$

where we introduced $\beta = \Gamma_{abs}/C_p$ and we made the hypothesis $\bar{a} \approx \bar{a}^*$ (i.e. we neglected the phase response from the bare resonator). We then make the following ansatz:

$$\delta a(t) = A_p^- e^{-i\Omega t} + A_p^+ e^{+i\Omega t} \quad (5.8a)$$

$$\delta T(t) = T e^{-i\Omega t} + T^* e^{+i\Omega t} \quad (5.8b)$$

where we assumed the temperature being a real quantity. Plugging the above quantities into the equations of motion provides terms oscillating at $\pm\Omega$. By

5.3. Theory

separating these according to the sign, we derive the relations:

$$A_p^- = \frac{iG\bar{a}T + \sqrt{\eta}\Gamma\delta s_{in}}{-i(\bar{\Delta} + \Omega) + \Gamma/2} \quad (5.9a)$$

$$A_p^+ = \frac{iG\bar{a}}{-i(\bar{\Delta} - \Omega) + \Gamma/2} T^* \quad (5.9b)$$

$$T = \frac{\beta\bar{a}}{-i\Omega + \gamma_{th}} (A_p^- + A_p^{+*}) \quad (5.9c)$$

In order to evaluate the effect on the probe, we isolate the component of $a(t)$ oscillating at $-\Omega$. This is given by the term A_p^- , which can be explicitly expressed as:

$$A_p^- = \frac{\sqrt{\eta}\Gamma}{-i(\bar{\Delta} + \Omega) + \Gamma/2 - if(\Omega) \left(1 + \frac{if(\Omega)}{i(\bar{\Delta} + \Omega) + \Gamma/2}\right)^{-1}} \delta s_{in} \quad (5.10)$$

where we introduced the auxiliary function:

$$f(\Omega) = \frac{G|\bar{a}|^2\beta}{-i\Omega + \gamma_{th}} \quad (5.11)$$

which is associated to the thermal response of the system. The expression at the denominator determines the scale of the phenomenon in frequency, while the term at the numerator quantifies the coupling between the optical population and the thermal one for a fixed driving condition.

The expression (5.10) is the counterpart of the general solution to OMIT [128, 129], which, in the “resolved sideband” limit, has analogous form as EIT [124]. However, a mechanical or atomic resonance frequency does not exist in our case, while the thermal system in the linearized regime is characterized by a first-order response (eq. 5.7b), typical of damped systems. Hence, the effect of TOIT bears similarities with OMIT and EIT, and it can be somehow

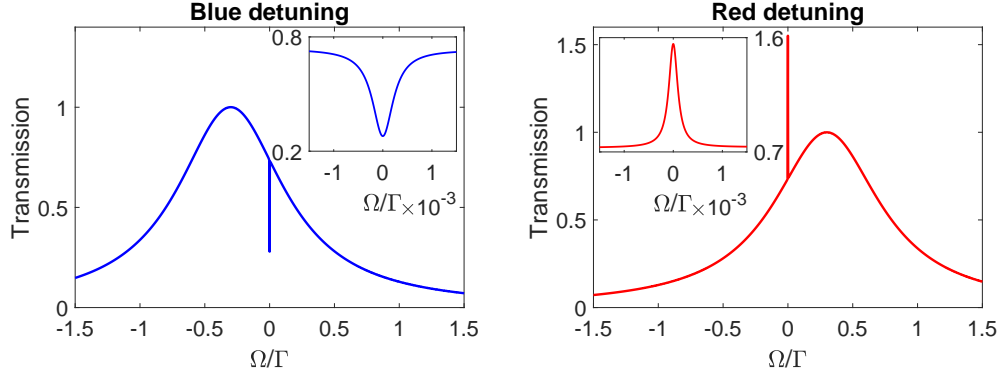


Figure 5.3: Calculated probe transmission spectra at regime of pump blue- and red-detuning with respect to the cavity resonance as a function of the probe-pump detuning Ω . The former is associated to a narrow dip in the transmission spectrum (inset), the latter to an analogous gain feature. The spectra shown here are derived from the theory described in section 5.3. For the calculation we chose $\bar{\Delta} = \pm 0.3\Gamma$.

compared by setting a vanishing mechanical (atomic) resonance frequency $\Omega_m \rightarrow 0$ ($\omega_{31} \approx \omega_{32}$ in EIT).

Fig. 5.3 shows a plot of the probe response for different pumping conditions. In the blue-detuning regime ($\omega_C > \bar{\omega}_0$), the effect manifests itself as a narrow dip in the resonance spectrum at frequency ω_C , characterized by a FWHM of the order of γ_{th} . Conversely, if the pump is tuned on the red side of the spectrum ($\omega_C < \bar{\omega}_0$), the effect manifests itself analogously as a gain peak. In both cases, the visibility depends on the intensity of the control field $|\bar{a}|^2$. Remarkably, the central frequency of the spectral window for the effect can be tuned arbitrarily within the bandwidth of the optical resonance, as the position of the absorption (gain) window only depends on the frequency of the control field.

The expression (5.10) is a complex quantity with the dimensions of a field (specifically $|A_p^-|^2$ has dimensions of an energy). In order to relate this with an experimentally measurable quantity, it is convenient to formalize again the problem by means of the input-output formalism. In this framework, the system consisting in the lossy optical resonator and two excitation/decay channels is equivalent to the scattering problem sketched in fig. 5.4. According to the formalism introduced so far, the excitation mode at

5.3. Theory

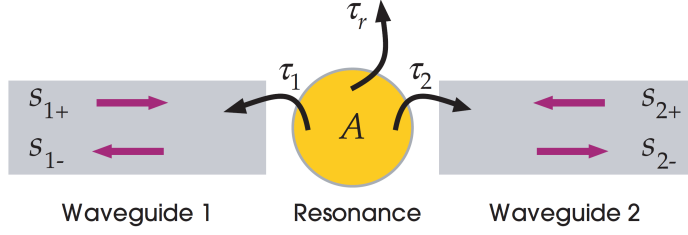


Figure 5.4: Schematic of the coupling scheme for an optical resonator. The localized mode is coupled to two scattering channels (here visualized as two waveguides) and to a loss channel, with rates $\Gamma_i = 1/\tau_i$. In RS configuration, the two scattering modes S_1 and S_2 can be interpreted as the vertical and horizontal polarizations. Note that in this configuration the coupling efficiency is given by $\eta = \Gamma_i/(\Gamma_1 + \Gamma_2 + \Gamma_r)$ for excitation from channel i . Figure from [1].

the input is characterized by a coupling rate $\eta\Gamma$: the reflected field amplitude s_{out}^r originates then from the interference between the impinging mode and a contribution from the cavity, such that $s_{out}^r = s_{in} - \sqrt{\eta\Gamma}a$. On the other hand, the transmitted signal will only be originated by the decay of the mode towards the second channel, so the transmitted field amplitude is given by: $s_{out}^t = -\sqrt{\eta\Gamma}a$, where we assumed equal coupling rate for input and output. By normalizing on the input amplitude, we obtain the reflection and transmission coefficients, which for the probe signal oscillating at $-\Omega$ read:

$$\mathcal{R} = \mathcal{R}_{RS}^{\parallel} = \frac{|\delta s_{out}^r|^2}{|\delta s_{in}|^2} = \left| 1 - \frac{\sqrt{\eta\Gamma}A_p^-}{\delta s_{in}} \right|^2 \quad (5.12)$$

$$\mathcal{T} = \mathcal{R}_{RS}^{\perp} = \frac{|\delta s_{out}^t|^2}{|\delta s_{in}|^2} = \left| \frac{-\sqrt{\eta\Gamma}A_p^-}{\delta s_{in}} \right|^2 \quad (5.13)$$

The transmission coefficient in particular is proportional to $|A_p^-|^2$ and it can be used to directly probe the response of the phenomenon in amplitude³. It

³It should be remarked that experiments may be able to access to quantities which slightly differ from this definition. As we shall see in section 5.4, owing to the nonlinear nature of the phenomenon, the lock-in detection technique provides for instance a direct measurement of $R_{LI} \propto |A_p^-|^2 + |A_p^-|^2$, rather than the term $|A_p^-|^2$ alone. Nevertheless,

should be noted that the expression above defines generalized reflection and transmission coefficients for any (symmetric) scattering problem of this type, independently on the actually transmitted or reflected signal.

In cross-polarized RS spectroscopy, in particular, the two loading channels can be identified in the two polarizations of free-space modes impinging from the microscope objective. In this context, the crossed polarization response \mathcal{R}_{RS}^\perp is proportional to the transmission coefficient \mathcal{T} , being the two channels orthogonal. Conversely, the reflected spectrum $\mathcal{R}_{RS}^\parallel$ analyzed in the same polarization of the excitation beam is proportional to \mathcal{R} . The coupling efficiency η presented here can be in this framework related to the usual coupling efficiency of the cavity $\eta_c = P_{coupled}/P_{incident}$, obtained in optimal coupling conditions (i.e. cavity mode aligned to the impinging polarization) via the relation $\eta = (1 - \eta_{abs})\eta_c/4$, where the factor 4 accounts for both the 45° orientation of the cavity in the RS scheme and for the loss towards the substrate, while the factor $\eta_{abs} = \bar{\Gamma}_{abs}/\Gamma$ accounts for the absorption from the material (see section 5.4).

The term at the denominator of expression (5.10) proportional to $if(\Omega)$ is responsible for the narrow absorption or gain feature in the transmission spectrum. Associated to such feature, a steep phase response can also be appreciated. Since the group delay is related to the derivative of the phase, in correspondence of the narrow spectral peak (dip) a marked group delay (advance) is also observed. The phase response of the transmitted signal⁴ reads:

$$\phi_t = \arg \left\{ \frac{\delta s_{out}^t}{\delta s_{in}} \right\} = \arg \left\{ \frac{A_p^-}{\delta s_{in}} \right\} \quad (5.14)$$

while the group delay associated can be expressed as:

$$\tau_d = -\frac{d\phi_t}{d\omega} = -\frac{d}{d\omega} \arg \left\{ \frac{A_p^-}{\delta s_{in}} \right\} \quad (5.15)$$

this distinction is not critical in most of the cases, as in practice $|A_p^-|^2 \gg |A_p^+|^2$.

⁴See footnote 3: as for the case of amplitude, the phase response measured experimentally may result slightly different to the predicted one, including terms proportional to A_p^+ .

5.4. Experiments

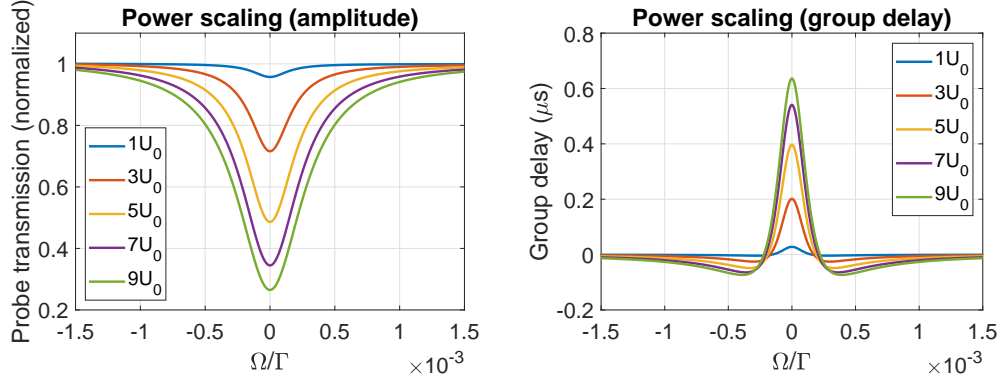


Figure 5.5: Predicted transmission (left) and group delay (right) spectra for increasing values of cavity energy U/U_0 . The amplitude plot is normalized on the edge values of the curves. The phenomenon intensity, in terms of visibility and peak group delay, increases with the optical energy.

Fig. 5.3, already discussed, shows the broadband response of the phenomenon calculated with the above model. Fig. 5.5 shows the predicted scaling behavior of the phenomenon, in terms of probe transmission and group delay, as for increasing values of the energy $U = |\bar{a}|^2$ stored within the cavity mode.

Finally, fig. 5.6 shows the theoretical estimation of TOIT transmission and group delay as a function of both pump-resonance detuning and probe-pump detuning. The calculation implements a model slightly more sophisticated than the one detailed so far, which includes multiple characteristic thermal decay rates in order to better reproduce the experimental results (see section 5.4.3). A comparison with the experimental results shown in fig. 5.12 suggests the suitability of this refined model to correctly capture the key features of the experimental observation, which we are going to describe in the next paragraph and constitute one of the main results of the present work.

5.4 Experiments

The experimental verification of TOIT was realized using planar silicon photonic crystal cavities in RS measurement configuration. The cavity geometry,

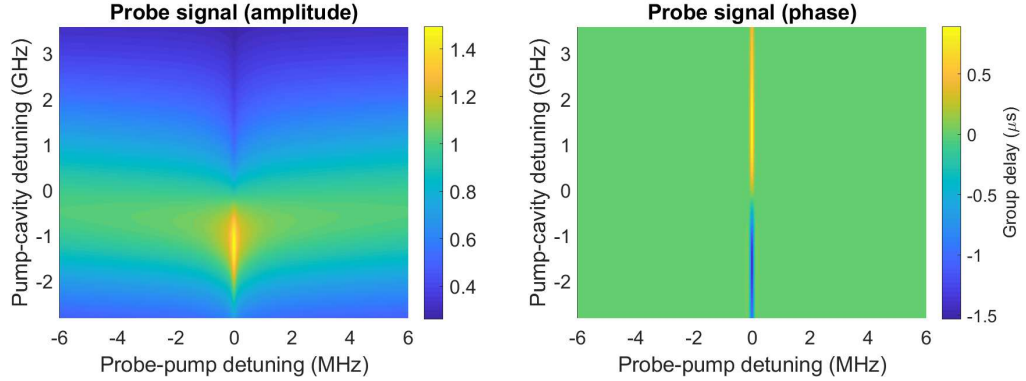


Figure 5.6: Predicted probe transmission (left) and group delay (right) as a function of both pump-probe detuning (horizontal axis) and pump-cavity detuning (vertical). The model adopted here refines the one discussed in this section by including multiple thermal volumes and correspondent decay rates. The plots predict qualitatively and partially quantitatively the experimental results shown in fig. 5.12.

shown in fig. 5.7a consists in a *dispersion-adapted* (DA) layout [48], which is based on a W1 line defect where a tapered increase of the waveguide width (similarly to the A1 design, discussed in chapter 4) is introduced in order to induce the confinement of a localized mode. This was demonstrated to yield a Gaussian mode envelope (fig. 5.7b), diffraction limited mode volume $V \approx 2(\lambda/n)^3$ and a good compromise between Q ($> 10^6$) and robustness to fabrication disorder. A digital lithographic tuning (in steps of $\Delta r = 3$ nm) of the far-field optimization was introduced in order to improve the vertical coupling efficiency from free space.

The cavities were fabricated (fig. 5.7c) in SOI with 220 nm thick device layer and 2 μm thick BOX. EBL was performed at 30 kV acceleration voltage on a ZEP-520A resist developed in Xylene. Dry etching was performed using a SF_6/CHF_3 gas chemistry and underetched with HF.

5.4.1 Resonator characterization

As a preliminary measure, the linear response of the cavities was characterized via RS spectroscopy, as detailed in chapter 2. We selected, among the others, a device with lattice step $a = 420$ nm, hole radius $r/a = 0.3$ and

5.4. Experiments

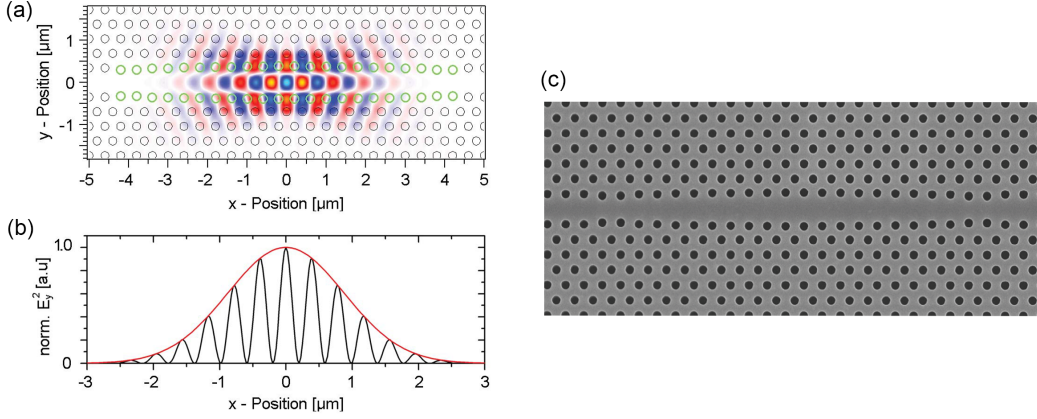


Figure 5.7: (a) Layout and simulated field profile E_y for a DA PhC cavity. The green dots are symmetrically shifted along the y axis. (b) Squared field distribution $|E_y|^2$ along the $y = z = 0$ line and Gaussian envelope (red). (c) SEM image of a fabricated DA cavity. Figures from [48].

far-field optimization $\Delta r = +9$ nm. This combination resulted in a resonance at telecom wavelength ($\lambda_0 = 1548.45$ nm) and a good compromise between quality factor $Q = 3.8 \times 10^4$, estimated from Fano fit of the experimental data, and coupling efficiency $\eta_c = 11\%$. The latter was estimated by comparing the scattered signal from the far-field optimized device, collected with a free-space detector, with a reference mirror and parallel polarizers, and taking into account the correction factor linked to crossed-polarization and to the emission towards the substrate. The experimentally measured RS spectrum is shown in fig. 5.8.

The RS technique was also used to estimate the parameters related to TO effect, namely α and Γ_{abs} . The TO coefficient was measured $\alpha = \xi_{TO} \frac{1}{n} \frac{dn}{dT} = 6.6 \text{ K}^{-1}$. This was determined by varying the device temperature via a calibrated thermo-electric cooler (TEC) controlled by a PID feedback loop, measuring the corresponding resonance wavelength variation from the RS spectrum, and thus extrapolating the datum by linear fit of the experimental data.

The parameter Γ_{abs} , related to linear absorption for low intracavity intensity, can be estimated by measuring the resonance shift as a function of the coupled power. We performed this measurement by systematically in-

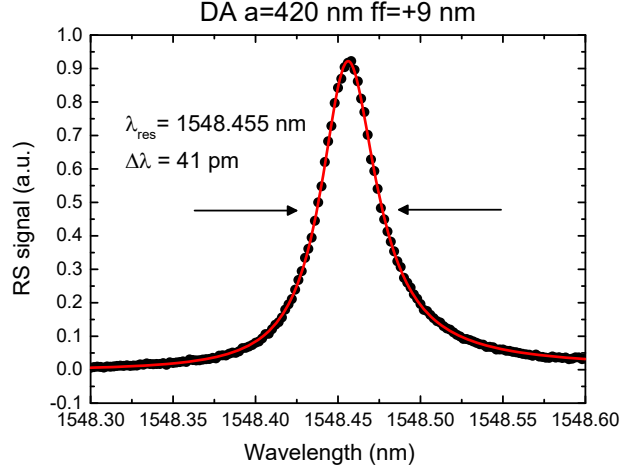


Figure 5.8: Measured RS spectrum of the DA cavity exploited for TOIT experiments. The design parameters are $a = 420$ nm, $r/a = 0.3$, $\Delta r = +9$ nm. The selected mode exhibits a resonance at telecom wavelength, $Q = 3.8 \times 10^4$ and a coupling efficiency $\eta_c = 11\%$. Points represent experimental data, solid red line is the Fano fit.

creasing the input power at the RS setup and recording the bistable response from the cavity (fig. 5.9a). We performed a fit of the experimental data by analytically solving the model for a bistable cavity eq. (1.42) and taking the root with highest value. From this, we obtained the overall shift trend of the mode resonance at different input power (fig. 5.9b), which is characterized by a red-shift, pointing to the dominant role of TO shift over other dispersive effects (Kerr, FCD) at low power.

With this procedure, we measured a normalized power-dependent TO coefficient:

$$\xi_p = \frac{1}{\lambda_0} \frac{d\lambda_0}{dP_{coupled}} = 2.6 \pm 0.3 \text{ W}^{-1} \quad (5.16)$$

By solving the rate equations (5.5) at steady state regime, one can calculate from this value the absorption rate Γ_{abs} , which is given by the expression:

$$\Gamma_{abs} = \frac{2\pi c}{\lambda_0 Q} \frac{K}{\alpha} \xi_p = 1.9 \times 10^{10} \text{ rad/s} \quad (5.17)$$

5.4. Experiments

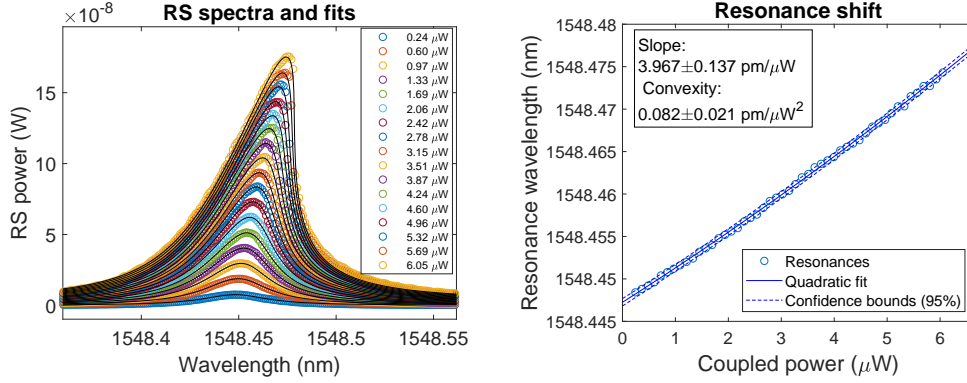


Figure 5.9: RS spectra (left panel) of the cavity mode for increasing incident power. The spectra are acquired by scanning the laser from shorter to longer wavelength. The estimated peak coupled power is shown in the legend. Each curve is fitted (black lines) with a bistable line model, obtained by analytically solving eq. (1.42) as a function of P_{out} and taking the highest-value solution. The peak resonance wavelength so estimated (right panel) is shown to follow a linear shift trend as a function of peak coupled power, with a slight convexity due to nonlinear absorption effects.

where for the calculation we assumed $K \approx 2\pi t\kappa = 8.3 \times 10^{-5}$ W/K, where t is the device layer thickness and $\kappa = 60$ W/(m·K) is the thermal conductivity of holey silicon [131, 132, 133]. It is perhaps instructive to compare this value with the overall cavity linewidth: the quantity $\eta_{abs} = \Gamma_{abs}/\Gamma \approx 0.30$ suggests that an important decay channel for the intracavity optical energy consists actually in the linear absorption processes associated to defects and localized electronic states at the interfaces. This numerical result is consistent with the one given by other authors [38] and corroborates the hypothesis that the high Q factor of silicon PhC cavities suspended in air is ultimately limited by absorption processes [42].

5.4.2 High resolution pump and probe spectroscopy

Experimental apparatus

The narrow-bandwidth nature of the phenomenon under investigation and the weak output signal from PhC cavities make the spectroscopic character-

ization of TOIT challenging with a traditional pump and probe technique, requiring a spectral resolution of the order of 100 kHz on the optical signal. In order to address the problem, we developed a high-resolution pump and probe technique based on a single-sideband type modulation of the control field, similar to the approach adopted for similar experiments involving sharp spectral features [134, 129, 127]. The experimental scheme is shown in fig. 5.10: the infrared radiation emitted from a tunable ECL source (Santec TSL-710) is coupled to a fiber-based Mach-Zehnder interferometer (MZI). On one arm of the interferometer, light is coupled to a series of two acousto-optic modulators (AOM). The two fiber-coupled AOMs (AA opto-electronic MT80-B10-IIR30) are designed [135] to be fed by a RF signal centered at 80 MHz, which excites an acoustic wave inside the device that is used to modulate the impinging light beam. The travelling grating created by the acoustic wave diffracts the beam and couples only the first order $m = \pm 1$ with high transmission efficiency within the design bandwidth ($70 \div 90$ MHz). The interaction of the light beam with the acoustic wave can be visualized as the inelastic scattering of the optical photon with the acoustic phonons of the material. As a consequence of conservation of energy, the outgoing photon is frequency shifted by the modulation frequency $\pm\omega_{mod}$. Of the two AOMs put in series, the first one exploits the order $m = -1$ of diffraction of the grating, which results in a negative shift $-\omega_{mod,1}$ of the optical frequency (red-shift), while the second one works at the $m = +1$, yielding a positive shift $+\omega_{mod,2}$. As a result, light at the second arm of the MZI has frequency:

$$\omega_p = \omega_C - \omega_{mod,1} + \omega_{mod,2} = \omega_C + \Omega$$

In practice, the driving frequency of the first AOM is kept fixed at $\omega_{mod,1}/2\pi = 80$ MHz, while the one of the second modulator is varied between the diffraction bandwidth of the device ($70 \div 90$ MHz), in order to allow a spectral scan of the phenomenon within a bandwidth of approximately 20 MHz. In order to separate the probe signal from the pump background, a second modulation at low frequency ($\Omega_{LI}/2\pi = 29$ kHz) is superimposed to the signal driving

5.4. Experiments

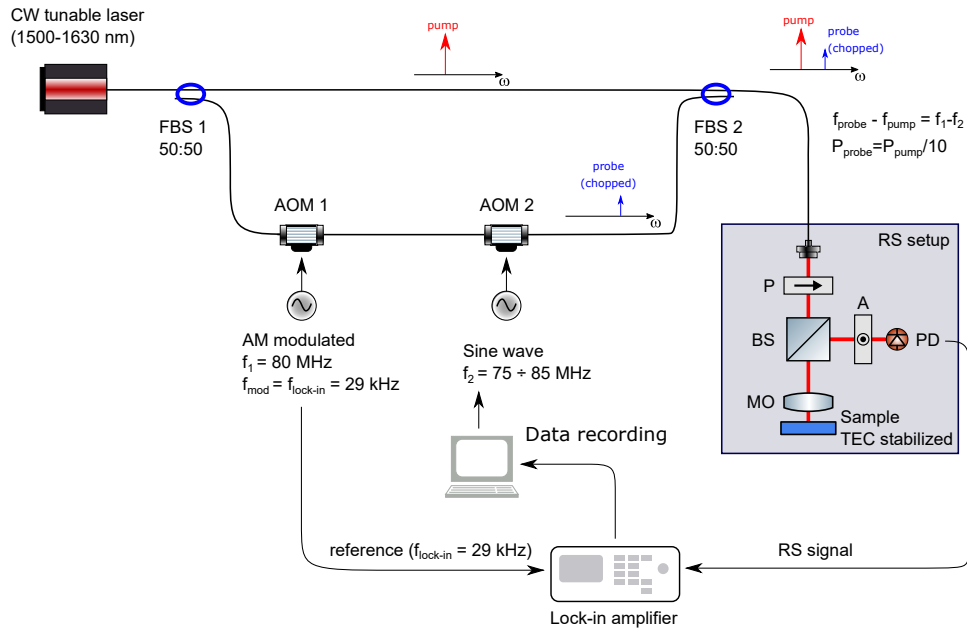


Figure 5.10: Schematic of the experimental setup used for high-resolution pump and probe RS. The light from an ECL source (Santec TSL-710) is separated in two arms via a 50:50 fiber beam-splitter (FBS). In the first path the signal is simply transmitted, while in the second arm, the optical frequency is shifted by Ω via a cascade of two AOMs and the probe signal so generated is chopped at the LI frequency Ω_{LI} . The two fields are recombined via a second FBS and the amplitudes are adjusted such that the pump power is approximately 10 times higher than the probe. The final signal feeds the RS setup, and it is eventually detected and analyzed by a LI amplifier, controlled by a computer data acquisition system. The modulating frequencies are generated by a two-channel function generator.

the first AOM and the modulating signal $m(t) = \frac{1}{2} [1 + m_{LI} \cos(\Omega_{LI}t)]$ is sent as reference to a lock-in (LI) amplifier (Ametek Signal Recovery 7265). Ultimately, the probe field so generated is recombined with the pump signal at the first arm of the MZI, and the resulting field is used as feed for the RS setup. This is given by the expression:

$$s_{in}(t) = \bar{s}_{in} e^{-i\omega_C t} + m(t) \delta s_{in} e^{-i(\omega_C + \Omega)t} \quad (5.18)$$

where $|\delta s_{in}|^2 / |\bar{s}_{in}|^2 \approx 1/10$. At the output of the RS setup, the light from the cavity is collected by a single-mode optical fiber and photodetected (Thorlabs PDB450C photodiode). The signal from the detector is sent at the input of the LI amplifier for comparison with the reference.

The whole apparatus records both the amplitude of the output component oscillating at frequency Ω_{LI} and its phase. The input signal (5.18) has the same form of the one introduced in section 5.3, except for the lock-in modulation, which can be considered quasi-static as long as $\Omega_{LI} \ll |\Omega|$.

The expression of the output signal is much more complicated owing to the nonlinear response of the system, which introduces many frequency components. However, the LI amplifier detects only the component oscillating at Ω_{LI} . Selecting only these terms from the expression of the photocurrent, we derive the following expression for the measured photocurrent:

$$I_{LI}(t) = \sigma_{PD} \frac{\eta \Gamma}{4} R_{LI} \cos(\Omega_{LI}t + \phi_{LI}) \quad (5.19)$$

where $\sigma_{PD} = 1.0$ A/W is the detector responsivity, while $R_{LI} = m_{LI} (|A_p^-|^2 + |A_p^+|^2)$ and ϕ_{LI} are the terms proportional to the final amplitude and phase redouts of the instrument. The latter quantity in particular is linked to the group delay (5.15) via the relation:

$$\tau_d = \frac{\phi_{LI}}{\Omega_{LI}} \quad (5.20)$$

5.4. Experiments

The whole experimental apparatus is automatized via a computer-based control over the instruments. In particular, the probe frequency Ω is scanned by controlling the function generator driving AOM 2, while the LI readouts are recorded point-by-point. Additionally, the computer-based interface varies the output power and the wavelength of the driving laser, thus allowing scans of the experimental parameters over different degrees of freedom.

Given the extremely highly precise control over the modulation frequency, the spectral resolution of the system is ultimately limited by the linewidth of the laser, which is specified < 100 kHz.

Results

Preliminary results were obtained using standard pump and probe technique, consisting in two dedicated ECL sources for pump and probe, in combination with the RS apparatus. These measurements do not have the required resolution for the characterization of the phenomenon, but they allow to appreciate some qualitative aspects. Fig. 5.11 shows three unresolved probe transmission spectra obtained with this technique at different pumping conditions, namely large and slight blue-detuning and red-detuning. Although the spectral feature under investigation is not fully resolved, the qualitative behavior above discussed can be already appreciated, with a positive or negative transparency window which sign depends on the detuning between pump and hot cavity resonance.

The results from high-resolution (HR) pump and probe measurements with the technique discussed above are presented in fig. 5.12. Here the pump-probe detuning Ω (horizontal axis) is varied together with the pump-cavity detuning Δ (vertical axis). The crossover from absorption to gain regime can be appreciated along the vertical direction, with a dip visibility (left panel) approaching unity. In correspondence of the “hot cavity” resonance frequency ($\bar{\Delta} \approx 0$), the phenomenon is not observed. The maximum visibility is observed for $\Omega \approx 0$, while for pump-probe detuning greater than few MHz, the usual cavity RS signal is observed. An analogous behavior can be appreciated for the group delay (right panel), acquired together with the

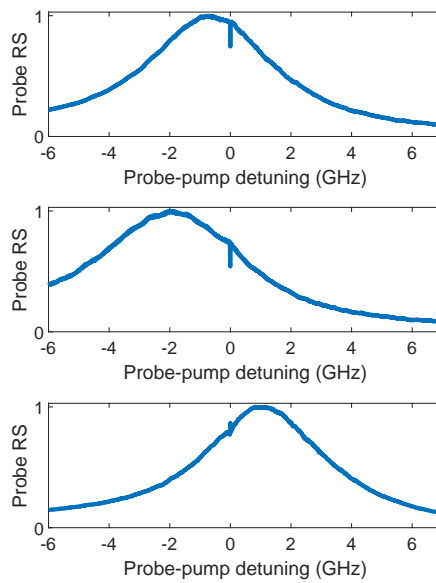


Figure 5.11: Broadband spectra of the probe signal (normalized on the cavity resonance) obtained in a standard pump and probe configuration. Upper and central panels show the effect at blue-detuning of the pump with respect to the hot resonance, which are associated to a spectral dip. The third panel shows the same measurement performed at red-detuning regime, where a gain peak is observed. The measurement is not fully resolved due to the limited accuracy of the laser sources, but the qualitative behavior of the effect can be appreciated.

5.4. Experiments

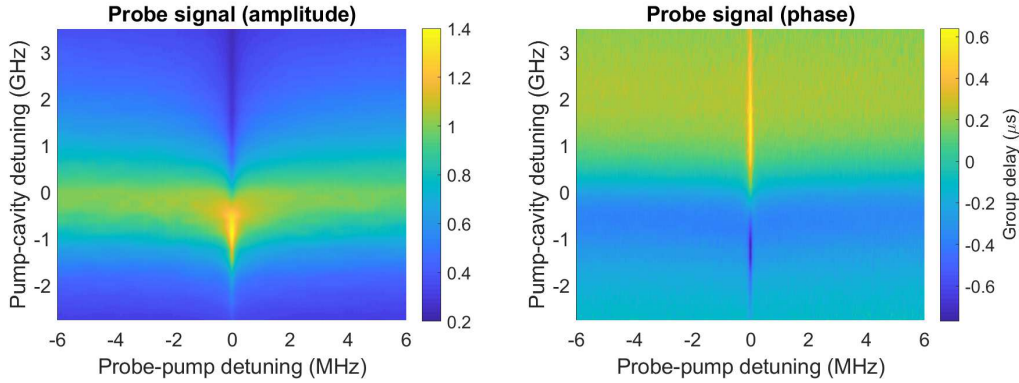


Figure 5.12: Intensity (left) and group delay (right) plots for measured probe transmission as a function of both the probe-pump detuning Ω and the pump-cavity detuning Δ . The measurements were acquired at constant and relatively low nominal power. Horizontal slices are independent scans, and a total of 51 scans were acquired for the measurement. The vertical slice in the intensity plot at large probe-pump detuning matches the usual resonance spectrum for the bare resonator. Note the crossover from induced gain to absorption regime in the vertical direction in correspondence of $\Omega \approx 0$.

probe signal amplitude. Here, the phase response is associated with a positive (negative) value of τ_g when the pump is tuned on the blue (red) side of the resonance spectrum. Although the hereby spectral measurements are acquired at low input power, the group delay response is still much more intense than the background phase response from the bare resonator.

Fig. 5.13 shows a scaling result for the phenomenon for varying coupled power, at blue-detuning regime. The dip visibility increases for increasing coupled power, until it approaches unity. It should be remarked that, owing to the static TO shift of the cavity resonance, the detuning $\bar{\Delta}$ is also varied, and the overall response normalized on the input power is consequently affected. The left panel of the same figure shows the group delay, calculated from the phase response of the instrument, which reaches a peak value of $\sim 4 \mu\text{s}$ for the maximum coupled power and vanishing pump-probe detuning.

In contrast with the theoretical results discussed so far, the experimental data here presented highlight a limitation of the model. The experimental data are here fitted by the sum of two Lorentzian lineshapes, with good accuracy, while a single Lorentzian fit, which would approximate well the

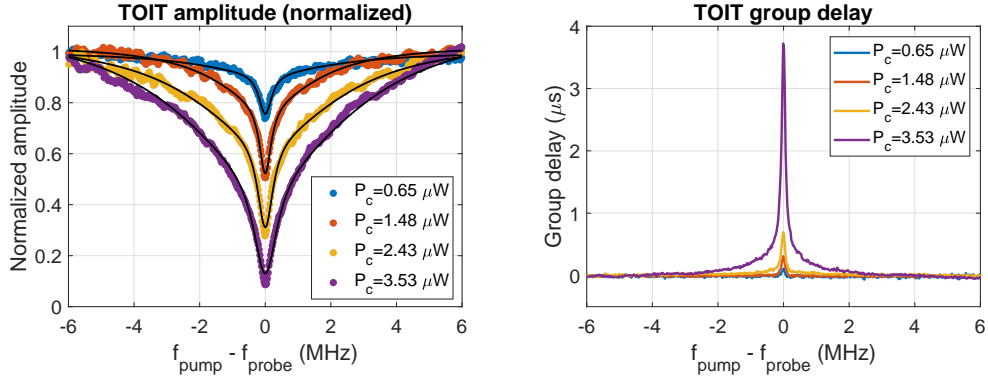


Figure 5.13: Measured intensity (left) and group delay (right) plots for TOIT at *blue*-detuning regime. The coupled power P_c is estimated by monitoring the RS signal. The probe amplitude spectra are normalized on the tails of the spectral dip. Solid black lines are best fit of the experimental data obtained with a two-Lorentzians model (see main text). The group delay is similarly referenced on the values corresponding to large pump-probe detuning.

expression for transmission that we derived in sect. 5.3 for $\Omega \sim \gamma_{th}$, fails to predict correctly the experimental result. We believe this behavior is associated to the diffusive dynamics of the thermal process which originates TOIT: in particular, the assumption of a single thermal decay rate γ_{th} governing the whole thermal decay seems to be not sufficient to well approximate the physics of heat diffusion. The solution we adopted, already investigated by other authors [47], is to include to the model two (or more) distinct thermal decay rates $\gamma_{th,1}$ and $\gamma_{th,2}$, associated to different thermal volumes (see section 5.4.3): qualitatively, we can imagine the heat being first generated within the localized mode region, and then to diffuse more slowly towards the rest of the PhC structure. In a simplified picture, the two decay processes can be considered independent: for this reason, as aforementioned, we fitted the experimental data with the sum of two Lorentzian lineshapes, both centered at $\Omega = 0$, assuming the width and intensity of each of them to be associated with the respective thermal processes.

Fig. 5.14 shows the phenomenon behavior at red-detuning regime, with increasing gain peak visibility and associated group advance for higher coupled power. The measurement at this regime is complicated by the emergence of TO static shift and TO bistability: the scaling of input power results

5.4. Experiments

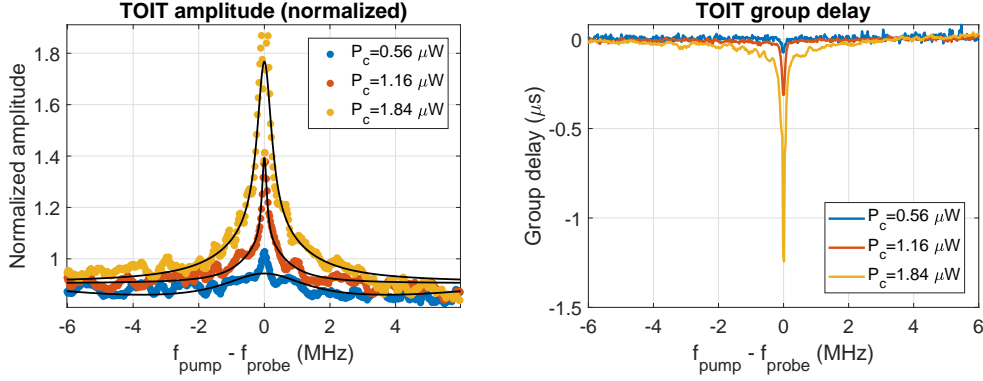


Figure 5.14: Measured intensity (left) and group delay (right) plots for TOIT at *red*-detuning regime.

eventually in a crossover from red- to blue-detuning regime, as shown by the contour plot in fig. 5.15. This feature is also observable in the asymmetric response in the maximum group delay (advance) achieved as a function of the pump-cavity detuning (fig. 5.16).

Following the two-Lorentzians model (two thermal decay rates), we provide the significant scaling trends for the quantities of interest. Fig. 5.17 shows the visibility of the dip (related to the data in fig. 5.13) as a function of the coupled power, following an approximately linear trend. Fig. 5.18 shows the FWHM obtained from best fit of the same data with two Lorentzian lineshapes. Following a similar argument as [128], we can estimate the natural thermal decay rate from the intercept of the linear fit with the vertical axis, obtaining two distinct rates $\gamma_{th,1}/2\pi \approx 0.2$ MHz and $\gamma_{th,2}/2\pi \approx 3$ MHz. Treating the two decay rates as two separate phenomena, it can be shown that the width of the transmission window increases proportionally to the coupled power $P_{coupled} \propto f_i(\Omega = 0)/\Gamma = G|\bar{a}|^2\beta_i/\gamma_{th,i}\Gamma =: C_i$. Following this analogy, the quantity C_i represents the *cooperativity* of the coupled thermo-optical system, and the FWHM of the two Lorentzians is given by:

$$\Gamma_{TOIT,i} = \gamma_{th,i}(1 + C_i) \quad (5.21)$$

The presence of two distinct decay rates makes non-trivial the estimate

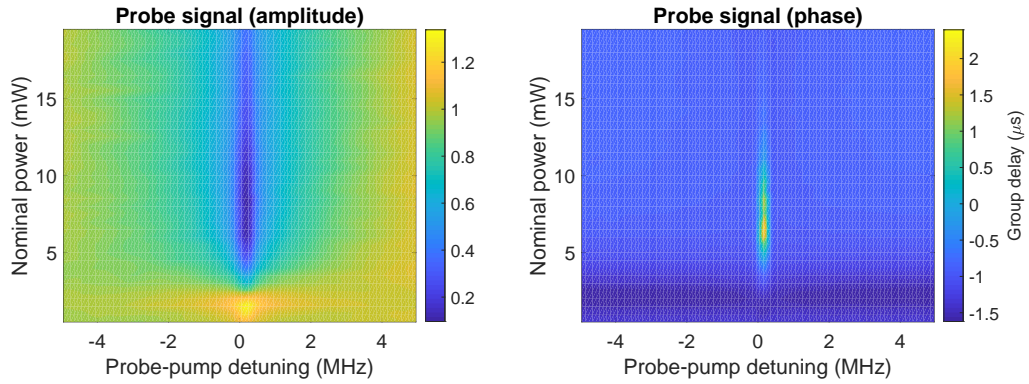


Figure 5.15: Probe intensity (left) and group delay (right) as a function of pump-probe detuning Ω and of the nominal pump power. The intensity signal is normalized on the value obtained for $\Omega \approx 5$ MHz. For low pump power, the driving field is in slight red-detuning conditions, and a gain peak, associated with group advance, is visible. As the power increases, the resonant mode experiences static TO shift, which brings the pump at blue-detuning regime. The maximum intensity of the phenomenon is identified for a pump power of approximately 7 mW, after which the large static TO effect reduces the overall efficiency of the phenomenon.

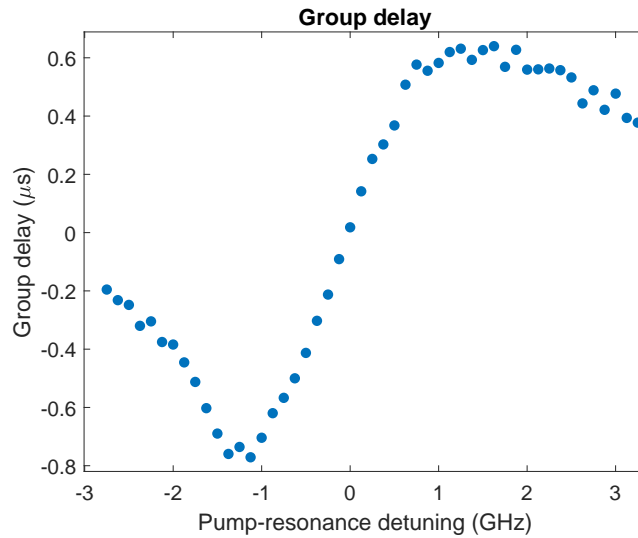


Figure 5.16: Peak group delay (advance) as a function of the pump/cold-cavity detuning, referred to the measurement shown in fig. 5.12. The crossover from gain to absorption regime is appreciable. The asymmetric shape of the curve is due to the presence of the static TO red-shift, which makes the gain region less stable.

5.4. Experiments

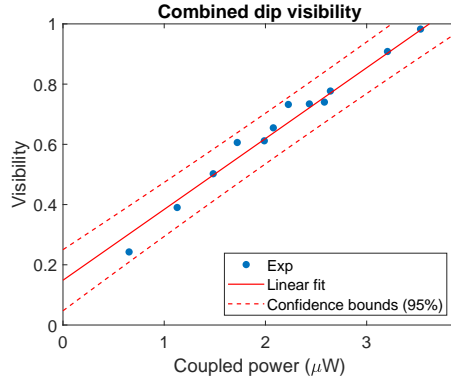


Figure 5.17: Dip visibility as a function of the coupled pump power. The experimental data are referred to fig. 5.13. The calculated visibility is obtained from two-Lorentzian fit (combined dip intensity) of the probe spectral response and normalized on the background signal.

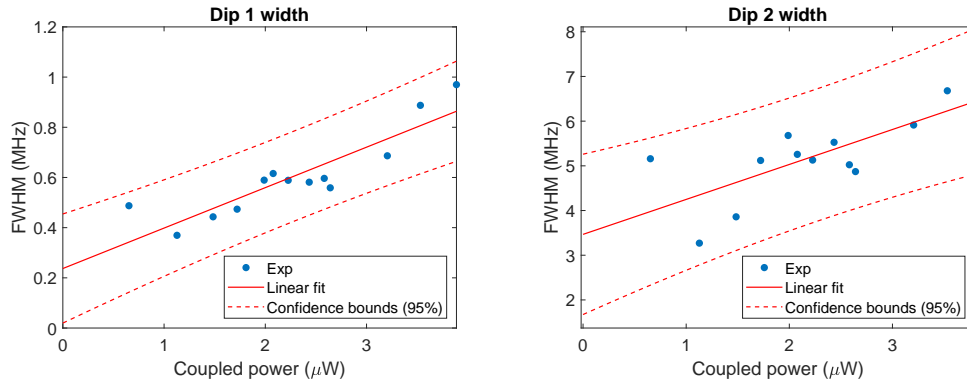


Figure 5.18: Estimated dip width (FWHM) $\Gamma_{TOIT,1}$ and $\Gamma_{TOIT,2}$, calculated from best fit of the experimental data shown in fig. 5.13 with a two-Lorentzians model. The two panels correspond to the values for the two Lorentzian lineshapes involved.

of the maximum group delay achievable. In the two-Lorentzian approach, one can associate each Lorentz-type response to a group delay, such that the overall value will be given by $\tau_g = \tau_{g,1} + \tau_{g,2}$. Because of time-bandwidth limit, the maximum delay theoretically achievable is $\tau_{g,i} \approx 2/\Gamma_{TOIT,i}$, which corresponds to the data presented here. This value is larger than the best ones reported for OMIT [129], being the phenomenon bandwidth more narrow.

Moreover, the measurement here described are limited by the finite linewidth of the laser source $\delta\omega_{laser}$, which makes the spectral region $\Omega < \delta\omega_{laser}$ not accessible⁵ to measurement. Nevertheless, the phenomenon may exhibit an even slower thermal response, characterized one or more additional thermal decay rates, for extremely small detuning, making the maximum delay achievable even higher. Similarly, different geometries characterized by larger mode volumes (e.g. ring resonators) and thus exhibiting slower thermal decay, could be used to achieve higher values of group delay. Notably, this property is inherently subject to the limitation set by the time-bandwidth relation, but given the arbitrary tunability of the control field in frequency, they can be in principle extended over a wide set of frequencies by exploiting multiple resonators in cascade.

5.4.3 Dynamical response

In order to validate our model and to better estimate the characteristic thermal rates, we performed a systematic study of the dynamical TO response of the cavity. The dynamical measurements were obtained by exciting the sample in the RS configuration with a step-like driving field tuned on the red side of the cold resonance.

The experimental apparatus is shown in fig. 5.19. The light from the ECL source is modulated by an intensity electro-optical modulator (EOM), biased at the V_π voltage. This is driven by a function generator which outputs a square wave with rise time < 1 ns and sufficiently low frequency (~ 50 kHz). The signal at the output of the RS setup is detected with a fast InGaAs

⁵In these conditions, the coherent interference between pump and probe at the MZI results in experimental artifacts.

5.4. Experiments

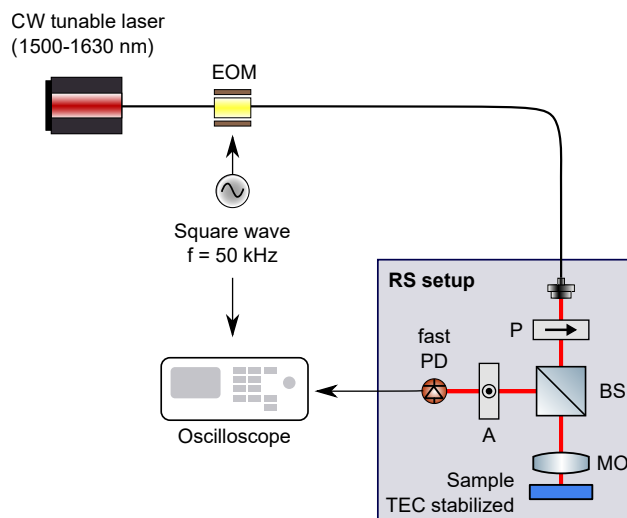


Figure 5.19: Schematic of the experimental setup used to probe the time-domain response of TO effect. The light emitted from a tunable source is modulated by a square-wave signal with fast rise time. This is also used as trigger for an oscilloscope where the RS signal is visualized. The electrical bandwidth of the system is approximately ~ 600 MHz.

photodiode and recorded by a wide-band oscilloscope.

Fig. 5.20 shows the recorded data for four different values of laser power and varying initial cavity-laser detuning. The dynamics occurs on a timescale of the order of few microseconds, consistently with the previous considerations, and it is faster for lower detuning and higher input power. The peak value of the plotted diagrams corresponds to the crossover from red- to blue-detuning regime, and it is associated to the maximum power coupled to the cavity. The asymptotic settling value is associated to the equilibrium solution $|\bar{a}|^2$ to eq. (5.5), and it is larger for higher values of detuning. Similarly, the different values of transmitted signal at the switch-on time correspond to different initial detunings from the cold-cavity resonance.

A similar result is shown in fig. 5.21, where instead of the detuning, we varied the nominal input power, and the normalized RS signal is plotted. The black dotted line represent the numerically calculated response of the system according to the model of eqs. (5.5), where we chose the heat capacity $C_{p,1} = \rho c_p V_{th,1} = 2.4 \times 10^{-12}$ J/K, corresponding to a thermal volume $V_{th,1} = 1.5 \mu\text{m}^3$, which is approximately the physical volume of bulk silicon

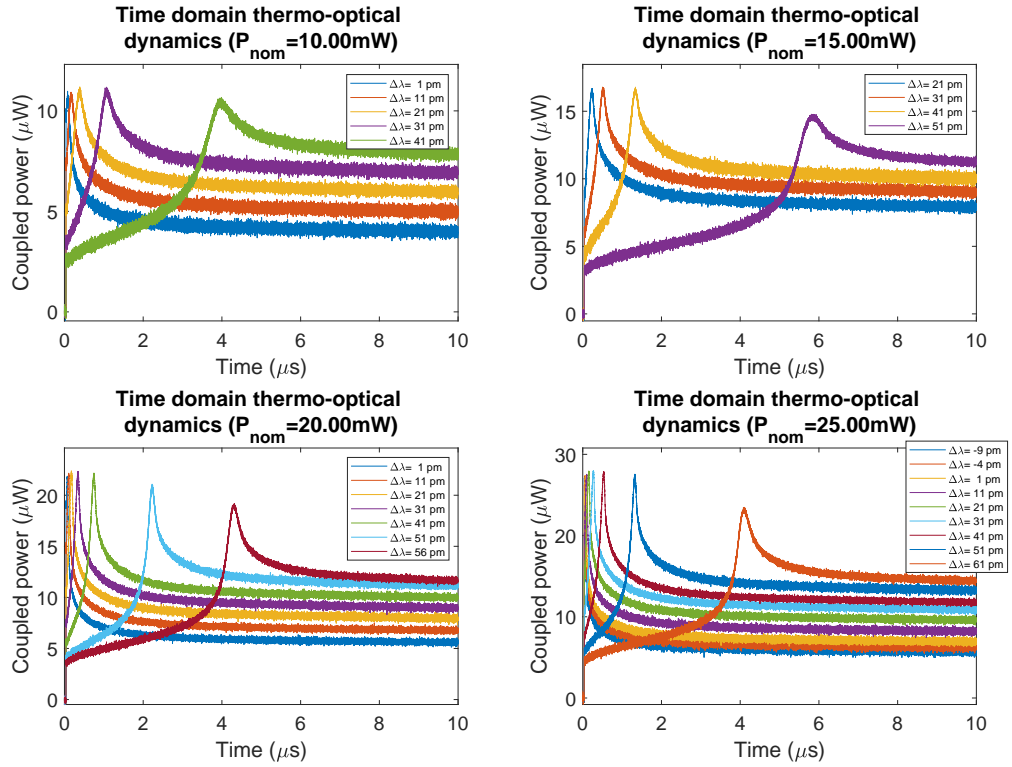


Figure 5.20: Time-resolved measurement of thermo-optic response under intense driving field. Each panel corresponds to a different nominal laser power (P_{nom}). The legend inset shows the initial laser-cavity (red) detuning, which is associated to a slower or faster TO response. The coupled power on the vertical axis is estimated from the peak signal from each set of experimental traces. The driving field is switched on at $t = 0$.

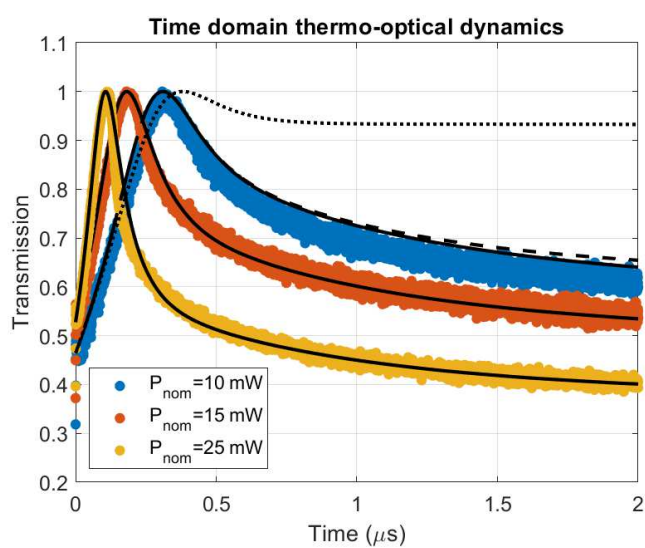


Figure 5.21: Time-resolved TO response of the resonator for different nominal pump power and fixed initial laser-cavity detuning ($\Delta \approx -\Gamma/2$). The response is normalized on the peak signal for each trace and the driving field is switched on at $t = 0$. Points represent experimental data. Solid black lines are the theoretical prediction according to a 3 thermal rates model. Dotted and dashed lines represent the theoretical prediction for a model with 1 and 2 thermal rates respectively.

material in the region where the mode is localized in the DA cavity [48]. As a thermal conductivity, we chose $K_1 = 1.25 \times 10^{-5}$ W/K, which is consistent with literature results [79] for similar PhC cavities. The detuning Δ is calculated from the initial transmission at the beginning of time-evolution and the pumping field intensity s_{in} is adjusted in accordance with the experimental conditions. The numerical integration matches the experimental result within the first 300 ns of time evolution, and it is consistent with the thermal decay rate retrieved from experimental results, being $\gamma_{th,1}/2\pi = K_1/(2\pi C_{p,1}) \approx 1$ MHz, but it eventually fails to describe the dynamics of the system on a longer timescale.

As aforementioned, in order to correctly describe the evolution of the system while keeping a discrete approximation of the heat diffusion equation, we expanded our model by introducing more than one thermal volume. In this framework, eqs. (5.5) become:

$$\frac{da(t)}{dt} = \left(i\Delta - \frac{\Gamma(U)}{2} \right) a(t) - i\omega_0\alpha\Delta T(t)a(t) + \sqrt{\eta\Gamma(U)}s_{in}(t) \quad (5.22a)$$

$$C_{p,1} \frac{d(\Delta T_1)}{dt} = \bar{\Gamma}_{abs}(U)|a(t)|^2 - K_1\Delta T_1(t) \quad (5.22b)$$

$$C_{p,2} \frac{d(\Delta T_2)}{dt} = K_1\Delta T_1(t) - K_2\Delta T_2(t) \quad (5.22c)$$

...

$$C_{p,n} \frac{d(\Delta T_n)}{dt} = K_{n-1}\Delta T_{n-1}(t) - K_n\Delta T_n(t) \quad (5.22d)$$

where $\Delta T = \sum_{i=1}^n \Delta T_i$. The former two equations describe the absorption of optical energy within the confined mode region, while the remaining $n - 1$ equations model the diffusion towards the rest of the physical system [47]. Although the model can be in principle refined arbitrarily, we notice that truncation at $n = 2$ already provides an accurate description of the temporal dynamics, as shown in fig. 5.21 (dashed line), where we choose $K_2 \approx K_1$ and $V_{th,2} = 6V_{th,1}$. This approximation yields a thermal decay rate $\gamma_{th,2}/2\pi = K_2/(2\pi C_{p,2}) \approx 100$ kHz, which is again in agreement with

5.5. Conclusions

the spectral measurements. In order to correct for the asymptotic decay of the measurement, we included in the final model (solid black lines), a third thermal rate (truncation $n = 3$) $\gamma_{th,3} \approx 15\gamma_{th,2}$. This is not associated to any appreciable spectral feature at this resolution, but the phenomenology of the effect suggests the possibility to exploit it as an additional source of group delay.

Remarkably, the model we formalized correctly predicts the temporal dynamics for any value of input power and detuning, upon appropriate choice of the physical parameters involved. Further investigation, involving a more quantitative matching between theory and experiments in multiple configurations are currently undergoing. Accordingly to the preliminary results presented here, we believe that a more accurate model for the spectral investigation of the phenomenon could be generalized from eqs. (5.22).

5.5 Conclusions

In this chapter, we described an effect of induced transparency observed in PhC resonators as a consequence of a Kerr-type thermo-optical interaction. The phenomenon bears similarities with induced transparency phenomenology in different physical systems (atomic, opto-mechanical and vibrational), but it is associated with a non-resonant first-order thermal response. Due to the intrinsically slow nature of thermal phenomena compared to the optical timescale, the effect is extremely narrow-band, with a bandwidth of the order of $\gamma_{th}/2\pi \sim 1$ MHz, and it is observed by probing the spectral region where the cavity is resonantly driven by a strong control field. In order to physically model the effect, we developed a theoretical framework based on coupled equations of motion involving temperature and cavity field as dynamical variables. We showed experimentally that the model predicts qualitatively the spectroscopic and time-resolved measurements, while a more quantitative agreement can be found by refining the formulation in order to accurately describe the spatial and temporal thermal dynamics. Besides the novelty of the results presented here, we point out that the appropriate study of the effect may lead to technological applications which benefit from the

high group delay achievable with this technique. While in this discussion we presented a maximum value of $\tau_d = 4 \mu s$, we believe this could be significantly extended, also by implementing the technique to other types of thermo-optically coupled resonators, and possibly in a cascaded fashion.

Conclusions

In this thesis, we studied several aspects of the nonlinear optical response of planar photonic crystal cavities. Although the scientific literature provides a solid theoretical background and an established technological knowledge concerning the experimental fabrication and characterization of this specific kind of optical microresonators, their employment in practical devices is still very limited, despite several unique advantages due to the extreme field enhancement effect achievable in this type of devices. Aim of this work was to explore several properties of photonic crystal microresonators which specifically benefit from the high Q/V figure of merit, in the perspective of applications to photonic devices.

In chapter 3, we presented an integrated cavity design aimed to support a “comb-like” resonance spectrum, similar to the one of the archetypal Fabry-Pérot optical cavity, which does rely on a PhC-type confinement principle instead of whispering gallery modes. We achieved this result by exploiting the effective potential created by superposition of two mismatched dielectric lattices, which produces a comb of high- Q resonances equally spaced in energy and characterized by Hermite-Gauss mode envelope. We showed from theoretical arguments how the device layout allows to tune the modes’ relative dispersion in order to achieve a set of three resonances equally spaced within the linewidth, thus able to support triply resonant nonlinear processes such as stimulated and spontaneous four-wave mixing. We implemented and refined state-of-art nanofabrication techniques for PhC cavities such as elec-

tron beam lithography and reactive ion etching to fabricate samples with extremely high Q factor ($Q > 10^6$) and unprecedented values of finesse ($\mathcal{F} = 8 \times 10^3$), in order to demonstrate experimentally the feasibility of the designed devices. From the experimental point of view, we developed a tuning technique to compensate *a posteriori* for the unavoidable error introduced by fabrication in terms of spectral detuning, and we showed how this can be used to achieve the required condition for triply resonant frequency conversion. Although the experimental study of the four-wave mixing implementation was still under development, we provided a numerical estimate of the expected generation efficiency, with promising results in comparison to other types of state-of-art microresonators. Specifically, the PBG-type confinement mechanism for in-plane localization allows to surpass the performance, both in terms of finesse and nonlinear coupling, of any silicon microresonator. From an application standpoint, the devices still need further development for efficient implementation to photonic integrated circuits. The most critical points, in terms of design are 1) the integration to a buried (encapsulated) geometry and 2) the on-chip coupling with waveguides. The latter point, in particular, would allow to fully exploit the potential of nonlinear coupling between all the three modes while keeping high the coupling efficiency.

In chapter 4, we investigated on the optical properties of a specific type of silicon rich silicon nitride for the applications to photonics in PhC based resonators. We showed how the material, based on an amorphous PECVD deposition, exhibits high optical quality at telecom wavelength in a CMOS-compatible platform, such that it enables the fabrication of PhC cavities with quality factor as high as $Q = 120,000$ in a suspended membrane with low refractive index contrast. Moreover, we performed a systematic study of the nonlinear properties of SRSN by second- and third-harmonic generation experiments, quantifying generation efficiencies of $\rho_{SH} = 4.7 \times 10^{-7} \text{ W}^{-1}$ and $\rho_{TH} = 5.9 \times 10^{-5} \text{ W}^{-2}$ respectively for the two processes and, remarkably, we observed absence of two-photon absorption quenching for coupled power up to few milliwatts. Despite the generation efficiencies are lower compared to other materials used in photonics, such as silicon, the absence of TPA consti-

tutes an intrinsic advantage compared to these platforms, paving the way to high-power technological applications. The material is particularly suited for the implementation to photonic devices, thanks to the low temperatures required for its growth, which make the fabrication process CMOS-compatible. In this perspective, a key point for further investigation would be to reduce the residual linear absorption at telecom wavelength, which remains the main limitation to the fabrication of ultrahigh-Q microresonators and to nonlinear operation in general.

In the last chapter of the work, we presented a novel phenomenon observed experimentally in PhC cavities, consisting in a narrow-bandwidth induced transparency effect. We developed a theoretical model which explains our observations as a consequence of thermo-optic effect, resulting in an effective Kerr-type interaction, namely a power dependent shift of the resonance wavelength. The model predicts qualitatively and partially quantitatively our experimental observations, which are based on a systematic study of the optical response of a PhC microresonator in a pump and probe scheme performed with sub-MHz resolution at optical wavelength. Our results are corroborated by a comprehensive analysis of the thermo-optical properties of the PhC cavity, consisting in linear and nonlinear characterization of the resonance spectrum at the thermal equilibrium and in the temporally resolved measurement of the dynamical response of the resonator. Our results provide the first description of a temperature-mediated induced transparency phenomenon in integrated resonators, which bears similarities with analogous induced transparency phenomena associated with slow-light, while it shows unique and completely novel phenomenology and features, such as a group delay as high as several microseconds, a typical linewidth of the order of 100 kHz and the absence of a physical resonance supporting the effect. An associated peak group delay the order of 1 μ s was observed without incurring in nonlinear (bistable) regime, a value comparable to the best results from other slow-light systems [129, 127]. In the perspective of integration, the phenomenon would enable to achieve extremely high group delay performances in a fully technology-compatible fashion, especially in view of cascaded resonator arrangements. Further studies in different cavity geometries (e.g.

whispering gallery mode resonators) are currently under development.

All the topics discussed here bring about further development perspectives, several of which are currently object of investigation by this and other research groups.

List of abbreviations

AAH Aubry-André-Harper. 68–70, 72, 80

AOM Acousto-Optic Modulator. 132, 134, 135

BOX Buried OXide. 44, 52, 75, 128

BZ Brillouin Zone. 6–8, 11, 12, 16–18, 57

CCD Charge-Coupled Device. 56, 105, 106, 108

CMOS Complementary Metal–Oxide–Semiconductor. 19, 75, 89, 90, 93, 102, 110, 150

CPO Coherent Population Oscillation. 115

CW Continuous Wave. 36, 54, 97, 104, 105

DFG Difference Frequency Generation. 26, 28

DL Device Layer. 44, 46, 50, 52, 75

DOS Density Of States. 22, 24

EBL Electron Beam Lithography. vi, 46–49, 81, 97, 128

ECL External Cavity Laser. 55, 132, 133, 135, 142

EIT Electromagnetically Induced Transparency. 114–116, 123, 124

- FBS** Fiber Beam-Splitter. 133
- FCA** Free Carrier Absorption. 30, 33–37, 90, 100, 117, 121
- FCD** Free Carrier Dispersion. 29, 31, 34–37, 90, 121, 130
- FDTD** Finite Difference Time Domain. 69–74, 78, 87, 95, 96, 103
- FP** Fabry Pérot. 55, 64, 77, 78
- FSR** Free Spectral Range. xii, 65, 74, 75, 77–82, 84
- FWHM** Full Width at Half Maximum. 19, 124, 139, 141
- FWM** Four-Wave Mixing. 25–27, 64–66, 74, 84, 85, 87, 88, 93
- GME** Guided Mode Expansion. xiii, 94, 95
- ICP** Inductively Coupled Plasma. xii, 50, 52, 53, 97
- LI** Lock-in (Amplifier). 125, 132–135
- MZI** Mach–Zehnder Interferometer. 132, 134, 142
- NA** Numerical Aperture. 54
- OMIT** Opto-Mechanically Induced Transparency. 115, 116, 123, 142
- OPO** Optical Parametric Oscillator. 63, 64, 87, 88
- PBG** Photonic BandGap. iv–vi, 7–9, 12–14, 16–19, 22, 23, 69, 73, 74, 94, 95
- PECVD** Plasma-Enhanced Chemical Vapor Deposition. xii, 90, 92, 93, 97, 150
- PhC** Photonic Crystal. iv–vii, xi–xiii, 6–23, 32, 35, 37–40, 43, 44, 46–48, 50, 53–60, 65, 66, 68–70, 73, 75, 83–85, 87, 88, 90, 93, 96, 97, 99–103, 107, 108, 110, 114, 120, 129, 131, 138, 146, 147, 149–151

List of abbreviations

- PMMA** Poly-Methyl-MetaAcrylate. xii, 47, 48
- QD** Quantum Dot. 23
- RIE** Reactive Ion Etching. vi, xii, 46, 50, 52, 53, 97
- RS** Resonant Scattering. xii, xiii, 41, 54–58, 60, 73–75, 77–80, 97–99, 101, 104–106, 108, 109, 125–131, 133–135, 138, 142, 143
- SBS** Stimulated Brillouin Scattering. 115
- SEM** Scanning Electron Microscope. xii, xiii, 15, 48, 49, 51, 53, 54, 65, 72, 81, 96, 97, 103, 104, 129
- SFG** Sum Frequency Generation. 26
- SHG** Second Harmonic Generation. 26, 102, 110
- SOI** Silicon-On-Insulator. vi, 32, 43–45, 50, 60, 75, 79, 89, 120, 128
- SPDC** Spontaneous Parametric Down-Conversion. 28
- SPM** Self Phase Modulation. 25–28
- SRSN** Silicon-Rich Silicon Nitride. xiii, 90, 93, 94, 97, 100–104, 107, 110, 150
- TE** Transverse Electric. 10–14, 16, 17, 54, 73, 75
- TEC** Thermo-Electric Cooler. 129
- THG** Third Harmonic Generation. 25–27, 102, 110
- TIR** Total Internal Reflection. vi, 9, 11, 12, 19, 22, 23, 65
- TM** Transverse Magnetic. 10–14, 17
- TO** Thermo-Optic. xiv, 29, 31, 35–37, 41, 90, 98, 100, 101, 115, 116, 118, 119, 121, 129, 130, 137, 138, 140, 142–145

TOIT Thermo-Optically Induced Transparency. xiii, xiv, 118, 120, 123, 127, 130, 132, 138, 139, 141, 142

TPA Two-Photon Absorption. xiii, 25–36, 40, 65, 90, 93, 94, 100, 110, 111, 117, 121

WGM Whispering Gallery Mode. 64–66, 78

XPM Cross Phase Modulation. 25, 27, 28

List of publications

Articles in peer reviewed international journals

- **M. Clementi**, A. Barone, T. Fromherz, D. Gerace, and M. Galli, “Selective tuning of optical modes in a silicon comb-like photonic crystal cavity”.
Nanophotonics (*in press*)
- T. Domínguez Bucio, C. Lacava, **M. Clementi**, J. Faneca, I. Skandalos, A. Baldycheva, M. Galli, K. Debnath, P. Petropoulos, and F. Y. Gardes, “Silicon Nitride Photonics for the Near-Infrared”.
IEEE Journal of Selected Topics in Quantum Electronics 26, 1–13 (2019)
- **M. Clementi**, K. Debnath, M. Sotto, A. Barone, A. Z. Khokhar, T. Domínguez Bucio, S. Saito, F. Y. Gardes, D. Bajoni, and M. Galli, “Cavity-enhanced harmonic generation in silicon rich nitride photonic crystal microresonators”.
Applied Physics Letters, 114 (13), 131103 (2019)
- K. Debnath, **M. Clementi**, T. Domínguez Bucio, A. Z. Khokhar, M. Sotto, K. M. Grabska, D. Bajoni, M. Galli, S. Saito, and F. Y. Gardes, “Ultrahigh-Q photonic crystal cavities in silicon rich nitride”.
Optics Express 25 (22), 27334 (2017)
- **M. Clementi**, A. Pappa, A. Eckstein, I. A. Walmsley, E. Kashefi, and

S. Barz, “Classical multiparty computation using quantum resources”.
Physical Review A, 96 (6), 062317 (2017)

Conferences

- **M. Clementi***, A. Barone T. Fromherz, D. Gerace, and M. Galli,
“Demonstration of Optical Frequency Combs in Photonic Crystal Cavities”.
Invited talk at 21th International Conference on Transparent Optical Networks (ICTON), Angers, France (07/2019)
- T. Domínguez Bucio*, S. L. Scholl, S. Ilie, C. Lacava, K. Debnath, A. Z. Khokhar, M. Banakar, M. Sotto, K. M. Grabska, **M. Clementi**, D. Bajoni, M. Galli, S. Saito, P. Petropoulos, and F. Y. Gardes,
“Low-Temperature NH₃-Free Silicon Nitride Platforms for Integrated Photonics”.
Given talk at IEEE 15th International Conference on Group IV Photonics (GFP) (08/2018)
- **M. Clementi***, K. Debnath, M. Sotto, T. Domínguez Bucio, M. Lisicidini, D. Bajoni, F. Gardes, and M. Galli,
“Harmonic Generation in Silicon Rich Nitride Photonic Crystal Cavities”.
Given talk at PLASMONICA 2018, Florence, Italy (07/2018),
- **M. Clementi***, K. Debnath, M. Sotto, T. Domínguez Bucio, M. Lisicidini, D. Bajoni, F. Gardes, and M. Galli,
“Harmonic Generation in Silicon Rich Nitride Photonic Crystal Cavities”.
Given talk at CLEO: Science and Innovations, San Jose, USA (05/2018),

Bibliography

- [1] J. D. Joannopoulos, S. G. Johnson, J. N. Winn, and R. D. Meade, *Photonic Crystals: Molding the Flow of Light*. Princeton University Press, 2008.
- [2] E. Yablonovitch, “Inhibited Spontaneous Emission in Solid-State Physics and Electronics,” *Physical Review Letters*, vol. 58, pp. 2059–2062, may 1987.
- [3] S. John, “Strong localization of photons in certain disordered dielectric superlattices,” *Physical Review Letters*, vol. 58, pp. 2486–2489, jun 1987.
- [4] L. Rayleigh, “Xxvi. on the remarkable phenomenon of crystalline reflexion described by prof. stokes,” *The London, Edinburgh, and Dublin Philosophical Magazine and Journal of Science*, vol. 26, no. 160, pp. 256–265, 1888.
- [5] H. Kosaka and T. Kawashima, “Superprism phenomena in photonic crystals,” *Physical Review B - Condensed Matter and Materials Physics*, vol. 58, no. 16, pp. R10096–R10099, 1998.
- [6] T. F. Krauss, R. M. D. L. Rue, S. Brand, R. M. De La Rue, and S. Brand, “Two-dimensional photonic-bandgap structures operating at near-infrared wavelengths,” *Nature*, vol. 383, pp. 699–702, oct 1996.

- [7] Y. Akahane, T. Asano, B.-S. Song, and S. Noda, “High-Q photonic nanocavity in a two-dimensional photonic crystal,” *Nature*, vol. 425, pp. 944–947, oct 2003.
- [8] P. B. Deotare, M. W. McCutcheon, I. W. Frank, M. Khan, and M. Lončar, “High quality factor photonic crystal nanobeam cavities,” *Applied Physics Letters*, vol. 94, no. 12, 2009.
- [9] K. Hennessy, A. Badolato, M. Winger, D. Gerace, M. Atatüre, S. Gulde, S. Fält, E. L. Hu, and A. Imamoglu, “Quantum nature of a strongly coupled single quantum dot–cavity system,” *Nature*, vol. 445, pp. 896–899, feb 2007.
- [10] J. D. Jackson, *Classical electrodynamics*. Wiley, 1999.
- [11] K. Sakoda, *Optical Properties of Photonic Crystals*. Springer Series in Optical Sciences, Springer Berlin Heidelberg, 2004.
- [12] E. Hecht, *Optics*. Pearson education, Addison-Wesley, 2002.
- [13] A. Yariv and P. Yeh, *Photonics*. Oxford University Press, Inc., 2006.
- [14] L. Andreani and M. Agio, “Photonic bands and gap maps in a photonic crystal slab,” *IEEE Journal of Quantum Electronics*, vol. 38, pp. 891–898, jul 2002.
- [15] S. G. Johnson, S. Fan, P. R. Villeneuve, J. D. Joannopoulos, and L. A. Kolodziejski, “Guided modes in photonic crystal slabs,” *Physical Review B*, vol. 60, no. 8, pp. 5751–5758, 1999.
- [16] M. Notomi, “Manipulating light with strongly modulated photonic crystals,” *Reports on Progress in Physics*, vol. 73, p. 096501, sep 2010.
- [17] Y. A. Vlasov, M. O’Boyle, H. F. Hamann, and S. J. McNab, “Active control of slow light on a chip with photonic crystal waveguides,” *Nature*, vol. 438, pp. 65–69, nov 2005.

BIBLIOGRAPHY

- [18] L. C. Andreani and D. Gerace, “Photonic-crystal slabs with a triangular lattice of triangular holes investigated using a guided-mode expansion method,” *Physical Review B - Condensed Matter and Materials Physics*, vol. 73, no. 23, pp. 1–16, 2006.
- [19] H.-Y. Ryu, M. Notomi, and Y.-H. Lee, “High-quality-factor and small-mode-volume hexapole modes in photonic-crystal-slab nanocavities,” *Applied Physics Letters*, vol. 83, pp. 4294–4296, nov 2003.
- [20] P. T. Kristensen, C. Van Vlack, and S. Hughes, “Effective mode volumes for leaky optical cavities,” *AIP Conference Proceedings*, vol. 1398, no. 10, pp. 100–102, 2011.
- [21] H. Choi, M. Heuck, and D. Englund, “Self-Similar Nanocavity Design with Ultrasmall Mode Volume for Single-Photon Nonlinearities,” *Physical Review Letters*, vol. 118, p. 223605, may 2017.
- [22] M. Minkov, V. Savona, and D. Gerace, “Photonic crystal slab cavity simultaneously optimized for ultra-high Q / V and vertical radiation coupling,” *Applied Physics Letters*, vol. 111, p. 131104, sep 2017.
- [23] S. Hu, M. Khater, R. Salas-Montiel, E. Kratschmer, S. Engelmann, W. M. J. Green, and S. M. Weiss, “Experimental realization of deep-subwavelength confinement in dielectric optical resonators,” *Science Advances*, vol. 4, p. eaat2355, aug 2018.
- [24] E. M. Purcell, H. C. Torrey, and R. V. Pound, “Resonance Absorption by Nuclear Magnetic Moments in a Solid,” *Physical Review*, vol. 69, pp. 37–38, jan 1946.
- [25] J. Bravo-Abad, A. Rodriguez, P. Bermel, S. G. Johnson, J. D. Joannopoulos, and M. Soljacic, “Enhanced nonlinear optics in photonic-crystal microcavities,” *Optics Express*, vol. 15, no. 24, p. 16161, 2007.
- [26] M. Soljačić, M. Ibanescu, S. G. Johnson, Y. Fink, and J. D. Joannopoulos, “Optimal bistable switching in nonlinear photonic crystals,” *Physi-*

cal Review E - Statistical Physics, Plasmas, Fluids, and Related Interdisciplinary Topics, vol. 66, no. 5, p. 4, 2002.

- [27] L. Novotny and B. Hecht, *Principles of Nano-Optics*. Cambridge University Press, 2006.
- [28] K. Nozaki, T. Tanabe, A. Shinya, S. Matsuo, T. Sato, H. Taniyama, and M. Notomi, “Sub-femtojoule all-optical switching using a photonic-crystal nanocavity,” *Nature Photonics*, vol. 4, pp. 477–483, jul 2010.
- [29] M. Fox, *Quantum optics: an introduction*. Oxford Master Series in Atomic, Optical and Laser Physics, Oxford: Oxford Univ. Press, 2006.
- [30] S. Noda, M. Fujita, and T. Asano, “Spontaneous-emission control by photonic crystals and nanocavities,” *Nature Photonics*, vol. 1, no. 8, pp. 449–458, 2007.
- [31] A. Auffèves, D. Gerace, M. Richard, S. Portolan, M. França Santos, L. C. Kwek, and C. Miniatura, *Strong Light-Matter Coupling*. WORLD SCIENTIFIC, feb 2014.
- [32] J. Leuthold, C. Koos, and W. Freude, “Nonlinear silicon photonics,” *Nature Photonics*, vol. 4, pp. 535–544, aug 2010.
- [33] R. Boyd and D. Prato, *Nonlinear Optics*. Elsevier Science, 2008.
- [34] R. Loudon, *The Quantum Theory of Light*. Oxford: Clarendon Press, 1973.
- [35] R. M. Osgood, N. C. Panoiu, J. I. Dadap, X. Liu, X. Chen, I. W. Hsieh, E. Dulkeith, W. M. Green, and Y. A. Vlasov, “Engineering nonlinearities in nanoscale optical systems: Physics and applications in dispersion-engineered silicon nanophotonic wires,” *Optics InfoBase Conference Papers*, vol. 1, no. 1, pp. 162–235, 2009.
- [36] M. Dinu, F. Quochi, and H. Garcia, “Third-order nonlinearities in silicon at telecom wavelengths,” *Applied Physics Letters*, vol. 82, pp. 2954–2956, may 2003.

BIBLIOGRAPHY

- [37] D. C. Hutchings, M. Sheik-Bahae, D. J. Hagan, and E. W. Van Stryland, “Kramers-Krönig relations in nonlinear optics,” *Optical and Quantum Electronics*, vol. 24, pp. 1–30, jan 1992.
- [38] P. E. Barclay, K. Srinivasan, and O. Painter, “Nonlinear response of silicon photonic crystal micresonators excited via an integrated waveguide and fiber taper,” *Optics Express*, vol. 13, no. 3, p. 801, 2005.
- [39] T. Uesugi, B.-S. Song, T. Asano, and S. Noda, “Investigation of optical nonlinearities in an ultra-high-Q Si nanocavity in a two-dimensional photonic crystal slab,” *Optics Express*, vol. 14, no. 1, p. 377, 2006.
- [40] M. Borselli, T. J. Johnson, and O. Painter, “Measuring the role of surface chemistry in silicon microphotronics,” *Applied Physics Letters*, vol. 88, p. 131114, mar 2006.
- [41] H. Sekoguchi, Y. Takahashi, T. Asano, and S. Noda, “Photonic crystal nanocavity with a Q-factor of ~ 9 million,” *Optics Express*, vol. 22, p. 916, jan 2014.
- [42] T. Asano, Y. Ochi, Y. Takahashi, K. Kishimoto, and S. Noda, “Photonic crystal nanocavity with a Q factor exceeding eleven million,” *Optics Express*, vol. 25, no. 3, p. 1769, 2017.
- [43] J. Komma, C. Schwarz, G. Hofmann, D. Heinert, and R. Nawrodt, “Thermo-optic coefficient of silicon at 1550 nm and cryogenic temperatures,” *Applied Physics Letters*, vol. 101, p. 041905, jul 2012.
- [44] T. Tanabe, M. Notomi, S. Mitsugi, A. Shinya, and E. Kuramochi, “Fast bistable all-optical switch and memory on a silicon photonic crystal on-chip,” *Optics Letters*, vol. 30, p. 2575, oct 2005.
- [45] M. Belotti, J. F. Galisteo López, S. De Angelis, M. Galli, I. Maksymov, L. C. Andreani, D. Peyrade, and Y. Chen, “All-optical switching in 2D silicon photonic crystals with low loss waveguides and optical cavities,” *Optics express*, vol. 16, no. 15, pp. 11624–11636, 2008.

- [46] M. Notomi, A. Shinya, S. Mitsugi, G. Kira, E. Kuramochi, and T. Tanabe, “Optical bistable switching action of Si high-Q photonic-crystal nanocavities,” *Optics Express*, vol. 13, no. 7, p. 2678, 2005.
- [47] T. Carmon, L. Yang, and K. J. Vahala, “Dynamical thermal behavior and thermal self-stability of microcavities,” *Optics Express*, vol. 12, p. 4742, oct 2004.
- [48] K. Welna, S. L. Portalupi, M. Galli, L. O’Faolain, and T. F. Krauss, “Novel Dispersion-Adapted Photonic Crystal Cavity With Improved Disorder Stability,” *IEEE Journal of Quantum Electronics*, vol. 48, pp. 1177–1183, sep 2012.
- [49] A. Sarangan, *Nanofabrication: Principles to Laboratory Practice*. CRC Press, 2016.
- [50] M. Razeghi, *Fundamentals of solid state engineering, 3rd edition*. Springer, Boston, MA, 01 2009.
- [51] M. Schatzl, *Deterministic Coupling of SiGe Quantum Dots to Photonic Crystal Structures*. PhD thesis, Johannes Kepler Universität Linz, 2016.
- [52] M. Bruel, “Process for the production of thin semiconductor material films,” 1994.
- [53] A. Shakoor, R. Lo Savio, S. L. Portalupi, D. Gerace, L. C. Andreani, M. Galli, T. F. Krauss, and L. Ofaolain, “Enhancement of room temperature sub-bandgap light emission from silicon photonic crystal nanocavity by Purcell effect,” *Physica B: Condensed Matter*, vol. 407, no. 20, pp. 4027–4031, 2012.
- [54] M. W. McCutcheon, G. W. Rieger, I. W. Cheung, J. F. Young, D. Dalacu, S. Frédérick, P. J. Poole, G. C. Aers, and R. L. Williams, “Resonant scattering and second-harmonic spectroscopy of planar photonic crystal microcavities,” *Applied Physics Letters*, vol. 87, p. 221110, nov 2005.

BIBLIOGRAPHY

- [55] M. Galli, S. L. Portalupi, M. Belotti, L. C. Andreani, L. O’Faolain, and T. F. Krauss, “Light scattering and Fano resonances in high-Q photonic crystal nanocavities,” *Applied Physics Letters*, vol. 94, no. 7, pp. 1–3, 2009.
- [56] U. Fano, “Effects of configuration interaction on intensities and phase shifts,” *Physical Review*, vol. 124, no. 6, pp. 1866–1878, 1961.
- [57] D. Thomson, A. Zilkie, J. E. Bowers, T. Komljenovic, G. T. Reed, L. Vivien, D. Marris-Morini, E. Cassan, L. Viroth, J.-M. Fédéli, J.-M. Hartmann, J. H. Schmid, D.-X. Xu, F. Boeuf, P. O’Brien, G. Z. Mashanovich, and M. Nedeljkovic, “Roadmap on silicon photonics,” *Journal of Optics*, vol. 18, p. 073003, jul 2016.
- [58] N.-V.-Q. Tran, S. Combrié, and A. De Rossi, “Directive emission from high-Q photonic crystal cavities through band folding,” *Physical Review B*, vol. 79, p. 041101, jan 2009.
- [59] S. L. Portalupi, M. Galli, C. Reardon, T. Krauss, L. O’Faolain, L. C. Andreani, and D. Gerace, “Planar photonic crystal cavities with far-field optimization for high coupling efficiency and quality factor,” *Optics Express*, vol. 18, p. 16064, jul 2010.
- [60] M. Galli, D. Gerace, K. Welna, T. F. Krauss, L. O’Faolain, G. Guizzetti, L. C. Andreani, L. O. Faolain, G. Guizzetti, and L. C. Andreani, “Low-power continuous-wave generation of visible harmonics in silicon photonic crystal nanocavities,” *Optics Express*, vol. 18, p. 26613, dec 2010.
- [61] M. S. Mohamed, A. Simbula, J.-F. Carlin, M. Minkov, D. Gerace, V. Savona, N. Grandjean, M. Galli, and R. Houdré, “Efficient continuous-wave nonlinear frequency conversion in high-Q gallium nitride photonic crystal cavities on silicon,” *APL Photonics*, vol. 2, p. 031301, mar 2017.
- [62] T. Udem, R. Holzwarth, and T. W. Hänsch, “Optical frequency metrology,” *Nature*, vol. 416, pp. 233–237, mar 2002.

- [63] T. J. Kippenberg, R. Holzwarth, and S. A. Diddams, “Microresonator-Based Optical Frequency Combs,” *Science*, vol. 332, pp. 555–559, apr 2011.
- [64] N. C. Harris, D. Grassani, A. Simbula, M. Pant, M. Galli, T. Baehr-Jones, M. Hochberg, D. Englund, D. Bajoni, and C. Galland, “Integrated Source of Spectrally Filtered Correlated Photons for Large-Scale Quantum Photonic Systems,” *Physical Review X*, vol. 4, p. 041047, dec 2014.
- [65] D. Grassani, A. Simbula, S. Pirotta, M. Galli, M. Menotti, N. C. Harris, T. Baehr-Jones, M. Hochberg, C. Galland, M. Liscidini, and D. Bajoni, “Energy correlations of photon pairs generated by a silicon microring resonator probed by Stimulated Four Wave Mixing,” *Scientific Reports*, vol. 6, p. 23564, apr 2016.
- [66] C. Reimer, L. Caspani, M. Clerici, M. Ferrera, M. Kues, M. Peccianti, A. Pasquazi, L. Razzari, B. E. Little, S. T. Chu, D. J. Moss, and R. Morandotti, “Integrated frequency comb source of heralded single photons,” *Optics Express*, vol. 22, no. 6, pp. 6535–6546, 2014.
- [67] C. Reimer, M. Kues, P. Roztocky, B. Wetzal, F. Grazioso, B. E. Little, S. T. Chu, T. Johnston, Y. Bromberg, L. Caspani, D. J. Moss, and R. Morandotti, “Generation of multiphoton entangled quantum states by means of integrated frequency combs,” *Science*, vol. 351, pp. 1176–1180, mar 2016.
- [68] D. J. Moss, R. Morandotti, A. L. Gaeta, and M. Lipson, “New CMOS-compatible platforms based on silicon nitride and Hydex for nonlinear optics,” *Nature Photonics*, vol. 7, pp. 597–607, aug 2013.
- [69] F. Alpeggiani, L. C. Andreani, and D. Gerace, “Effective bichromatic potential for ultra-high Q-factor photonic crystal slab cavities,” *Applied Physics Letters*, vol. 107, p. 261110, dec 2015.
- [70] A. Simbula, M. Schatzl, L. Zagaglia, F. Alpeggiani, L. C. Andreani, F. Schäffler, T. Fromherz, M. Galli, D. Gerace, F. Sch, T. Fromherz,

BIBLIOGRAPHY

- M. Galli, and D. Gerace, “Realization of high-Q/V photonic crystal cavities defined by an effective Aubry-André-Harper bichromatic potential,” *APL Photonics*, vol. 2, p. 056102, may 2017.
- [71] S. Combrié, G. Lehoucq, G. Moille, A. Martin, and A. De Rossi, “Comb of high-Q Resonances in a Compact Photonic Cavity,” *Laser & Photonics Reviews*, vol. 11, p. 1700099, nov 2017.
- [72] P. G. Harper, “Single Band Motion of Conduction Electrons in a Uniform Magnetic Field,” *Proceedings of the Physical Society. Section A*, vol. 68, pp. 874–878, oct 1955.
- [73] S. Aubry and G. André, “Analyticity breaking and Anderson localization in incommensurate lattices,” in *Ann. Israel Phys. Soc*, vol. 3, p. 18, 1980.
- [74] M. Modugno, “Exponential localization in one-dimensional quasi-periodic optical lattices,” *New Journal of Physics*, vol. 11, p. 033023, mar 2009.
- [75] X. Ji, F. A. S. Barbosa, S. P. Roberts, A. Dutt, J. Cardenas, Y. Okawachi, A. Bryant, A. L. Gaeta, and M. Lipson, “Ultra-low-loss on-chip resonators with sub-milliwatt parametric oscillation threshold,” *Optica*, vol. 4, p. 619, jun 2017.
- [76] C. J. Chen, J. Zheng, T. Gu, J. F. McMillan, M. Yu, G.-Q. Lo, D.-L. Kwong, and C. W. Wong, “Selective tuning of high-Q silicon photonic crystal nanocavities via laser-assisted local oxidation,” *Optics Express*, vol. 19, p. 12480, jun 2011.
- [77] K. Hennessy, C. Högerle, E. Hu, A. Badolato, and A. Imamoglu, “Tuning photonic nanocavities by atomic force microscope nano-oxidation,” *Applied Physics Letters*, vol. 89, p. 041118, jul 2006.
- [78] S. Sokolov, J. Lian, E. Yüce, S. Combrié, G. Lehoucq, A. De Rossi, and A. P. Mosk, “Local thermal resonance control of GaInP photonic

- crystal membrane cavities using ambient gas cooling,” *Applied Physics Letters*, vol. 106, p. 171113, apr 2015.
- [79] L.-D. Haret, T. Tanabe, E. Kuramochi, and M. Notomi, “Extremely low power optical bistability in silicon demonstrated using 1D photonic crystal nanocavity,” *Optics Express*, vol. 17, p. 21108, nov 2009.
- [80] B. E. Deal and A. S. Grove, “General Relationship for the Thermal Oxidation of Silicon,” *Journal of Applied Physics*, vol. 36, pp. 3770–3778, dec 1965.
- [81] F. Intonti, N. Caselli, S. Vignolini, F. Riboli, S. Kumar, A. Rastelli, O. G. Schmidt, M. Francardi, A. Gerardino, L. Balet, L. H. Li, A. Fiore, and M. Gurioli, “Mode tuning of photonic crystal nanocavities by photoinduced non-thermal oxidation,” *Applied Physics Letters*, vol. 100, p. 033116, jan 2012.
- [82] X. Zeng and M. A. Popović, “Design of triply-resonant microphotonic parametric oscillators based on Kerr nonlinearity,” *Optics Express*, vol. 22, p. 15837, jun 2014.
- [83] A. Rodriguez, M. Soljacic, J. D. Joannopoulos, and S. G. Johnson, “Chi2 and Chi3 harmonic generation at a critical power in inhomogeneous doubly resonant cavities,” *Optics Express*, vol. 15, no. 12, p. 7303, 2007.
- [84] M. Aspelmeyer, T. J. Kippenberg, and F. Marquardt, “Cavity optomechanics,” *Reviews of Modern Physics*, vol. 86, pp. 1391–1452, dec 2014.
- [85] S. Azzini, D. Grassani, M. Galli, L. C. Andreani, M. Sorel, M. J. Strain, L. G. Helt, J. E. Sipe, M. Liscidini, and D. Bajoni, “From classical four-wave mixing to parametric fluorescence in silicon microring resonators,” *Optics Letters*, vol. 37, no. 18, p. 3807, 2012.
- [86] S. Azzini, D. Grassani, M. Galli, D. Gerace, M. Patrini, M. Liscidini, P. Velha, and D. Bajoni, “Stimulated and spontaneous four-wave mix-

BIBLIOGRAPHY

- ing in silicon-on-insulator coupled photonic wire nano-cavities,” *Applied Physics Letters*, vol. 103, no. 3, 2013.
- [87] S. K. Selvaraja, E. Sleenckx, M. Schaekers, W. Bogaerts, D. V. Thourhout, P. Dumon, and R. Baets, “Low-loss amorphous silicon-on-insulator technology for photonic integrated circuitry,” *Optics Communications*, vol. 282, no. 9, pp. 1767–1770, 2009.
- [88] G.-L. Bona, R. Germann, and B. J. Offrein, “SiON high-refractive-index waveguide and planar lightwave circuits,” *IBM Journal of Research and Development*, vol. 47, pp. 239–249, mar 2003.
- [89] S. C. Mao, S. H. Tao, Y. L. Xu, X. W. Sun, M. B. Yu, G. Q. Lo, and D. L. Kwong, “Low propagation loss SiN optical waveguide prepared by optimal low-hydrogen module,” *Optics Express*, vol. 16, p. 20809, dec 2008.
- [90] D. J. Blumenthal, R. Heideman, D. Geuzebroek, A. Leinse, and C. Roeloffzen, “Silicon Nitride in Silicon Photonics,” *Proceedings of the IEEE*, vol. 106, pp. 2209–2231, dec 2018.
- [91] A. Arbabi and L. L. Goddard, “Measurements of the refractive indices and thermo-optic coefficients of Si₃N₄ and SiO_x using microring resonances,” *Optics Letters*, vol. 38, p. 3878, oct 2013.
- [92] T. D. Bucio, C. Lacava, M. Clementi, J. Faneca, I. Skandalos, A. Baldycheva, M. Galli, K. Debnath, P. Petropoulos, and F. Gardes, “Silicon Nitride Photonics for the Near-Infrared,” *IEEE Journal of Selected Topics in Quantum Electronics*, vol. 26, pp. 1–13, mar 2020.
- [93] K. Debnath, M. Clementi, T. T. D. Bucio, A. A. Z. Khokhar, M. Sotto, K. K. M. Grabska, D. Bajoni, M. Galli, S. Saito, and F. Y. F. Gardes, “Ultrahigh-Q photonic crystal cavities in silicon rich nitride,” *Optics Express*, vol. 25, p. 27334, oct 2017.
- [94] M. Clementi, K. Debnath, M. Sotto, A. Barone, A. Z. Khokhar, T. D. Bucio, S. Saito, F. Y. Gardes, D. Bajoni, and M. Galli, “Cavity-

- enhanced harmonic generation in silicon rich nitride photonic crystal microresonators,” *Applied Physics Letters*, vol. 114, p. 131103, apr 2019.
- [95] F. L. Riley, “Silicon Nitride and Related Materials,” *Journal of the American Ceramic Society*, vol. 83, pp. 245–265, dec 2000.
- [96] T. Domínguez Bucio, A. Z. Khokhar, C. Lacava, S. Stankovic, G. Z. Mashanovich, P. Petropoulos, and F. Y. Gardes, “Material and optical properties of low-temperature NH₃-free PECVD SiN_x layers for photonic applications,” *Journal of Physics D: Applied Physics*, vol. 50, p. 025106, jan 2017.
- [97] C. Lacava, S. Stankovic, A. Z. Khokhar, T. D. Bucio, F. Y. Gardes, G. T. Reed, D. J. Richardson, and P. Petropoulos, “Si-rich Silicon Nitride for Nonlinear Signal Processing Applications,” *Scientific Reports*, vol. 7, p. 22, dec 2017.
- [98] E. Kuramochi, M. Notomi, S. Mitsugi, A. Shinya, T. Tanabe, and T. Watanabe, “Ultrahigh-Q photonic crystal nanocavities realized by the local width modulation of a line defect,” *Applied Physics Letters*, vol. 88, p. 041112, jan 2006.
- [99] K. Debnath, T. D. Bucio, A. Al-Attili, A. Z. Khokhar, S. Saito, and F. Y. Gardes, “Photonic crystal waveguides on silicon rich nitride platform,” *Optics Express*, vol. 25, p. 3214, feb 2017.
- [100] M. W. McCutcheon, J. F. Young, G. W. Rieger, D. Dalacu, S. Frédérick, P. J. Poole, and R. L. Williams, “Experimental demonstration of second-order processes in photonic crystal microcavities at submilliwatt excitation powers,” *Physical Review B*, vol. 76, p. 245104, dec 2007.
- [101] S. Buckley, M. Radulaski, K. Biermann, and J. Vučković, “Second harmonic generation in photonic crystal cavities in (111)-oriented GaAs,” *Applied Physics Letters*, vol. 103, p. 211117, nov 2013.

BIBLIOGRAPHY

- [102] K. Rivoire, Z. Lin, F. Hatami, W. T. Masselink, and J. Vučković, “Second harmonic generation in gallium phosphide photonic crystal nanocavities with ultralow continuous wave pump power,” *Optics Express*, vol. 17, no. 25, p. 22609, 2009.
- [103] S. Yamada, B.-S. Song, S. Jeon, J. Upham, Y. Tanaka, T. Asano, and S. Noda, “Second-harmonic generation in a silicon-carbide-based photonic crystal nanocavity,” *Optics Letters*, vol. 39, p. 1768, apr 2014.
- [104] Y. Zeng, I. Roland, X. Checoury, Z. Han, M. El Kurdi, S. Sauvage, B. Gayral, C. Brimont, T. Guillet, M. Mexis, F. Semond, and P. Boucaud, “Resonant second harmonic generation in a gallium nitride two-dimensional photonic crystal on silicon,” *Applied Physics Letters*, vol. 106, p. 081105, feb 2015.
- [105] J. S. Levy, M. A. Foster, A. L. Gaeta, and M. Lipson, “Harmonic generation in silicon nitride ring resonators,” *Optics Express*, vol. 19, no. 12, p. 11415, 2011.
- [106] S. Yamada, B.-S. Song, S. Jeon, J. Upham, Y. Tanaka, T. Asano, and S. Noda, “Second-harmonic generation in a silicon-carbide-based photonic crystal nanocavity,” *Optics Letters*, vol. 39, p. 1768, apr 2014.
- [107] R. W. Boyd and D. J. Gauthier, ““Slow” and “fast” light,” in *Progress in Optics*, vol. 43, pp. 497–530, Elsevier Masson SAS, 2002.
- [108] M. D. Stenner, D. J. Gauthier, and M. A. Neifeld, “The speed of information in a ‘fast-light’ optical medium,” *Nature*, vol. 425, pp. 695–698, oct 2003.
- [109] T. F. Krauss, “Why do we need slow light?,” *Nature Photonics*, vol. 2, no. 8, pp. 448–450, 2008.
- [110] T. Baba, “Slow light in photonic crystals,” *Nature Photonics*, vol. 2, pp. 465–473, aug 2008.

- [111] R. Tucker, Pei-Cheng Ku, and C. Chang-Hasnain, “Slow-light optical buffers: capabilities and fundamental limitations,” *Journal of Light-wave Technology*, vol. 23, pp. 4046–4066, dec 2005.
- [112] J. Li, T. P. White, L. O’Faolain, A. Gomez-Iglesias, and T. F. Krauss, “Systematic design of flat band slow light in photonic crystal waveguides,” *Optics Express*, vol. 16, p. 6227, apr 2008.
- [113] L. V. Hau, S. E. Harris, Z. Dutton, and C. H. Behroozi, “Light speed reduction to 17 meters per second in ultracold atomic gases,” *Letters to Nature*, vol. 397, no. February, pp. 594–598, 1999.
- [114] B. Corcoran, C. Monat, C. Grillet, D. J. Moss, B. J. Eggleton, T. P. White, L. O’Faolain, and T. F. Krauss, “Green light emission in silicon through slow-light enhanced third-harmonic generation in photonic-crystal waveguides,” *Nature Photonics*, vol. 3, no. 4, pp. 206–210, 2009.
- [115] C. Monat, B. Corcoran, D. Pudo, M. Ebnali-Heidari, C. Grillet, M. Pelusi, D. Moss, B. Eggleton, T. White, L. O’Faolain, and T. Krauss, “Slow Light Enhanced Nonlinear Optics in Silicon Photonic Crystal Waveguides,” *IEEE Journal of Selected Topics in Quantum Electronics*, vol. 16, no. 1, pp. 344–356, 2010.
- [116] M. Passoni, D. Gerace, L. O’Faolain, and L. C. Andreani, “Slow light with interleaved p-n junction to enhance performance of integrated Mach-Zehnder silicon modulators,” *Nanophotonics*, may 2019.
- [117] M. Fleischhauer and M. D. Lukin, “Quantum memory for photons: Dark-state polaritons,” *Physical Review A*, vol. 65, p. 022314, jan 2002.
- [118] B. Julsgaard, J. Sherson, J. I. Cirac, J. Flurášek, and E. S. Polzik, “Experimental demonstration of quantum memory for light,” *Nature*, vol. 432, no. 7016, pp. 482–486, 2004.
- [119] C. Liu, Z. Dutton, C. H. Behroozi, and L. V. Hau, “Observation of coherent optical information storage in an atomic medium using halted light pulses,” *Nature*, vol. 409, pp. 490–493, jan 2001.

BIBLIOGRAPHY

- [120] J. J. Longdell, E. Fraval, M. J. Sellars, and N. B. Manson, “Stopped Light with Storage Times Greater than One Second Using Electromagnetically Induced Transparency in a Solid,” *Physical Review Letters*, vol. 95, p. 063601, aug 2005.
- [121] R. W. Boyd, “Material slow light and structural slow light: similarities and differences for nonlinear optics [Invited]: reply,” *Journal of the Optical Society of America B*, vol. 29, no. 9, p. 2644, 2012.
- [122] M.-c. N. Dicaire, J. Upham, I. De Leon, S. A. Schulz, and R. W. Boyd, “Group delay measurement of fiber Bragg grating resonances in transmission: Fourier transform interferometry versus Hilbert transform,” *Journal of the Optical Society of America B*, vol. 31, p. 1006, may 2014.
- [123] K. Boller, A. Imamolu, S. E. Harris, A. Imamoglu, and S. E. Harris, “Observation of electromagnetically induced transparency,” *Physical Review Letters*, vol. 66, pp. 2593–2596, may 1991.
- [124] M. Fleischhauer, A. Imamoglu, and J. P. Marangos, “Electromagnetically induced transparency: Optics in coherent media,” *Reviews of Modern Physics*, vol. 77, pp. 633–673, jul 2005.
- [125] M. S. Bigelow, N. N. Lepeshkin, and R. W. Boyd, “Observation of Ultraslow Light Propagation in a Ruby Crystal at Room Temperature,” *Physical Review Letters*, vol. 90, no. 11, p. 4, 2003.
- [126] M. S. Bigelow, “Superluminal and Slow Light Propagation in a Room-Temperature Solid,” *Science*, vol. 301, pp. 200–202, jul 2003.
- [127] C. H. Dong, Z. Shen, C. L. Zou, Y. L. Zhang, W. Fu, and G. C. Guo, “Brillouin-scattering-induced transparency and non-reciprocal light storage,” *Nature Communications*, vol. 6, pp. 1–6, 2015.
- [128] S. Weis, R. Rivière, S. Deléglise, E. Gavartin, O. Arcizet, A. Schliesser, and T. J. Kippenberg, “Optomechanically Induced Transparency,” *Science*, vol. 330, pp. 1520–1523, dec 2010.

- [129] A. H. Safavi-Naeini, T. P. M. Alegre, J. Chan, M. Eichenfield, M. Winger, Q. Lin, J. T. Hill, D. E. Chang, and O. Painter, “Electromagnetically induced transparency and slow light with optomechanics,” *Nature*, vol. 472, pp. 69–73, apr 2011.
- [130] M. L. Gorodetsky and I. S. Grudinin, “Fundamental thermal fluctuations in microspheres,” *Journal of the Optical Society of America B*, vol. 21, p. 697, apr 2004.
- [131] J. K. Yu, S. Mitrovic, D. Tham, J. Varghese, and J. R. Heath, “Reduction of thermal conductivity in phononic nanomesh structures,” *Nature Nanotechnology*, 2010.
- [132] A. Jain, Y. J. Yu, and A. J. McGaughey, “Phonon transport in periodic silicon nanoporous films with feature sizes greater than 100 nm,” *Physical Review B - Condensed Matter and Materials Physics*, vol. 87, no. 19, pp. 1–8, 2013.
- [133] N. Zen, T. A. Puurtinen, T. J. Isotalo, S. Chaudhuri, and I. J. Maasilta, “Engineering thermal conductance using a two-dimensional phononic crystal,” *Nature communications*, vol. 5, p. 3435, 2014.
- [134] T. Tanabe, M. Notomi, and E. Kuramochi, “Measurement of ultra-high-Q photonic crystal nanocavity using single-sideband frequency modulator,” *Electronics Letters*, vol. 43, no. 3, p. 187, 2007.
- [135] E. A. Donley, T. P. Heavner, F. Levi, M. O. Tataw, and S. R. Jefferts, “Double-pass acousto-optic modulator system,” *Review of Scientific Instruments*, vol. 76, p. 063112, jun 2005.